

ARTICLE

Evaluating sequential and allosteric activation models in I_{Ks} channels with mutated voltage sensors

David Fedida¹, Daniel Sastre¹, Ying Dou¹, Maartje Westhoff¹, and Jodene Eldstrom¹

The ion-conducting I_{Ks} channel complex, important in cardiac repolarization and arrhythmias, comprises tetramers of KCNQ1 α -subunits along with 1–4 KCNE1 accessory subunits and calmodulin regulatory molecules. The E160R mutation in individual KCNQ1 subunits was used to prevent activation of voltage sensors and allow direct determination of transition rate data from complexes opening with a fixed number of 1, 2, or 4 activatable voltage sensors. Markov models were used to test the suitability of sequential versus allosteric models of I_{Ks} activation by comparing simulations with experimental steady-state and transient activation kinetics, voltage-sensor fluorescence from channels with two or four activatable domains, and limiting slope currents at negative potentials. Sequential Hodgkin–Huxley-type models approximately describe I_{Ks} currents but cannot explain an activation delay in channels with only one activatable subunit or the hyperpolarizing shift in the conductance–voltage relationship with more activatable voltage sensors. Incorporating two voltage sensor activation steps in sequential models and a concerted step in opening via rates derived from fluorescence measurements improves models but does not resolve fundamental differences with experimental data. Limiting slope current data that show the opening of channels at negative potentials and very low open probability are better simulated using allosteric models of activation with one transition per voltage sensor, which implies that movement of all four sensors is not required for I_{Ks} conductance. Tiered allosteric models with two activating transitions per voltage sensor can fully account for I_{Ks} current and fluorescence activation kinetics in constructs with different numbers of activatable voltage sensors.

Introduction

The modeling of the processes underlying the activation and subsequent opening of voltage-dependent K⁺ (Kv) channels has always been central to the description of, and differentiation between, potential mechanisms underlying membrane excitation. The original formalism of squid axon conductance and gating by Hodgkin and Huxley contains only a few dynamic elements, which mirrors the simplicity of purpose in a physiological system designed primarily to conduct nerve impulses at high speed and frequency (Hodgkin and Huxley, 1952). Despite this, some fundamental properties of the original Hodgkin and Huxley model remain key features of almost all voltage-dependent channel models, including the delay observed in channel opening requiring multiple activation steps and independent movement of gating particles or voltage sensor (VS) domains, while separation between VS activation and pore domain (PD) dynamics is not considered in the squid axon model.

Activation models of Kv channels have undergone several important reinventions since these foundational studies, increasing in complexity and flexibility as subsequent investigators

sought to describe ion channel systems in much greater quantitative detail (Zagotta et al., 1994; Sigworth, 1994) and understand those that did not conform, or only partially conformed, to adapted Hodgkin–Huxley models. Those studies more interested in reproducing action potential waveforms and properties have tended to rely on more classical ion channel model formulations (Hafner et al., 1981; O’Hara et al., 2011; Paci et al., 2013), but the expression of individual ion channels, such as Shaker, in heterologous systems that permit precise time- and voltage-control of the experimental substrate has allowed much more detailed analysis of channel kinetics in the absence of other overlapping ion channel conductances (Zagotta et al., 1994). The aims of these models have been to either refine the earlier models to achieve a previously unattainable quantitatively accurate description of the particular ion channel system under investigation (Schoppa and Sigworth, 1998a, 1998b; Zheng et al., 2001; Rothberg and Magleby, 2000) or to build new models to account for large qualitative differences in activation mechanisms (Horrigan et al., 1999; Altomare et al., 2001; Chowdhury and Chanda, 2012a,

¹Department of Anesthesiology, Pharmacology and Therapeutics, University of British Columbia, Vancouver, Canada.

Correspondence to David Fedida: david.fedida@ubc.ca

M. Westhoff’s current affiliation is Department of Physiology and Membrane Biology, School of Medicine, University of California Davis, Davis, CA, USA.

© 2024 Fedida et al. This article is distributed under the terms of an Attribution–Noncommercial–Share Alike–No Mirror Sites license for the first six months after the publication date (see <http://www.upress.org/terms/>). After six months it is available under a Creative Commons License (Attribution–Noncommercial–Share Alike 4.0 International license, as described at <https://creativecommons.org/licenses/by-nc-sa/4.0/>).

2012b). The original Hodgkin-Huxley formulation for *Loligo* expects ion conduction when all VSs become activated, but fly and mammalian ion channel schemes allow for a subsequent final or multiple concerted transition(s) (Schoppa and Sigworth, 1998b; Ledwell and Aldrich, 1999) from VS activated-closed states to VS activated-open states. These transitions are included after the VS activation delay to reproduce channel opening that is slower than predicted from a strict Hodgkin-Huxley model, and such concerted events make the overall activation scheme sequential (Zagotta et al., 1994; Sigworth, 1994; Horrigan et al., 1999).

The success of structural modeling approaches to understanding ion channel activation gating and block mechanisms (Ramasubramanian and Rudy, 2018; Maly et al., 2022; Willegems et al., 2022; Chan et al., 2023), along with the use of molecular dynamics simulations to directly predict the underlying molecular motions and atomistic details of permeation, gating, and block (Carnevale et al., 2021; Flood et al., 2019; Abrahamyan et al., 2023), have, in recent years, lessened the popularity of classic kinetic modeling. Still, there remains value in examining how the demonstrated biophysical properties of currents through ion channels conform to the particular stringencies of different types of Markovian kinetic models. Kinetic models with rate constants provide a precise means to describe and/or predict behavior (kinetics) of ion channels by collating the information that must be accounted for by any viable structural models. Also, the structural basis for all of the observed kinetic states summarized by the model needs to be determined to understand gating. Indeed, such models are still widely used to study mutational effects on the kinetics of ion channels (Moreno et al., 2013; Carbonell-Pascual et al., 2016), predict action potential properties and shapes in novel iPSC models (Paci et al., 2013; Kernik et al., 2019), for stratification of genetic variants (Kernik et al., 2020), and the potential pro-arrhythmic response to drugs in development (Bottino et al., 2006; Moreno et al., 2016; Passini et al., 2017; Li et al., 2019).

The history of activation models for KCNQ1 and I_{Ks}

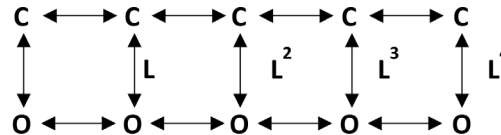
Models of KCNQ1 and I_{Ks} , KCNE1:KCNQ1 in a stoichiometry up to 4:4 (Murray et al., 2016), are of particular interest to investigators, and a particular challenge to model as the kinetic interconversion between the two current phenotypes is so extreme upon the coexpression of KCNE1. Activation of KCNQ1 shows time constants in the order of 16–20 ms at +10 to +50 mV (Ruscic et al., 2013), while being closer to 3 s for I_{Ks} at +60 mV (Westhoff et al., 2019), and is followed by inactivation, which is apparently absent in I_{Ks} (Hou et al., 2017). The activation delay observed in both channels suggests that the VSs of KCNQ1 and I_{Ks} , much like those of *Shaker*, must also undergo multiple transitions during activation, prior to PD opening. At the present time, two classes of Markov-type models are proposed to account for the activation properties of KCNQ1 and/or I_{Ks} . Early models from Pusch et al. and Silva and Rudy are sequential (see below), and incorporate VSs which transition independently through one or two conformational changes prior to becoming fully activated (Pusch et al., 1998, 2001; Silva and Rudy, 2005).

The fully activated VS-channel complex then undergoes a single concerted step to allow the PD to open to one or more open states (Pusch et al., 1998; Silva and Rudy, 2005; Nekouzadeh et al., 2008). Slow activation in I_{Ks} versus KCNQ1 is reproduced by slowing the VS transitions from resting to intermediate states.

Sequential schemes



Allosteric schemes



A related model for single-channel recordings was modified to allow channels to open to subconducting levels when individual VS domains were fully activated, and an additional fast closing pathway was connected to channel open states to account for the rapid closing of channels during opening bursts seen during long sweep records of single-channel openings (Werry et al., 2013).

Allosteric models of gating (see above) in the manner described for the voltage gating behavior of *Shaker* channels (McCormack et al., 1994), HCN channels (Altomare et al., 2001), and large conductance Ca^{2+} -activated potassium (BK) channels (Horrigan et al., 1999; Rothberg and Magleby, 2000; Horrigan and Aldrich, 2002; Horrigan, 2012) have also been suggested to best represent KCNQ1 (Ma et al., 2011; Meisel et al., 2012; Osteen et al., 2012) and I_{Ks} gating (Meisel et al., 2012). In these models, independent activation of VSs increases the channel open probability and this positive allosteric activation is represented by a factor L (Osteen et al., 2012), which increases the equilibrium constants for the C-O transitions L-fold for each VS that is activated (Horrigan et al., 1999). The concordance on the voltage axis of voltage sensor fluorescence (VCF) measurements with the voltage dependence of the conductance-voltage (G-V) relationship in KCNQ1 (Osteen et al., 2010), but not I_{Ks} , led these authors to propose an allosteric gating model for KCNQ1 alone but to incorporate a concerted opening step in channel gating into their I_{Ks} models, with the implication that the VSs in all four subunits must be activated before some local conformational rearrangement can lead to PD opening. Subsequently, the idea of a concerted opening step has proven controversial, with some studies in support (Barro-Soria et al., 2014) and others favoring an allosteric model of activation for I_{Ks} as well as KCNQ1 (Meisel et al., 2012; Zaydman et al., 2014). Recent experiments that demonstrate the opening of I_{Ks} channels with only a single, two, or three active VS domains have lent further experimental support to the allosteric activation of the VSs and pore conductance (Westhoff et al., 2019), but this idea remains controversial. Structural modeling has identified specific domains of KCNE subunits that may regulate gating via an allosteric network of residues on the S5-S6 domain (Kuenze et al., 2020), and molecular simulations support flexible coupling between VS and

pore, thus permitting pore opening at intermediate VS positions (Ramasubramanian and Rudy, 2018).

Study aims

In this study, we will compare the predictions of different activation models for I_{Ks} with our recent and new experimental data to determine which class of models best reproduces I_{Ks} activation kinetics. Our goal in modeling is to use the simplest applicable models with the fewest transitions that are currently understood to make sense in the context of our current appreciation of I_{Ks} channel activation. We will explore the effect of reducing the number of independently moving VSs (e.g., wild-type [wt] versus E160R-containing VS subunits), as we have already shown how this affects the electrophysiological properties of I_{Ks} (Westhoff et al., 2019). We started with the most basic of Hodgkin-Huxley type models and increased model complexity and type, from sequential to allosteric, ending with a 30-state activation gating model, all the time trying to define transition rates using experimental electrophysiological and VCF data. Our analysis suggests that allosteric gating models provide the best fit to a broad set of experimentally defined biophysical parameters. Channel opening results from the movement of independent VSs, so that in I_{Ks} channels a final concerted transition of all four VSs is not obligatory for PD opening. The allosteric factor is relatively small at 1.36, which suggests that activation of less than four VSs may result in meaningful current conduction through open substates of the I_{Ks} channel at intermediate voltages.

Materials and methods

Chemicals

Alexa Fluor 488 C₅-maleimide was obtained from Thermo Fisher Scientific. HMR1556 was from Bio-Techne Canada. All other chemicals were obtained from Sigma-Aldrich. All biohazard and animal care activities were carried out after ethical review and approval by The University of British Columbia Biosafety and Animal Care and Use Committees under protocol numbers B21-0006 and A22-0049-R001, respectively, and their antecedents.

Molecular biology

The EQ (KCNE1:KCNQ1), EQQ (KCNE1:KCNQ1:KCNQ1) and EQQQQ (KCNE1:KCNQ1:KCNQ1:KCNQ1) constructs were generated as described (Murray et al., 2016). The E160R mutation was incorporated into Q1 subunits of the fusion constructs via a gBlocks Gene Fragment (Integrated DNA Technologies) with compatible restriction sites. Throughout this paper, the E160R mutation in Q1 is denoted by an asterisk (Q*). The EQ*QQ*Q* and tandem fluorescence constructs were made by Applied Biological Materials Inc. from precursor constructs that we provided to them. All mutations were confirmed by sequencing. Constructs for transfection into mammalian cells were subcloned into pcDNA3.1 (RRID:Addgene_117272).

Cell culture and transfection

tsA201-transformed human embryonic kidney 293 cells (whole cell) or mouse *ltk*- fibroblast cells (cell attached) were obtained

from ATCC or Sigma-Aldrich, certified authentic, validated, and mycoplasma free. Cell lines were cultured and plated as described (Murray et al., 2016; Westhoff et al., 2017). Transfections with Lipofectamine 2000 (Thermo Fisher Scientific) followed the manufacturer's protocol, and cotransfection with KCNE1-GFP (hereafter referred to as E1) was at a 3:1 ratio of E1:KCNQ1 (E1+Q1). For experiments described in Figs. 1 and 2, to measure the I_{Ks} activation kinetics, we usually used the concatenated construct EQ, instead of co-transfected E1+Q1, to ensure a 4:4 stoichiometry of expressed E1:Q1 channels. However, we have previously shown that a 3:1 transfection ratio of E1:Q1 construct DNA produces the same activation and deactivation kinetics whether EQ, Q1+E1, QQQQ+E1, QQ+E1, or EQQQQ+E1 are transfected into tsA201 cells (Westhoff et al., 2019). In the extended τ_{act} -V relationship in Fig. 3 B, we did include time constant data from two wt QQ+E1 cells at +110 and three wt QQQQ+E1 cells at +110 to +130 mV. All experiments were performed 24–48 h after transfection at room temperature, 22°C. Successfully transfected cells were identified by GFP-fluorescence. For recordings in the presence of E1, currents <500 pA or not expressing I_{Ks} were discarded.

Oocyte preparation

Mature female *Xenopus laevis* frogs (*Xenopus* 1) between 3 and 4 yr of age and between 0.2 and 0.5 kg in weight were anesthetized in a solution containing 2 g/l tricaine methanesulfonate and 2 g/l HEPES (pH 7.4 with NaOH). Animals were euthanized in accordance with the University of British Columbia animal care protocol number A22-0049-R001. The ovarian lobes were extracted, divided into smaller sections, and digested for 2–4 h in a solution containing 3 mg/ml collagenase type 4 (Worthington Biochemical Corporation), 82.5 mM NaCl, 2.5 mM KCl, 1 mM MgCl₂, and 5 mM HEPES (pH 7.6 with NaOH). The oocytes were washed and stored in media containing 500 ml Leibovitz's L-15 medium (Thermo Fisher Scientific), 15 mM HEPES, 1 mM glutamine, and 500 µM gentamicin, brought up to 1 liter with distilled water (pH 7.6 with NaOH). Stage IV and V oocytes were selected and stored at 18°C.

Oocytes were injected with cRNA synthesized using the Ambion mMessage mMachine T7 transcription kit (Applied Biosystems). Q1 constructs differed from mammalian constructs as they were modified to remove extracellular C214 and C331 cysteine residues and included a G219C for fluorescence purposes. 10 ng of C214A/G219C/C331A Q1 pcDNA3.1+ (psQ; a gift from Dr. Jianmin Cui, Washington University in St. Louis, St. Louis, MO) cRNA was injected, while 50 ng of the tandem constructs in pGEMHE was used. These were psQQ (C214A/G219C/C331A Q1-C214A/C331A Q1) and psQ-E160R Q* (C214A/G219C/C331A Q1-E160R/C214A/C331A Q1*), also named psQQ*. The E160R mutation prevents activation of VSs in two of the four domains. The pGEMHE (RRID:Addgene_114674) vector was a gift from Dr. Yoshihiro Kubo (National Institute for Physiological Sciences, Okazaki, Japan). All constructs were coinjected with 5 ng E1 in pBSTA. Experiments were performed 3–4 days after injection at room temperature. For wt hERG, cRNA was synthesized as above and oocytes were injected with 10–100 ng cRNA. Injected oocytes were stored in ND96 (96 mM NaCl, 3 mM KCl, 2 mM

CaCl_2 , 1 mM MgCl_2 , and 5 mM HEPES at pH 7.4) and incubated at 18°C prior to use.

Electrophysiology solutions

For whole-cell recordings, the bath solution contained (in mM) 135 NaCl, 5 KCl, 1 MgCl_2 , 2.8 NaAcetate, and 10 HEPES (pH 7.4 with NaOH). The pipette solution contained (in mM) 130 KCl, 5 EGTA, 1 MgCl_2 , 4 $\text{Na}_2\text{-ATP}$, 0.1 GTP, and 10 HEPES (pH 7.2 with KOH). For two-electrode fluorometry (VCF), the bath solution contained ND96 plus 0.1 mM LaCl_3 . The pipette solution contained 3 M KCl. For cell-attached recordings (Fig. S1), the bath solution contained (in mM) 135 KCl, 1 MgCl_2 , 0.1 CaCl_2 , 10 HEPES, and 10 dextrose (pH 7.4 with KOH). The pipette solution contained (in mM) 6 NaCl, 129 MES, 1 MgCl_2 , 5 KCl, 1 CaCl_2 , and 10 HEPES (pH 7.4 with NaOH; Eldstrom et al., 2021).

Electrophysiology

Whole-cell, macropatch, and single-channel currents were acquired using an Axopatch 200B amplifier, Digidata 1440A, and pClamp 10 software (Molecular Devices). For whole-cell recordings, a linear multistage electrode puller (Sutter Instrument) was used to pull electrode pipettes from thin-walled borosilicate glass (World Precision Instruments; Murray et al., 2016; Westhoff et al., 2017). Pipettes were fire-polished prior to use. Electrode resistances for whole-cell recordings were between 1 and 3 $\text{M}\Omega$, with series resistances <5 $\text{M}\Omega$. Series resistance compensation of ~80% was applied to all whole-cell recordings, with a calculated voltage error of ~1 mV/nA current. Whole-cell currents were sampled at 10 kHz and filtered at 2–5 kHz (Murray et al., 2016; Westhoff et al., 2017). We had noticed in preliminary experiments that the endogenous delayed rectifier K^+ current in tsA201 cells contaminated the I_{Ks} current records at a level of ~200–400 pA at +80 mV, and this is an issue when measuring the delay time to exponential activation (Δt) for constructs expressed at a lower level, such as $\text{EQ}^*\text{QQ}^*\text{Q}^*$, as is typical for many concatemers. Thus, wherever possible and for all Δt measurements, whole-cell current data used in this study were obtained from experiments after 0.3–1.0 μM HMR1556 subtraction. Examples of tsA201 cells transfected with $\text{EQ}^*\text{Q}+\text{E1}$ and exposed to HMR1556 are shown in Fig. S1. The endogenous current is revealed by exposure to 0.3 μM HMR1556, which blocks I_{Ks} but leaves the endogenous current unaffected. Doses of 1 μM HMR1556 were required to affect endogenous currents. The only important contamination of the I_{Ks} current is the step current that occurs at the start of the pulse and the subsequent development of the I_{Ks} time course and tail currents are unaffected, as is the G-V relationship (Fig. S1 B). The contamination at the start of the depolarization is removed by subtraction of records obtained after, from those obtained before exposure to 0.3 μM HMR1556 (Fig. S1 E).

Voltage-clamp fluorimetry

Oocytes were labeled with 10 μM Alexa Fluor 488 C₅-maleimide in a depolarizing high potassium ion solution containing (in mM) 98 KCl, 1.8 CaCl_2 , and 5 HEPES (pH 7.6 with KOH) for 30 min on ice. The oocytes were washed with the bath solution and left on ice prior to recording. Fluorescence and ionic current

recordings were obtained simultaneously as described (Es-Salah-Lamoureux et al., 2010) with an Omega XF100-2 filter set (Omega Optical Inc). Two-electrode voltage-clamp experiments were performed using an Oocyte Clamp OC-725C (Warner Instruments) and digitized via a Digidata 1440A (Molecular Devices) running pClamp 10 software (Molecular Devices). Fluorescence recordings from the same oocyte were averaged when necessary to improve the signal-to-noise ratio and photobleaching of the dye between recordings was minimized by using an electronic shutter to limit oocyte UV exposure during the voltage step epochs of the protocol. To correct the fluorescence baseline for dye bleaching, a fluorescence signal was recorded at the -140 mV holding potential in the absence of a voltage step and was subtracted from signals recorded during steps to voltages between -180 and +80 mV. Bleaching did not appear to affect the components or kinetics of the fluorescence-voltage (F-V) relations, but diminished signal amplitude over time.

Data and statistical analysis

Data were cumulated and analyzed in MS Excel. G-V plots were obtained from tail current amplitudes. For electrophysiological experiments, the number of replicates is stated in the figure legends and Table 1. Although we often collected many replicates, we used a minimum sample size of three to allow calculation of sample means and standard errors (SEM) using standard functions in MS Excel. Data were discarded if cells were excessively leaky or degraded during experiments. No sample size calculation was performed as a standard procedure in cellular electrophysiology experiments. All results are reported as mean \pm SEM, as denoted by error bars on data points unless otherwise stated. For comparison of $t_{1/2}$ differences in Fig. S4 B, a statistical comparison was performed using a one-way ANOVA with a Bonferroni post hoc test. P values <0.05 were considered to be statistically significant.

A Boltzmann sigmoidal equation was used to fit G-Vs (MS Excel and Graphpad Prism) to obtain the $V_{1/2}$ and slope factor. F-V plots were fit with a double Boltzmann equation. Current activation records were fit with a single exponential equation in Clampfit 10.7 (RRID:SCR_011323; Molecular Devices), with the fit starting at ~0.5–1 s with the clear initiation of exponential current relaxation. Deactivating currents were fit with a single exponential in Prism 7 for all 4 s of the deactivating pulse to extract time constants. Δt and τ_{act} relationships were fit in MS Excel with a linear regression equation to obtain the Pearson correlation coefficient (R). To obtain α , β , δ , and γ rate constants, rate versus voltage plots are fit with the equation:

$$\text{rate constant}(V) = \text{rate constant}(0) \times e^{\frac{VF}{RT}}, \quad (1)$$

where V and 0 refer to voltage in V, z, the apparent valence, and F, R, and T have their usual meanings. At room temperature (22°C), $F/RT = 39.6 \text{ V}^{-1}$.

Modeling

MATLAB R2021, R2022, and R2023a (RRID:SCR_001622; Mathworks) were used to construct and simulate Markov models. Final models were also checked using IonChannelLab software

Table 1. Isochronal kinetics: Mean $V_{1/2}$ of activation (mV) and slope values (k , mV) for experimental data, and data from different models

Construct	G-V, $V_{1/2}$, k (mV)	F1-V, $V_{1/2}$, k (mV)	F2-V, $V_{1/2}$, k (mV)	n , G-V, F-V
KCNQ1	-33.9 ± 0.51, 7.6 ± 0.24	-	-	3
EQ	13.2 ± 3.9, 13.5 ± 1.2	-	-	8
EQ*Q+E1	22.3 ± 1.9, 16.8 ± 0.77	-	-	5
EQ*QQ*Q*+E1	32.8 ± 5.7, 19.4 ± 1.2	-	-	5
psQ+E1 G-V	4.19 ± 2.6, 17.4 ± 1.3	-96.9 ± 2.0, 26.2 ± 1.0	3.0 ± 5.1, 18.6 ± 2.4	14, 8
psQQ+E1 G-V	7.06 ± 2.5, 15.2 ± 1.5	-88.2 ± 5.1, 29.4 ± 2.8	3.2 ± 1.8, 15.0 ± 2.4	10, 3
psQQ*+E1 G-V	23.5 ± 1.3, 16.2 ± 0.70	-86.5 ± 4.2, 28.2 ± 2.4	21.0 ± 4.7, 18.0 ± 2.8	13, 8
Model	G-V, $V_{1/2}$, k (mV)	F1-V, $V_{1/2}$, k (mV)	F2-V, $V_{1/2}$, k (mV)	
1 A	62.5, 10.0	-	-	
1 B	50.2, 13.2	-	-	
1 C	33.5, 18.2	-	-	
2 A	4.76, 20.6	-99.6, 30	3.6, 20.4	
2 B	23.2, 19.0	-88.2, 30	26.0, 17.1	
4 A	4.51, 21.4	-95.5, 29.6	5.8, 18.9	
4 B	22.0, 22.9	-93.9, 30.2	22.4, 19.5	
4 C	31.0, 23.3	-	-	
5 A	7.5, 17.5	-102, 28.6	2.93, 21.3	
5 B	20.6, 19.3	-101.9, 28.7	16.4, 24.7	
5 C	33.8, 20.0	-	-	

First 4 data rows are from tsA201 cells; rows 5–7 are from oocytes; values in rows 9–19 are from simulations. For Scheme 1, A and B, G-V values are predictions using Eq. 2 (Fig. 1 D).

(Santiago-Castillo et al., 2010), and model outputs were plotted using custom-written MATLAB routines. Within MATLAB, the function “ode23s” was used to solve differential equations using a Jacobian matrix, and the function “fminsearchbnd” with boundaries (D’Errico, 2021) was used to optimize rate constants and model fits to steady-state G-V and F-V relationships, τ_{act} and Δt , and time-dependent current and fluorescence recordings. We followed the methods described by Moreno et al. to use a bounded Nelder Mead optimization algorithm (Nelder and Mead, 1965; Moreno et al., 2016), and we optimized transition rates by minimizing a scalar function that simultaneously incorporated the squared errors (SumSq) between model and experimental G-Vs, F-Vs, τ_{act} versus Δt (e.g., Figs. 6 B, 12, and 13), and/or the error between experimental current recordings and the model simulations at +60 mV (Figs. 2 C and 12 A). It has been suggested that more predictive models can be obtained from data based on short experimental voltage-clamp protocols rather than those derived from more traditional current-voltage or time-voltage curves (Clerx et al., 2019). Here, we used a combination of different inputs as part of the optimization process. Empirically, we found that the isochronal G-V and F-V relationships were the quickest to optimize together, and gave excellent fits using the optimization algorithm, while including time-dependent current or fluorescence data slowed the process considerably. Usually, simulations were run until the

variable SumSq was no longer decreasing, which usually took between 500 and thousands of optimization cycles (e.g., Fig. S7). This process was then repeated a number of times to detect and exclude local minima and attempt to improve the overall fit to all the different data sets, G-V, F-V, τ_{act} -V, Δt -V, and current recordings. In the Scheme 1 models, the current time course was used as an important optimization parameter, but in Schemes 2, 3, 4, and 5 models, the Δt versus τ_{act} relationship was extensively used as an experimental input to ensure time-dependent delay and time constant data were considered together with the isochronal G-V and F-V relationships during the optimization process. The experimentally derived Δt versus τ_{act} graph defines the kinetics of transitions through closed states as well as the kinetics of the opening transition(s) as long as the two processes are temporally distinct. The object was not to build entirely new conceptual models of I_{Ks} activation gating but to explore the effect of reducing the numbers of functional VSs on already-existing sequential or allosteric models, with the specific aim of observing which ones could best simulate the experimental data we obtained from I_{Ks} constructs with one to three E160R-containing VSs (Westhoff et al., 2019). In this sense, model transitions were preconstrained and the absolute values of the rates themselves were of secondary importance to how the models themselves dealt with the experimentally observed effects of zero compared with two or three E160R-containing VSs.

In Markov model schemes, subscripts R or A indicate the number of resting or activated subunits. Closed and open channel states are indicated as "C" and "O," respectively. Forward and backward rate constants in VS state changes are indicated as " α , β " and " κ , λ ", for the first VS and second VS transitions, respectively. The allosteric factor in the model **Schemes 4** and **5** is indicated as "D." Voltage-dependent transition rates related to VS-pore coupling in the opening step of **Schemes 2, 3, 4**, and **5** are denoted by " δ " and " γ " for opening and closing, respectively.

Online supplemental material

Fig. S1 details the HMR1556 subtraction methodology used for tsA201 cell data in the study; **Figs. S2** and **S4** show the rationale for the use of prepulse potentials in tsA201 cells and oocytes; **Figs. S3, S5, S6**, and **S7** show additional results and model outputs.

Results

Kinetics of I_{Ks} channels with a single activatable VS domain

In wt I_{Ks} channels, the VS domains respond to depolarizing changes in transmembrane potential as physical charge translation within the electric field in a manner that leads to inner gate opening and ion conduction through the pore (Wang et al., 2020). The conversion of the negatively charged glutamic acid at E160 in the S2 of Q1 into a positively charged arginine prevents individual VS translation as evidenced by the lack of methanethiosulfonate modification of the ion currents or visible changes in the Alexa Fluor 488 fluorescence signal from labeled G229C or G219C residues, respectively, in the E160R subunits (Westhoff et al., 2019). The inclusion of an E160R mutation in all four VS domains of the Q1 subunit results in a non-activatable channel, from which ion currents cannot be observed (Restier et al., 2008; Zayzman et al., 2014; Westhoff et al., 2019), but the experimental consequence of including E160R mutations in one, two, or three tethered-subunit VSs is still to allow channel complexes to activate and pass current (**Fig. 1 A**, Westhoff et al., 2019). It can be seen that while the expression of E1-GFP (referred to as E1) along with the Q1 subunits produces dramatic changes in the current activation and deactivation recordings from KCNQ1 alone to EQ with a 4:4 KCNE1:KCNQ1 stoichiometry, the inclusion of the E160R mutation, indicated by a *, in two (EQ*Q+E1) or three (EQ*QQ*Q*+E1) Q1 subunits does not, at first glance, alter the channel activation kinetics a great deal, although it does reduce the overall current magnitude from wt (Westhoff et al., 2019). Upon careful inspection, though, activation is slower in channels containing more E160R subunits at equivalent potentials, while EQ*Q+E1 and EQ*QQ*Q*+E1 channels deactivate more quickly than wt EQ at -40 mV.

The amplitudes of experimentally obtained tail currents were fit to a simple Boltzmann distribution to obtain the half-activation ($V_{1/2}$) values and plotted as a function of step potential (**Fig. 1 B**) as isochronal (10 s) G-V relationships (see **Table 1**). In prior experiments, we have shown that tethering I_{Ks} channel constructs of different stoichiometries (Q, EQ, EQQQ, EQQQQ, without or with additional E1 co-expression) does not affect the $V_{1/2}$ of activation (Murray et al., 2016; Westhoff et al., 2019), so

the depolarization of the EQ*Q+E1 and EQ*QQ*Q*+E1 G-V relationships compared with the wt EQ G-V cannot be explained by the concatenation of subunits, but is the effect of the presence of the E160R mutation in the VSs of these channels. The open probability distribution (Po-V) can be expressed as

$$Po = \{1/[1 + \exp(V_{1/2} - V)zF/RT]\}^a, \quad (2)$$

where a is estimated to be proportional to the number of closed states in a sequential model (Fitzhugh, 1965; Gagnon and Bezanilla, 2009), and is used here to approximate the number of activatable VS subunits. The $V_{1/2}$ and RT/zF (32.8 and 19.4 mV) obtained from the single activatable subunit construct (EQ*QQ*Q*+E1), with $a = 1$, generates the solid red curve through experimental data points (**Fig. 1 B**), and these $V_{1/2}$ and z values were then inserted into **Eq. 2** with $a = 2$ or $a = 4$ for the EQ*Q+E1 and wt EQ constructs, respectively, to obtain the green and blue dashed curves displaced to more positive voltages than the EQ*QQ*Q*+E1 data. In **Fig. 1 B**, the voltage dependencies of experimental data from the two or four active VS subunit constructs are hyperpolarized with respect to the single activatable subunit data and not depolarized as expected from **Eq. 2**, but the slope factors, k , for wt (13.5 mV) and EQ*Q+E1 (16.8 mV) experimental constructs are in close agreement with those for the wt and EQ*Q+E1 dashed curves generated from **Eq. 2** (14.6 and 16.2 mV, respectively). The similarity of the slopes between data and theory supports the idea of 1, 2, or 4 activatable VSs in the constructs as engineered, even though the $V_{1/2}$ shifts do not support the simple activation mechanism defined by **Eq. 2** and **Scheme 1**.

The aims of the present experiments are to understand in greater detail the activation process of the I_{Ks} channel complex and to assess the suitability of the various kinetic models proposed for their activation. What is new here is the approach of utilizing changes in I_{Ks} current kinetics and fluorescence in the presence of the E160R mutation in two or three Q1 VS domains, as a way to reduce the number of activatable subunits and simplify the number of possible model transitions that are required to simulate the data. As well, rate constants derived from the simplest model with the fewest variables can be incorporated into the models with more activatable subunits to compare models to experimental data and check the validity of the overall schemes.

The starting point for the modeling of I_{Ks} activation kinetics is the application of a Hodgkin-Huxley type system to the behavior of the different E160R constructs. **Scheme 1, A-C**, are Markov diagrams for the state transitions of four-VS, two-VS, and single-activatable VS channels, based on the Hodgkin-Huxley model of independent gating particle movement, α and β rate constants, and the idea that concomitant activation of the available gating particles is sufficient for channel pore opening (Hodgkin and Huxley, 1952). Subscripts to closed (C_a) and open (O_a) channel states indicate the individual subunit states, resting (R) or activated (A). The advantage of restricting individual subunit activation with the E160R mutation is that models are simplified, and ultimately, with three E160R subunits in a channel complex, activation/opening comprises only a single transition for which rate constants can be analytically derived from experimental data.

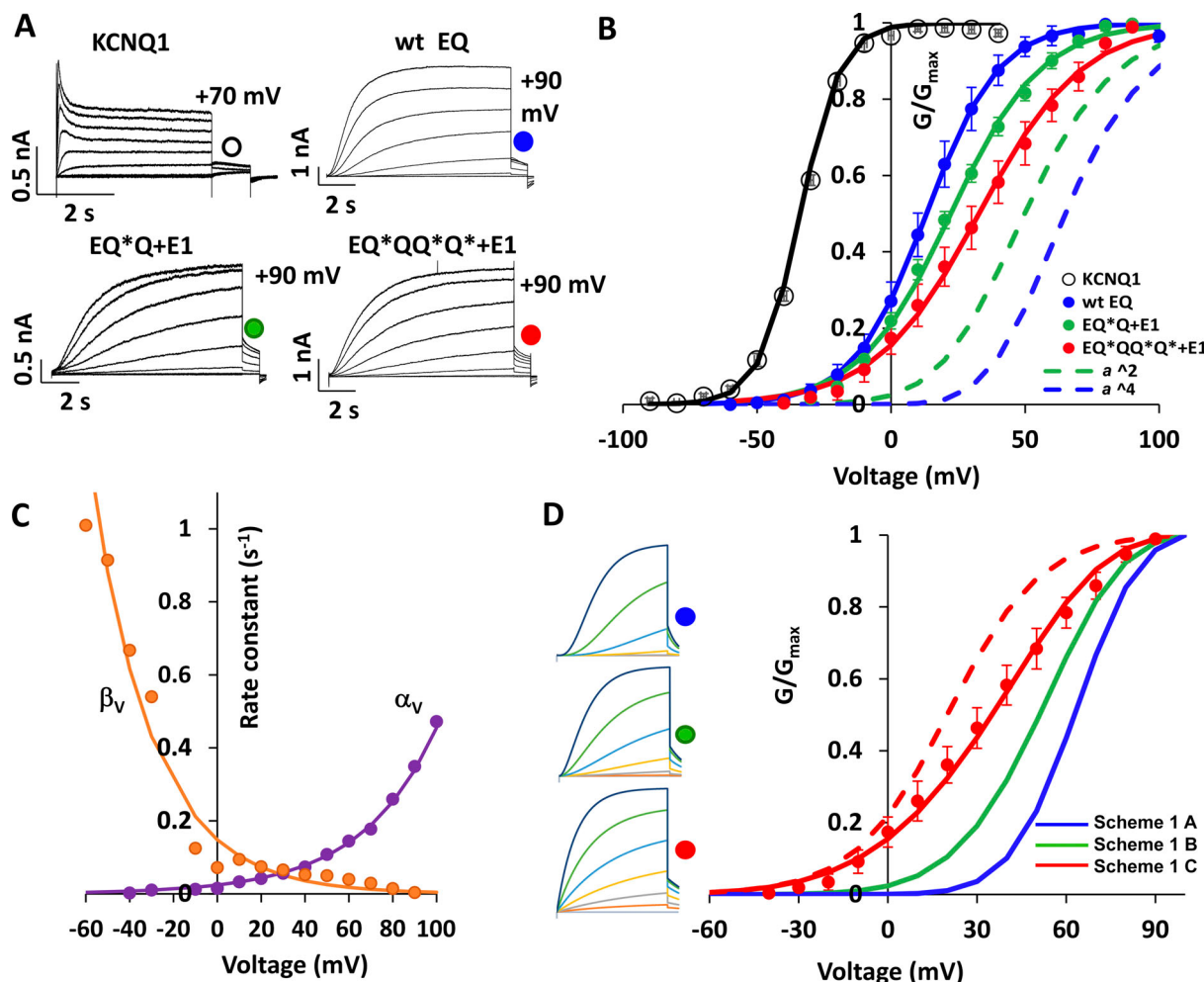


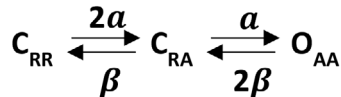
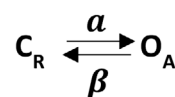
Figure 1. Whole-cell experiments and Scheme 1 simulations for wt (EQ) and mutant I_{Ks} with two (EQ*Q+E1) or three (EQ*QQ*Q*+E1) E160R mutations. (A) HMR1556-subtracted currents (except KCNQ1) from tsA201 cells recorded during 10-s (4 s for KCNQ1) pulses in 20 mV steps to between -80 mV and indicated values, then to -40 mV for 1 s. Holding potential was -90 mV and a 4-s prepulse to -120 mV was applied before each step (see Fig. S1). $V_{1/2}$ s and k are as follows: for KCNQ1 (-37.6 , 7.0 mV); EQ (12.4 , 11.1 mV); EQ*Q+E1 (22.3 , 16.6 mV); and for EQ*QQ*Q*+E1 (29.1 , 19.1 mV). (B) Mean tsA201 cell G-V data (symbols) fit with unconstrained Boltzmann distribution, for KCNQ1 alone (black; $V_{1/2} = -33.9$ mV, $k = 7.6$ mV, $n = 3$), wt EQ (blue; $V_{1/2} = 13.2$ mV, $k = 13.5$ mV, $n = 8$), EQ*Q+E1 (green; $V_{1/2} = 22.3$ mV, $k = 16.8$ mV, $n = 5$), and EQ*QQ*Q*+E1 (red; $V_{1/2} = 32.8$ mV, $k = 19.4$ mV, $n = 5$). Data are summarized in Table 1. Dashed lines show predicted G-V relationships using Eq. 2 with $V_{1/2} = 32.8$ mV and $k = 19.4$ mV as a varies with the number of VSs ($a = 4$ blue, $V_{1/2} = 66.4$ mV and $k = 14.6$ mV; $a = 2$ green, $V_{1/2} = 50.8$ mV and $k = 16.2$ mV). Error bars represent mean \pm SEM. (C) Rate constant plots for α_v and β_v calculated from EQ*QQ*Q*+E1 data. Lines fit to data with Eq. 1. For fit parameters see Table 2, row 1. (D) Isochronal Scheme 1 simulations using optimized rate constants (Table 2, row 2). EQ*QQ*Q*+E1 10 s data G-V (red circles) and optimized Scheme 1 C fit (red line, $V_{1/2} = 33.5$ mV, $k = 18.2$ mV). Dashed red line depicts the Scheme 1 C G-V expected from a 50-s pulse ($V_{1/2} = 19.8$ mV, $k = 15.3$ mV). The Scheme 1 B simulation (green, $V_{1/2} = 50.2$ mV, $k = 13.2$ mV) and Scheme 1 A simulation (blue, $V_{1/2} = 62.5$ mV, $k = 10.0$ mV) are shown. Insets show example sets of Scheme 1 model currents, $+90$ to -10 mV in 20 mV steps.

Downloaded from https://jgpress.org/jgp/article-pdf/156/3/202313465/jgp-202313465.pdf by guest on 22 May 2023

In the simplest case in which there are three E160R-containing VS subunits in the complex and the remaining activatable subunit only undergoes a single transition (Scheme 1 C), the Po-V relationship, the τ_{act} -V, and the τ_{deact} -V are uniquely defined by the forward and backward rate constants between the resting and activated channel states. Current records (Fig. 1 A) were fit with an exponential starting at 0.5 s, which omits the early current at the start of the records, and activation time constants (τ_{act}) extracted and plotted against the membrane potential (Fig. 2 A). Tail currents were obtained using a two-pulse protocol and fit with a single exponential decay function to provide data points at negative potentials. Using 10 s isochronal G-V data for EQ*QQ*Q*+E1 (Fig. 1 B), the exponential voltage-

dependence of the rate constants, α_v and β_v (Fig. 1 C), and the apparent valence of the forward and backward transitions were obtained by calculation and fitting (Eq. 1 and Table 2). Constants were optimized together using custom-written MATLAB programs and library solvers (see Materials and methods) to minimize the error between model and experimental fits to G-V, τ_{act} -V data, and between model and current tracings at $+30$ mV (rates in Table 2). The analytical fits to the experimental data are shown as dashed lines and the optimized model fits as solid lines (Fig. 2).

The forward (α) and backward (β) rate constants versus voltage functions obtained from the fitting described above were incorporated into MATLAB models and used to simulate

Scheme 1 A**Scheme 1 B****Scheme 1 C**

Scheme 1. Sequential Hodgkin-Huxley type activation gating models incorporating independent VS movement for wt channels (Scheme 1 A), channels with two E160R-containing VS ($\text{EQ}^*\text{Q}^*\text{E1}$, Scheme 1 B), and channels with three E160R-containing VS ($\text{EQ}^*\text{QQ}^*\text{Q}^*\text{E1}$, Scheme 1 C). Channel states are represented as closed (C) and open (O). For each VS, subscript R denotes those in the rest state and A denotes those in the activated state. Note that when all subunits are activated the channel is open.

isochronal G-V relationships and currents for the $\text{EQ}^*\text{QQ}^*\text{Q}^*\text{E1}$ (Scheme 1 C), $\text{EQ}^*\text{Q}^*\text{E1}$ (Scheme 1 B), and wt (Scheme 1 A) constructs (Fig. 1 D and Table 1), and the predicted steady-state G-V relationship for $\text{EQ}^*\text{QQ}^*\text{Q}^*\text{E1}$ after 50 s pulses (dashed line, Fig. 1 D). The curves generated overlaid the experimental data from the single activatable subunit construct and the dashed curves predicted from Eq. 2 for the other constructs, and they also provided a good fit to current records for the $\text{EQ}^*\text{QQ}^*\text{Q}^*\text{E1}$ construct in minimizing the difference currents between the experiment and model (Fig. 2 C). Scheme 1 models are highly constrained in that the last VS to move also comprises the gate, and the rate constant for the closed-to-opening transition has to be identical to that for moving a VS. Structural studies show that these events are not identical and thus that the rate constants are unlikely to be identical. Despite the constraints, these models reproduce much of the simple kinetic data obtained from an I_{Ks} channel with only one activatable VS domain and predict the slope changes in the isochronal G-V when the channel complex

contains two or four activatable VSs. However, the models do not predict the progressive hyperpolarization of the G-V seen with two or more activatable subunits (Fig. 1 B) or the slower deactivation of tail currents (Fig. 1 A), and the model currents for $\text{EQ}^*\text{QQ}^*\text{Q}^*\text{E1}$ (Fig. 2 C) do not show the delay in activation before the exponential rise of current seen experimentally (Fig. 1 A). These differences suggest that Hodgkin-Huxley models, while supporting the idea that the E160R mutation can immobilize VS domains, fail to reproduce both central properties (G-V shifts) and more subtle behaviors of the I_{Ks} constructs. Thus, experiments are needed that provide a more complete description of activation kinetics along with further development of more representative activation models.

Minimum activation time of I_{Ks} channels with one, two, or four activatable VS domains

The I_{Ks} activation time course can be defined precisely for Hodgkin-Huxley models, and thus also the delay from when

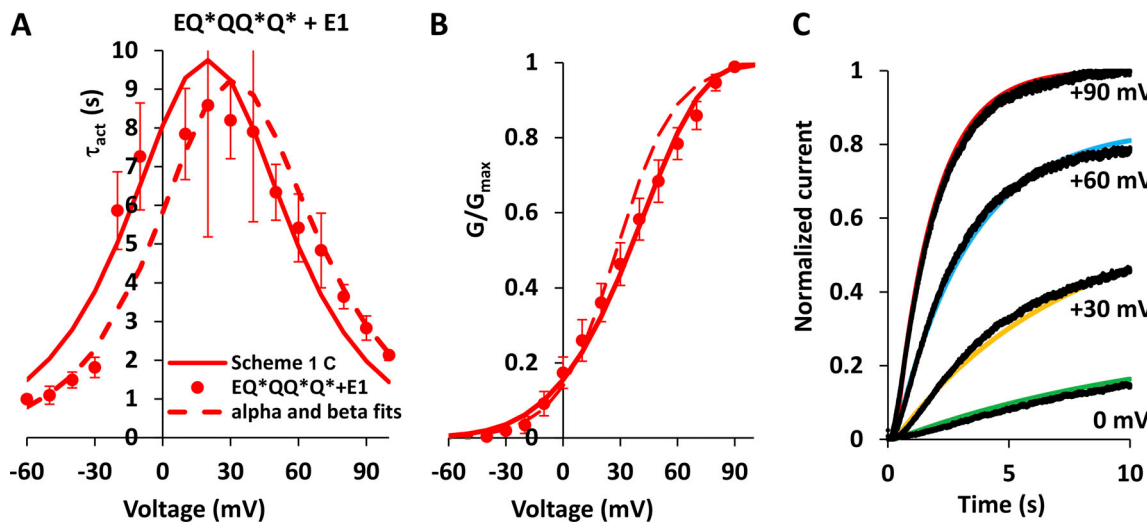


Figure 2. Optimization of Scheme 1 C models for mutant I_{Ks} with three E160R mutations ($\text{EQ}^*\text{QQ}^*\text{Q}^*\text{E1}$). (A) Activation time constants versus step voltage relationship ($\tau_{\text{act}}\text{-}V$) for HMR1556-subtracted $\text{EQ}^*\text{QQ}^*\text{Q}^*\text{E1}$ data. $\tau_{\text{act}}\text{-}V$ plots for tsA201 experimental data (red circles), the analytical fit to data (dashed red line), and optimized Scheme 1 C model fit (solid red line). The experimental data were obtained from exponential fits to deactivating tail currents between -30 and -60 mV and for fits to activating currents between -20 and $+100$ mV. The model time constants were obtained from exponential fits to the activating model currents. (B) Optimization of $\text{EQ}^*\text{QQ}^*\text{Q}^*\text{E1}$ G-V plot. 10-s isochronal experimental data (red circles, $V_{1/2} = 32.8$ mV, $k = 19.4$ mV), the analytical fit to data (dashed red line, $V_{1/2} = 28.1$ mV, $k = 15.4$ mV), and optimized 10 s Scheme 1 C model fit (solid red line, $V_{1/2} = 33.5$ mV, $k = 18.2$ mV, Table 1). (C) Simulated currents obtained using Scheme 1 C with optimized tsA201 experimental rate constants (Table 2, row 2) overlain with $\text{EQ}^*\text{QQ}^*\text{Q}^*\text{E1}$ current recordings (black) obtained using the protocol in Fig. 1 A for 10-s pulses. Currents and simulations are normalized to the peak values at $+90$ mV. Model fits are matched to the start of exponential relaxation in the current records.

Table 2. Transition rate constants for I_{Ks} models

Model	$\alpha(0)$ (ms ⁻¹)	$\beta(0)$ (ms ⁻¹)	$\delta(0)$ (ms ⁻¹)	$\gamma(0)$ (ms ⁻¹)	$\kappa(0)$ (ms ⁻¹)	$\lambda(0)$ (ms ⁻¹)	$z\alpha(e_0)$	$z\beta(e_0)$	$z\delta(e_0)$	$z\gamma(e_0)$	$z\kappa(e_0)$	$z\lambda(e_0)$	
(1) EQ*QQ*Q [*] + E1 Whole-cell patch clamp	2.38e-5	1.48e-4										7.45e-1	-9.0e-1
(2) EQ*Q [*] Q [*] + E1 Optimized for Scheme 1 C model	2.678e-5	9.704e-5										8.63e-1	-8.56e-1
(3) Scheme 1 B, EQ*Q+E1 model, optimized	1.201e-4	9.527e-5										4.860e-1	9.195e-1
(4) Scheme 1 A, wt EQ model, optimized	2.567e-4	8.227e-5										4.636e-1	9.161e-1
(5) G219C psQQ [*] +E1 fluorimetry	4.817e-3	1.596e-4	3.354e-4	3.893e-4								4.50e-1	-4.50e-1
(6) G219C psQQ [*] +E1 Voltage clamp fluorimetry	4.255e-3	1.6e-4	1.363e-4	3.895e-4								4.833e-1	5.38e-1
(7) Scheme 2 A, psQ+E1, optimized	9.63e-4	3.19e-5	1.34e-4	1.56e-4								4.50e-1	-4.50e-1
(8) Scheme 2 B, psQQ [*] +E1, optimized	8.51e-4	3.19e-5	5.45e-5	1.558e-4								4.833e-1	6.99e-1
(9) Scheme 4 allosteric models, optimized, D = 1.357	8.71e-4	2.43e-5	2.88e-5	6.92e-5								4.75e-1	-4.34e-1
Mean rates, n = 5 ± SEM	9.23e-4 ± 4.92e-5	2.60e-5 ± 1.32e-6	4.42e-5 ± 1.03e-5	1.54e-4 ± 5.73e-5								4.87e-1 ± 0.009	6.89e-1 ± 0.011
(10) Scheme 5 allosteric models, optimized	9.64e-4	3.19e-5	1.042e-4	1.298e-4	6.033e-5	7.79e-5	4.50e-1	-4.50e-1				5.38e-1	-5.38e-1
Mean rates, n = 4 ± SEM	9.55e-4 ± 1.84e-5	3.29e-5 ± 3.90e-7	1.152e-4 ± 1.27e-5	1.214e-4 ± 9.486e-6	7.455e-5 ± 5.41e-6	5.844e-5 ± 8.84e-6	4.76e-1 ± 0.011	-4.61e-1 ± 0.004	5.96e-1 ± 0.024	6.15e-1 ± 0.038	6.03e-1 ± 0.030	-5.67e-1 ± 0.013	
(11) Scheme 5 B, T_{act} and Δt optimized	2.89e-3	9.57e-5	5.21e-5	6.49e-5	1.82e-4	2.34e-4	4.50e-1	-4.50e-1	5.38e-1	-5.38e-1	3.23e-1	-5.38e-1	
(12) Scheme 5 C, T_{act} and Δt optimized	3.85e-3	1.28e-4	3.473e-5	4.333e-5	3.03e-4	3.89e-4	4.50e-1	-4.50e-1	5.38e-1	-5.38e-1	4.30e-1	-5.38e-1	

Rate constants obtained directly from fits to experimental data and modified rate constants obtained after model optimization, as indicated. For Schemes 4 and 5 models, the single best optimization result as determined by "fval" (MATLAB) the minimum value of the objective function at the solution, is shown, as well as mean data from a number of optimization runs starting from different initial parameter values. The best solution was used to generate plots for Schemes 4 and 5 models. Optimizing transition kinetics used G-V, F-V, t_{act} -V, Δt -V experimental data, and the F2/F1 ratio (see Materials and methods).

channels are displaced from resting states until they enter the open state (Hodgkin and Huxley, 1952; Colquhoun and Hawkes, 1977). For a channel with a single activatable subunit, the occupancy of the open state should mirror the rise in conductance, with no delay, and as more activatable subunits are present, the delay (Δt) increases as a function of the natural logarithm of the number of subunits (a):

$$\Delta t = \ln(a) * \tau_{act}, \quad (3)$$

where τ_{act} measures the exponential current relaxation after the activation delay (Horrigan et al., 1999). Δt can be measured by using a negative enough holding potential to ensure channels are in ground-closed states where all VS domains are fully in their resting conformations and then fitting the exponential current increase during a depolarizing step back to zero current to measure the time delay from pulse initiation. In a similar manner to other authors in oocytes (Tzounopoulos et al., 1998), we tested how holding potential modulated the residence of wt I_{Ks} channels in resting closed states in mammalian cells (Fig. S2 A), extending holding potentials more negative to those in our prior study (Westhoff et al., 2017). From a holding potential of -90 mV, tsA201 cells were pulsed between -40 and -180 mV for 2 s and then current activation was recorded during a subsequent 4 s step to $+80$ mV. Normalized individual data sets and the overall mean values of the time delay (Δt) between the $+80$ -mV step initiation to exponential current activation as a function of prepulse voltage suggest that the maximum activation delay is reached at a prepulse potential of about -140 mV. However, this holding voltage was not well tolerated by tsA201 cells. We settled on a holding potential of -120 mV for our experiments, at which voltage Δt values reached 96% of their maximum (Fig. S2 B). This holding potential is sufficient to place channels into or close to their ground-closed configurations, especially if used continuously, and therefore appropriate to use as the holding potential or prepulse potential for Δt experiments.

Using HMR1556-subtracted currents, it was relatively straightforward to fit the current time course at positive potentials with an exponential function and obtain Δt for wt EQ channel currents (Fig. 3 A). It is clear that for this construct, $\Delta t \neq 0$ as exponential fits to current activation intersect the time axis at positive time values after the initiation of the voltage step. It was difficult to fit exponentials to activating currents at potentials negative to -20 mV, even during 20-s depolarizations due to extremely slow activation of I_{Ks} , so tail current deactivation rates were used to obtain time constants between -30 and -60 mV. The averaged bell-shaped activation time constant–voltage relationships (τ_{act} –V) for the three constructs are shifted in a hyperpolarizing direction with more active VSs (Fig. 3 B). We extended the τ_{act} –V relations to $+180$ mV to compare the relative time constants of activation for the three constructs at voltages where the forward rate constant would define the speed of the opening transition. The experimental data diverge from the red, green, and blue Scheme 1 curves which converge as the opening time constant reduces to $1/\alpha$ in each case. Instead, the τ_{act} –V ratios relative to wt remain relatively constant at potentials positive to $+50$ mV, with τ_{act} ratios of ~ 0.5 – 0.6 for wt/EQ*Q+E1, and ~ 0.4 for wt/EQ*QQ*Q*+E1 (Fig. 3 B, inset).

The Δt –V relationships have a shallower dependence on pulse potential than the time constants and are displaced upwards to longer delay values as more activatable VSs are present in the construct (symbols in Fig. 3 C), although this is only significant between wt EQ and the other constructs. Peak values are at ~ 0 mV for wt and $+20$ to $+30$ mV for EQ*Q+E1 and EQ*QQ*Q*+E1, which are close to the isochronal $V_{1/2}$ s for each construct (Fig. 1 B), as expected if Δt bears a fixed relationship to the activation time constants. When the Δt values are plotted against τ_{act} (symbols in Fig. 3 D), the fast time constants of current activation at more positive potentials than $+50$ mV correlate with shorter Δt values, but overall the relationships are non-linear, τ_{act} increases (slower activation) while Δt values appear to plateau closer to the $V_{1/2}$ and negative potentials. At the higher potentials between $+60$ and $+150$ mV for wt EQ data, the maximum slope of $\Delta t / \tau_{act}$ was 0.336 ($R^2 = 0.96$).

The optimized rate constants from the Scheme 1 C model described in Fig. 1 (Table 2, row 2) were used as seed values in optimizing Scheme 1 B and Scheme 1 A models by simultaneous least squares fitting to the experimental G–V and τ_{act} –V relationships for wt and EQ*Q+E1, and the final rate constants for these two models are shown in Table 2, rows 3 and 4. The activation time courses of simulated currents produced by the final Scheme 1 model were fit with exponential relationships in the same way as the experimental current records were fit to obtain model τ_{act} and Δt values. Optimized Scheme 1 τ_{act} –V, Δt –V, Δt – τ_{act} , and G–V model curves are shown as solid lines overlaying wt, EQ*Q+E1, and EQ*QQ*Q*+E1 experimental data points (Fig. 3, B–D; and Fig. S3 A). Clearly, while the model τ_{act} –V and G–V curves are good fits, none of the model Δt –V curves are good fits to the experimental data (Fig. 3 C), and for the Scheme 1 C model, Eq. 3 predicts Δt values of zero across the voltage range (red line in Fig. 3 C). Scheme 1 B and Scheme 1 A models output Δt –V curves of a similar shape to those found experimentally but displaced upwards to longer delay times, and these model differences are carried over to the Δt – τ_{act} relationships (Fig. 3 D).

The activation delay times found experimentally are about half those expected from the Scheme 1 models and one-quarter of expected values from Eq. 3 for the measured exponential relaxation time constants, and may be compared with a value of 0.12 for BK channels previously reported (Horrigan et al., 1999). The classical explanation would be that a much slower process or processes slow current activation beyond the time taken for equilibration of the closed state transitions. More representative models of this type would then require additional steps in the activation process, such as extra or concerted transitions. Alternatively, only one subunit may be required to activate for the channel to open and current to begin its exponential trajectory, irrespective of the number of subunits available for this process, so that the activation delay, Δt , is less than expected from the Scheme 1 models. Notably, this latter idea cannot explain the activation delays found in the EQ*QQ*Q*+E1 channel (red points in Fig. 3 C) with only one active VS, which undergoes a single activating transition.

The model simulations bring up another interesting quirk in the delay Δt versus τ_{act} relationships, which, according to Eq. 3, should be linear with slopes $\ln(a)$. Neither the experimental nor

the model $\Delta t - \tau_{act}$ relationships are straight lines, and we hypothesized this was related to fitting relatively slow time constants to current data obtained from 10-s test pulses. We examined this possibility using the **Scheme 1 B** and **Scheme 1 A** models (Fig. S3 B). Simulated currents during 4–100 s pulses were fit with exponentials to extract τ_{act} and Δt . It appears that longer test pulses improve the linearity of $\Delta t - \tau_{act}$ relationships which reach steady state with pulses of a 50-s duration or longer. The time constant fits from 10 s pulses deviate from this steady-state relationship with τ_{act} values >2 s. Regression lines fit to the initial steep regions of the model 50 s $\Delta t - \tau_{act}$ relations gave slopes of 1.35 and 0.62 for **Scheme 1 A** and **Scheme 1 B**, respectively ($R^2 = 0.99$ in each case), which compare favorably with the theoretical values from Eq. 3 of 1.39 and 0.69 (Fig. S3 B). The slight underestimations are hypothesized to reflect errors in the automatic fitting of model currents and estimations of Δt . It appears that the non-linearity of the experimental relationships is partly due to the inability to accurately measure $\Delta t - \tau_{act}$ from fits to currents during 10–20 s depolarizations, but this does not explain the deviation of the experimental $\Delta t - \tau_{act}$ curves from the **Scheme 1** model curves, especially at the shorter values of τ_{act} .

Kinetics of VS displacement during activation determined directly using VCF

The observed activation delay after the initiation of the step voltage pulse (Fig. 3 A), suggests the existence of multiple activation steps even for channels with a single activatable VS and fits well with prior literature that divides the movement of each VS into at least two independent steps with their own resolvable fluorescence components, F1 and F2 (Osteen et al., 2010; Zayzman et al., 2014; Barro-Soria et al., 2014; Westhoff et al., 2019). In **Scheme 2** models, F1 forward and reverse kinetics are associated with voltage-dependent activating transitions with rates α and β , and F2 kinetics are represented by a concerted transition associated with channel opening, and opening and closing rates δ and γ , respectively.

To measure fluorescence and separate the fluorescence components in oocytes, we used a single C214A/G219C/C331A-Q1 pseudo-wildtype construct (psQ) that contains a labelable cysteine, 219C, at the top of the S4 (Fig. 4), or two Q1 subunits in a tandem linked psQQ with a 219C at the top of the S4 of one of the pairs of Q1s. Using Alexa Fluor 488 C₅-maleimide allowed tracking of VS environment changes during activation of the I_{Ks} channel. To examine the effect of reducing the number of activatable subunits on the F1 and F2 components of VS activation, a dimeric construct was developed that has two E160R-containing VS subunits when it assembles as a tetramer (psQ-E160R Q*, psQQ*-E1 in Fig. 4 A). Previously, we had compared activation data from psQ*Q and psQQ* and found no difference (Westhoff et al., 2019), so here we only use psQQ*-E1. For psQQ*, the presence of the labelable G219C in subunits not containing E160R ensured that the two activatable subunits in the complex could be labeled with the fluorophore Alexa Fluor 488. Unfortunately, it was not possible to record fluorescence from constructs with E160R mutations in three VSs due to difficulties with the synthesis and expression of protein from very large

cRNA molecules, so we were limited to the study of psQ, psQQ, and psQQ* constructs. We also tested how prepulse voltage modulated the residence of psQQ+E1 and psQQ*-E1 channels in resting closed states in oocytes. Either the activation half-time (Fig. S4, A and B) for psQQ+E1 and psQQ*-E1 channels or the activation delay, Δt , for psQQ+E1 channels (Fig. S4, C and D) was measured after 5-s prepulses to between −160 and −40 mV. It was noted that the activation half-times of psQQ*-E1 channels were less dependent on the prepulse voltage than the half-times or Δt values for psQQ+E1. This is likely due to the restriction on activation of two of the four VSs in the psQQ*-E1 channels. Nevertheless, in channel constructs using the two methods, a prepulse voltage of −140 mV was sufficient to place channel complexes in resting closed states, and so this prepulse potential was used in experiments to determine the F1 and F2 components of VS fluorescence during activation gating.

Current and fluorescence records are shown for voltage steps from −140 mV to between −180 and +80 mV (Fig. 4 A). After subtraction of the fluorescence baseline (the −140 mV step), which corrected for photobleaching during the pulse, fluorescence records during activation were fit with either one or two exponentials, depending on the step voltage, which allowed separation of data into F1 and F2 components. The graph in Fig. 4 B summarizes the peak fluorescence values as a function of potential along with G-V relations for the psQ+E1 and psQQ*-E1 constructs (G-V only shown for psQQ+E1). The experimental F-V and G-V relations are shown as symbols, the G-V and F-V fits as lines, with the component F1-V and F2-V relationships as broken lines. The F1-V relationships were not clearly separable for the psQ+E1, psQQ+E1, and psQQ*-E1 constructs, with $V_{1/2}$ s of −96.9, −88.2 (not shown), and −86.5 mV, respectively (Table 1). However, the F2-Vs tracked closely with the respective G-V relationships for the specific constructs. The $V_{1/2}$ s of the G-V and F2-V for psQ+E1 were 4.2 and 3.0 mV, and for psQQ*-E1 were 23.5 and 21.0 mV, respectively. This tracking of F2 with the G-V has been described previously for pseudo-wt KCNQ1+KCNE1 channels, so was not unexpected in the present experiments (Osteen et al., 2010; Zayzman et al., 2014; Barro-Soria et al., 2014).

The $V_{1/2}$ separation between the G-V relationships for psQ+E1 and psQQ+E1 channels compared with that for psQQ*-E1 channels with only two activatable subunits is preserved in a similar manner to that observed in the mammalian cell expression system (Fig. 1 and Table 1) and is accompanied by a hyperpolarizing shift in the F2 component of fluorescence emission in wt, but minimal change in the voltage-dependence of the F1 component. This suggests that the major F1 component of fluorescence and consequently VS activation is independent and unaffected by the presence or otherwise of fixed and/or mobile adjacent VS domains. In contrast, the displacement of the F2-V to more depolarized potentials in the presence of E160R subunits suggests that this secondary VS movement is constrained by the presence of non-activatable subunits within the same channel complex or is tied in some more complex manner to the G-V, opening of the channel gate and development of conductance. Interestingly, it was also noted that the proportion of the total fluorescence signal attributable to F1 decreased from 80% in wt to 57% in psQQ*-E1. This can be clearly inferred from the time

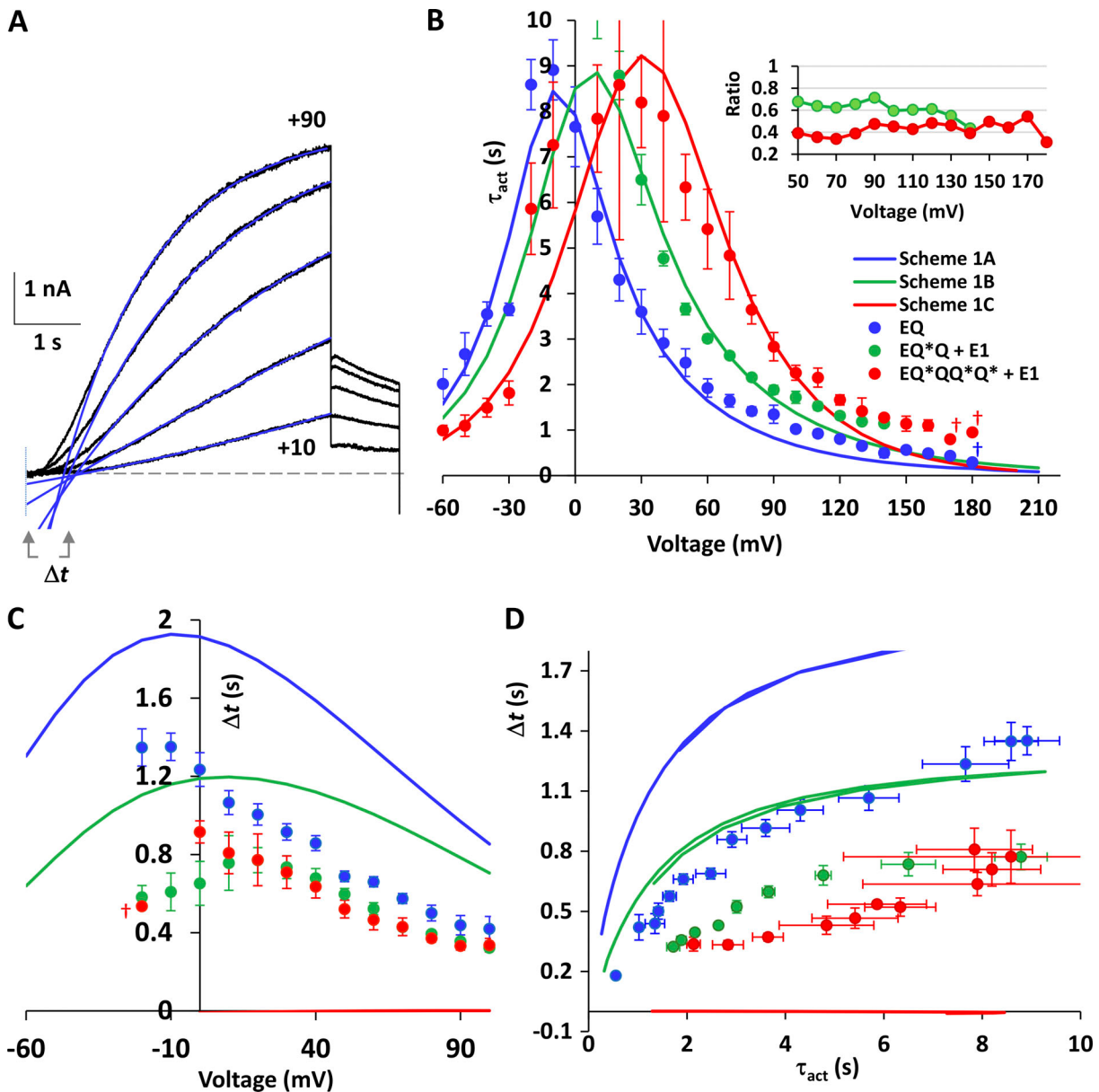


Figure 3. Activation delay (Δt) and exponential relaxation (τ_{act}) relationships with Scheme 1 model fits. **(A)** HMR1556-subtracted tsA201 cell EQ currents (black traces) in 20-mV steps from +10 to +90 mV. Holding potential was -90 mV, with a 4-s prepulse to -120 mV (not shown). Exponential fits to the activation time course after a delay are shown as overlaid blue lines. Activation delay (Δt) is the time from pulse onset to where exponential fits (blue lines) intersect the dashed line representing zero current. **(B)** Exponential activation of I_{Ks} (τ_{act}) after delay versus activation step potential. Mean tsA201 cell data, blue (wt, $n = 6-18$), green (EQ^*Q+E1 , $n = 4-7$), and red ($EQ^*QQ^*Q^*+E1$, $n = 2-17$), from exponential fits to currents during 4–20 s depolarizations from -20 to +180 mV. Data at -60 to -30 mV are from tail currents. Holding potential was -90 mV, with a 4 s -120 mV prepulse (except some data at ≥ 110 mV). Curves are fits from Scheme 1 models. Inset shows the ratio of τ_{act} in control to EQ^*Q+E1 , and to $EQ^*QQ^*Q^*+E1$. wt data includes 2 QQ+E1 and 3 QQQQ+E1 cells. \dagger denotes $n < 3$. **(C)** Δt versus activation step potential, -20 to +100 mV. wt EQ (blue, $n = 5-13$), EQ^*Q+E1 (green, $n = 4-7$), and $EQ^*QQ^*Q^*+E1$ (red circles, $n = 2-6$). 10–20 s pulse data. Curves are fits from Scheme 1 models. **(D)** Plot of Δt versus τ_{act} , symbols as for B and C. Data are for voltages from -20 to +100 mV. Lines in panels B–D show optimized fits from Scheme 1 A, (blue) 1 B (green), and 1 C (red) models.

Downloaded from https://jgpress.org/jgp/article-pdf/159/3/202313465.pdf by guest on 22 May 2023

course of fluorescence tail decay at -40 mV (Fig. 4 A, lower). The psQ+E1 tails are quite well maintained at -40 mV, as expected if the majority of the fluorescence signal is accounted for by the F1 component, whereas the total psQQ*+E1 signal decays much more. This relative increase of the F2 component compared with F1, in the presence of E160R-containing subunits, is also suggestive that this component of fluorescence may not arise entirely from VS movements alone.

We analyzed the kinetics of the separate fluorescence components in terms of two transitions for independent VSs, according to Scheme 2. The time constants for relaxation of F1 and F2 were obtained from mono-exponential or biexponential fits to the fluorescence traces at different potentials (Fig. 5, A and B; and Materials and methods), and with the steady-state, F1-V and F2-V were used to calculate α , β (for F1, Fig. 5, C and D) and δ , γ (for F2, Fig. 5, E and F) for psQ+E1 and psQQ*+E1 as a function of

potential. The kinetic parameters that define the curves may be found in **Table 2**, and the psQ+E1 data are consistent with values reported previously (in brackets) with $\alpha_0 = 4.8e-3 \text{ ms}^{-1}$ (4e-3 ms^{-1}), $\beta_0 = 1.6e-4 \text{ ms}^{-1}$ (9.1e-5 ms^{-1}), $\delta_0 = 3.4e-4 \text{ ms}^{-1}$ (2.6e-4 ms^{-1}), and $\gamma_0 = 3.9e-4 \text{ ms}^{-1}$ (1.18e-4 ms^{-1}), considering these authors used slightly different methods to obtain the time constants for F1 and F2 ([Barro-Soria et al., 2014](#)).

Simulations of oocyte fluorescence data incorporating two VS transitions

The experimentally derived kinetic parameters from the psQ+E1 and psQQ^{*}+E1 fluorescence F1-V and the F2-V (**Fig. 5**), summarized in **Table 2**, were incorporated into **Scheme 2, A and B**, models (below), assuming independent transitions for each VS subunit (reflected in F1 and the α, β rate constants) followed by a second, shared, coordinated transition that leads to channel opening (reflected in F2 and the δ, γ rate constants). The fluorescence emission for an α transition versus a δ transition was either set as f1:1 or f1:2 (one-to-one or twice the fluorescence emission for an F2 versus an F1 transition). Isochronal model F-V and G-V curves simulated using these rates are shown overlying the experimental data (symbols, **Fig. 6 A**). For psQ+E1, **Scheme 2 A** with f1:1, the model fits overlay the F-V data extremely well and also simulates the voltage-dependence of the G-V exactly. The modeled F-V determined using f1:2 is shown as the long-dash blue line and is displaced below the experimental data as expected if the fluorescence contribution from F2 is being overestimated. In contrast to this result, the simulations using **Scheme 2 B** show a much better fit to experimental data with the F-V modeled using f1:2. This correlates with the observation made experimentally (**Fig. 4**) that the F2 fluorescence component comprised a larger proportion of the total fluorescence in the psQQ^{*}+E1 mutant than in psQ+E1. With the F-V modeled using f1:2, the F1, F2 components, and the G-V also show an excellent correlation with the experimental data.

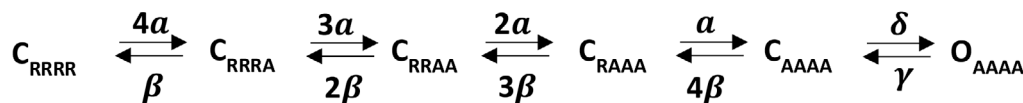
The delay (Δt) and exponential current relaxation kinetics (τ_{act}) of the oocyte currents (open circles in **Fig. 6 B**) were very similar to the mammalian cell data previously described (filled circles in **Fig. 6 B**, from **Fig. 3 D**), but the transient kinetics were not well fit by model simulations using the experimental rates from the VCF experiments or the F1 and F2 rate constants from [Barro-Soria et al. \(2014\)](#), shown by dashed lines (**Fig. 6 B**), which model Δt versus τ_{act} from -20 to +100 mV. To reproduce the

transient kinetics, rate constants for both VS transitions needed to be optimized in **Scheme 2, A and B**, models (**Table 2**). This required slower rate constants for F1 and F2 transitions, which gave the Δt and τ_{act} graphs (continuous lines in **Fig. 6 B**), and model currents and fluorescence (**Fig. 6 C**), without altering the steady-state kinetics, which were already well fit by the experimentally derived rate constants. The model current tracings show appropriate activation delay and activation time constants in psQQ^{*}+E1 (**Scheme 2 B**) compared with psQ+E1 (**Scheme 2 A**), reflecting the model relationships between Δt and τ_{act} for the two schemes (**Fig. 6 B**). It is not clear why the kinetic parameters from the fluorescence experiments require scaling and do not directly reproduce the delay and exponential activation of currents. It is likely that the 5-s duration fluorescence test pulses are too short to measure F2 time constants accurately from small signals and reproduce current relaxation time constants in the 10 s range, but this does not explain why modeled Δt measurements, which predominantly reflect the F1 transition, do not reproduce experimental activation delays well.

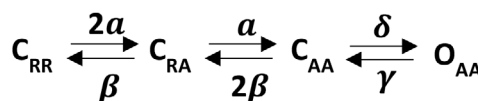
Although these models produce excellent fits to the data, neither set of rates used in both models reproduce the G-V shift seen experimentally, nor the persistently slower activation time constants at positive potentials in EQ^{*}Q+E1 versus wt constructs (**Fig. 3 B**). The **Scheme 2** results described above were obtained using either a four-state model simulating psQQ^{*}+E1 or a six-state model simulating psQ+E1. In these models, the independently moving VSs are assumed to undergo a first transition from rest, followed by a second coordinated transition of all four activated subunits that induce channel opening. However, published experimental data describing two VS movements in I_{K_s} do not explicitly demonstrate direct coupling of the second VS movement to the channel opening step ([Zayzman et al., 2014](#); [Barro-Soria et al., 2014](#); [Westhoff et al., 2019](#); [Hou et al., 2020](#)), and this raises the possibility that separation of these two events might better predict the current kinetics and the hyperpolarization of the G-V seen in psQQ+E1 compared with the two active VS channel psQQ^{*}+E1.

The incorporation of two independent VS transitions, separated from the coordinated opening transition, in our models with four (**Scheme 3 A**) or two (**Scheme 3 B**) activatable VSs, uses fluorescence rate constants from psQ+E1 and psQQ^{*}+E1 experiments in a similar manner to the **Scheme 2** models (**Fig. 7**). Plots of Δt versus τ_{act} show similarly fast time constants of

Scheme 2 A



Scheme 2 B



Scheme 2. Sequential models for psQ+E1 (**Scheme 2 A**) and for psQQ^{*}+E1 (**Scheme 2 B**) including a single concerted opening transition defined by δ and γ rates. Channel states are represented as closed (C) and open (O). Subscript R denotes VS in the rest state and A denotes those in the activated state.

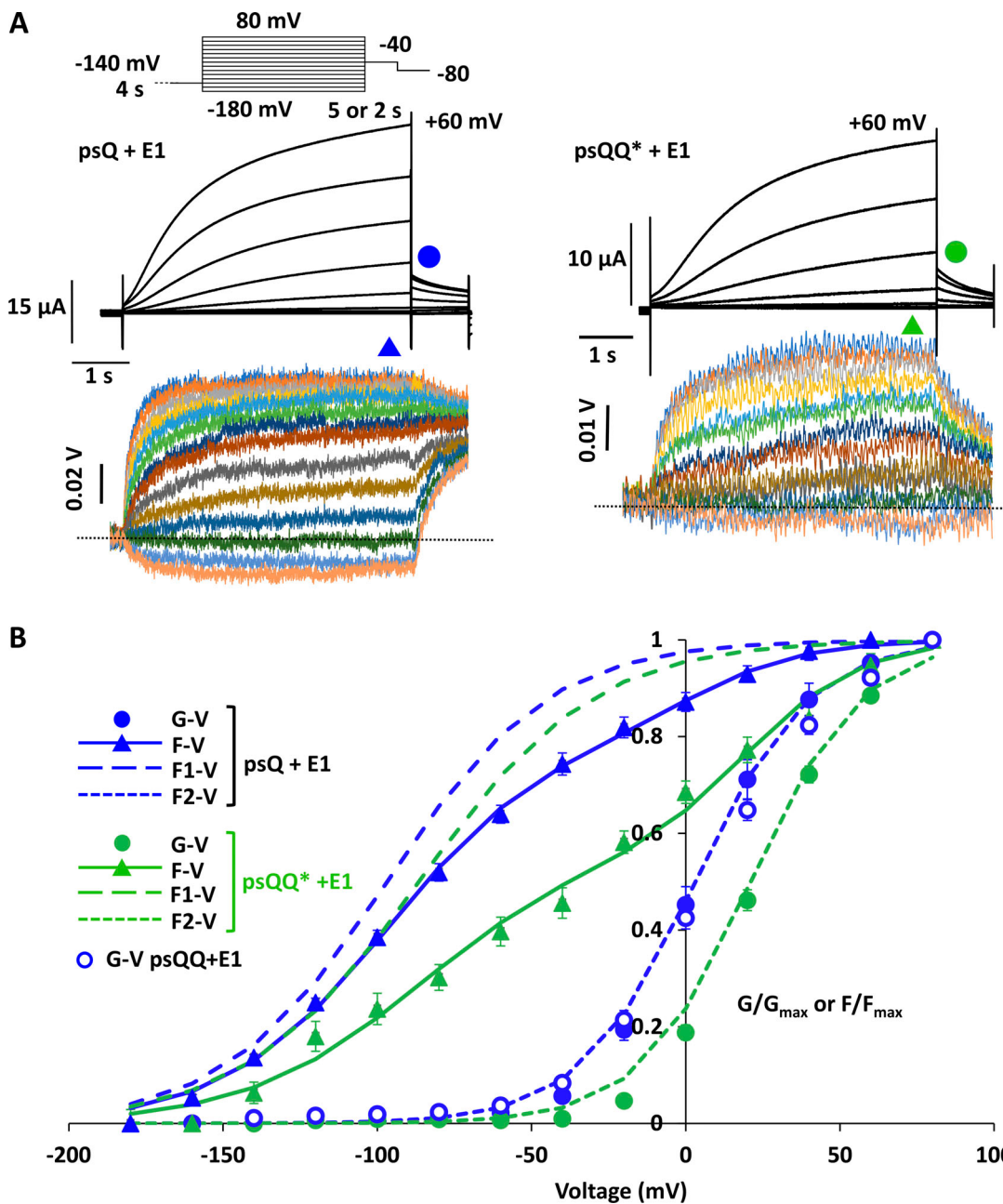


Figure 4. VCF recordings from oocyte psQ+E1 and psQQ*+E1 mutant I_{Ks} . (A) Protocol: a 4-s prepulse to -140 mV is followed by 5-s duration 20 mV steps from -180 to +80 mV. Repolarization is for 1 s to -40 and then -80 mV. Example psQ+E1 and psQQ*+E1 currents to +60 mV and fluorescence to +80 mV (below) during 20 mV steps are shown. Fluorescence traces have been subtracted from -140 mV trace to correct for photobleaching and filtered at 50 Hz for presentation. psQ+E1 traces are unaveraged, and psQQ*+E1 data are averaged from four files from a single oocyte. (B) G-V, F-V, F1-V, and F2-V plots fit with either a single (G-V) or double (F-V) Boltzmann equation. psQ+E1 (blue symbols and lines; G-V, circles $n = 14$, $V_{1/2} = 4.2$ mV; F-V, triangles $n = 8$, and fit line; F1-V, $V_{1/2} = -96.9$ mV and F2-V, $V_{1/2} = 3.0$ mV), and psQQ*+E1 (green symbols and lines; G-V, circles $n = 13$, $V_{1/2} = 23.5$ mV; F-V, triangles and fit line $n = 8$; F1-V, $V_{1/2} = -86.5$ mV and F2-V, $V_{1/2} = 21.0$ mV). The G-V for psQQ+E1 is shown as open blue circles, $V_{1/2} = 7.06$ mV, $n = 10$.

Downloaded from http://jgpress.org/jgp/article-pdf/156/3/e202313465/1923608.pdf by guest on 22 May 2023

exponential activation as the **Scheme 2** models as the rate-limiting opening step remains the same (Fig. 7 A). However, the predicted Δt values are much closer to experimental values due to the multiple extra closed steps that have to be traversed in **Scheme 3** models before channels can open. Activation time constants from the simulated data (not shown) again converge at very positive potentials as did the **Scheme 1** model curves, which is not what was observed experimentally (Fig. 3 B). **Scheme 3**

models did not produce good simulations of the 5-s experimental F-V and G-V data despite the use of the δ , γ rates measured from the fluorescence emissions. The normalized F-V relation was displaced below the experimental points (blue curves below triangles in Fig. 7 B) and although the F2-V overlays the experimental G-V, the model G-V data points are displaced to more positive voltages. The simulations of 5 s F-V data for the **Scheme 3 B** model using rate constants from the psQQ*+E1 data are quite

good if we assume equivalent fluorescence for the F1 and F2 transitions (β :1, solid green line over the triangles in Fig. 7 B). Still, the model G-V data points are significantly depolarized compared with the experimental G-V data. In this case, the modeled F2-V also overlays the experimental G-V relationship.

The inclusion of a second transition in the activation path of each VS (via the δ , γ rates) in Scheme 3 models, separate from the final concerted opening transition involving all activated VSs, did slow current activation kinetics and improve the activation delay properties, but separated the F2-V from the G-V in both models, which was a significant failure. Unsurprisingly, the use of the same experimental rate constants in both Scheme 3, A and B, models gave identical F-V relationships and the expansion of the 6-state two VS model to the 15-state four VS model failed to predict the hyperpolarization of the psQ+E1 G-V compared with that from psQQ^{*}+E1. There is no simple way, in sequential activation models that maintain independent subunit movement, to account for the G-V hyperpolarization seen experimentally as the number of activatable VSs is increased from one or two to four in both mammalian and oocyte expression systems (Fig. 1 B and Fig. 4 B).

Limiting slope behavior of pseudo-wt I_{Ks} , psQQ+E1

Ion channels that open with a concerted transition, after activation of independently moving VSs, such as Shaker and hERG, reach a limiting slope of e-fold per RT/F increase in Po at very negative voltages from which the equivalent gating charge can be estimated (Schoppa et al., 1992). The equivalent gating charge of ion channels which gate in an allosteric manner with parallel VS gating pathways through closed and open states cannot be estimated using the limiting slope method (Horrigan et al., 1999). At very negative voltages and low Po where the equivalent charge is usually estimated, the Po is higher due to channels opening from multiple closed states along the activation pathway. In allosteric gating models, a weakly voltage-dependent channel opening pathway is introduced between resting closed states and open states as well as between closed and additional open states that are accessible in a voltage-dependent manner to produce the voltage-dependence of activation seen at more positive voltages. Given these different limiting slope behaviors of ion channels that gate in a sequential or allosteric manner, the Po-V plot of I_{Ks} may reveal clues about its mechanism of gating.

For comparative purposes, this experiment was performed on hERG channels, psQ+E1, psQQ+E1, and psQQ^{*}+E1, expressed in oocytes in separate experiments. To enable measurement of very low Po values from small hERG tail currents, records were made in 20 mM [K⁺]_o, which increases single channel conductance (Materials and methods and Fig. 8) following protocols adapted from a prior study (Zhang et al., 2004). Experimental Po values were obtained from tail currents (shown enlarged) after 2 mV steps to between -72 and -40 mV, and from a second set of data obtained after 20 mV steps from -40 to +40 mV (right panel). Data from the two protocols were combined and normalized to draw an overall Po-V curve. Consistent with previous findings, at very negative voltages, a limiting Po slope was reached for hERG currents, with no deviation at the lowest Po values recorded (Fig. 8 C), which gave an equivalent number of

gating charges, z_a of $6.08 \pm 0.34 e_0$, in keeping with prior measurements from wt and mutant hERG channels. The limiting slope behavior of psQQ+E1 at negative voltages is very different from that of hERG, with the slope weakly voltage-dependent in both individual data sets and also mean data (Fig. 8, B and C). The maximum slope is achieved down to Po values of ~0.01 after which the slope decreases again at more negative voltages. The mean z_a value for psQQ+E1 measured during the steepest part of the Po-V relationship was $2.07 \pm 0.06 e_0$, for psQQ^{*}+E1 it was $2.46 \pm 0.12 e_0$, and for psQ+E1 was $2.41 \pm 0.13 e_0$ ($n = 10$, not plotted in Fig. 8 C). Neither the sequential activation Scheme 2 A (model used in Fig. 6) nor Scheme 3 A reproduce this slope decrease at more negative voltages for psQQ+E1 where the experimental Po remains higher than predicted from a sequential activation pathway (Fig. 8 D). The fit is actually reasonable down to Po ~0.01, and for psQQ^{*}+E1, there is less deviation from a sequential model. The data and fits suggest that I_{Ks} has access to open states at low Po and supports the idea of independent VS activation regulating I_{Ks} pore conductance in an allosteric manner. Moreover, adopting an allosteric model of gating might give insight into the hyperpolarizing shift of the four versus two active VS G-Vs (Figs. 1 and 4), which was not successfully reproduced by sequential gating schemes (Figs. 1, 6, and 7).

Simulations of oocyte VCF experimental results with allosteric models

An allosteric model in which independent VSs undergo a single transition from resting to activated and channel opening occurs when zero to four subunits are activated was examined first and is shown in Scheme 4. For both the 10-state model representing psQ+E1 (Scheme 4 A), the 6-state model representing psQQ^{*}+E1 (Scheme 4 B) and the 4-state model representing EQ^{*}QQ^{*}Q^{*}+E1 expressed in tsA201 cells (Scheme 4 C), an allosteric factor, D, was introduced for the closed to open transitions and between open transitions to maintain microscopic reversibility. The allosteric factor is further increased D-fold for each subunit that is activated, predisposing the channel to pass through several closed states before opening, consistent with the delays seen in I_{Ks} activation, while the C_{RRRR}-O_{RRRR}, C_{RRRA}-O_{RRRA}, and C_{RRAA}-O_{RRAA} transitions remain accessible, consistent with the higher-than-expected Po at very negative voltages (Fig. 8).

In Scheme 4 models, as $\alpha \gg \delta$ (Fig. 5), if D is sufficiently large, channel openings will be biased to occur after all VSs are activated (C_{AAAA}-O_{AAAA}), which makes the C_{RRRR}-O_{RRRR} and other C-O_{RRRA}, -O_{RRAA}, and -O_{RAAA} open state transitions negligible and transforms the parallel allosteric model into a quasi-sequential or an obligatory-coupled one (Chowdhury and Chanda, 2012b). A limiting slope would then be reached at negative voltages and the activation path would be equivalent to that of Scheme 2 models (Fig. 6). As the slope of the experimental psQQ+E1 G-V relationship becomes weakly voltage-dependent for Po less-than ~0.01 (Fig. 8 C), significant channel opening must occur from early closed states, and indeed, simulations of the Po-V relationship support the idea that D is small (Fig. 10 D).

The feature that sets allosteric models apart from sequential models with different numbers of active subunits is that in those

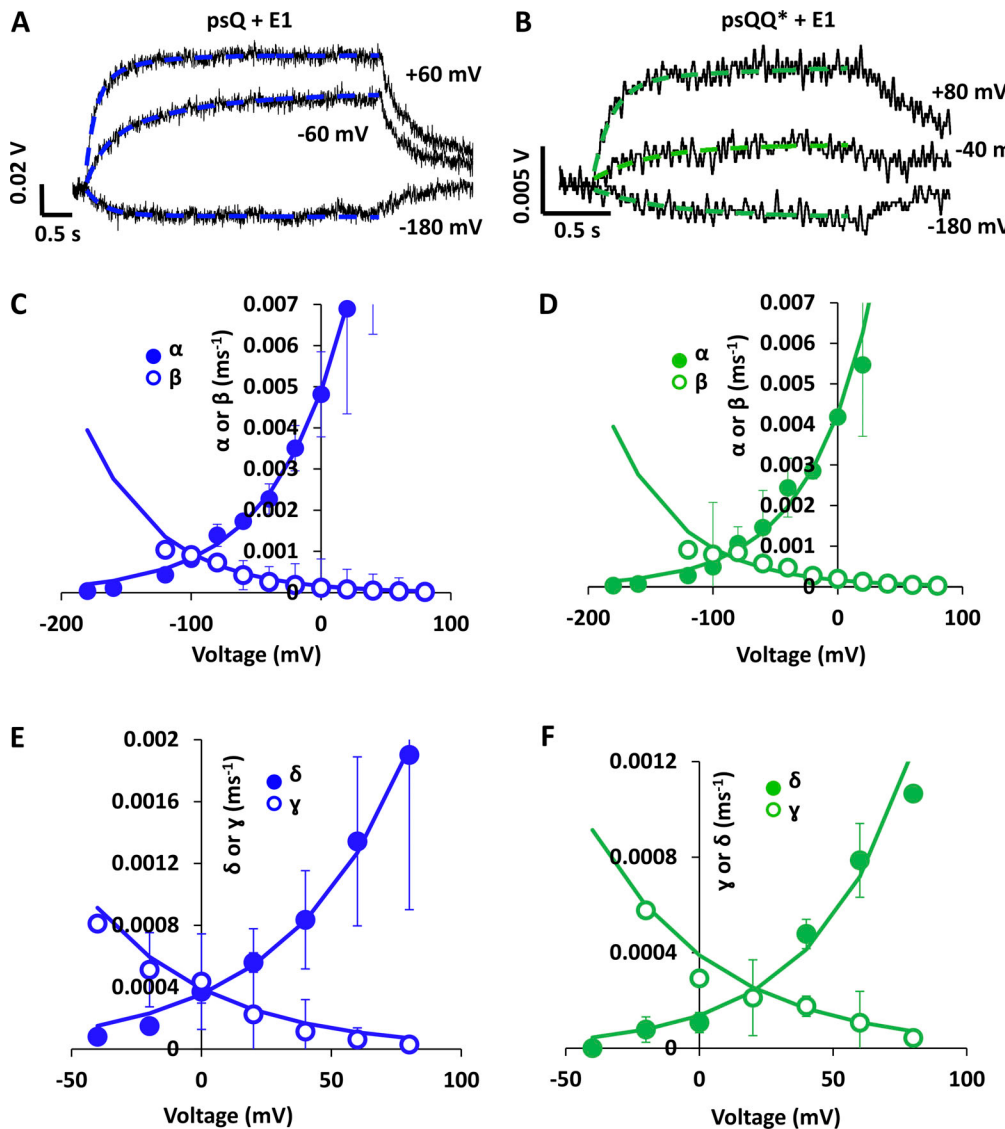


Figure 5. Fluorescence activation rate constants for psQ+E1 and psQQ*+E1 expressed in oocytes. (A and B) Representative fluorescence recordings for psQ+E1 and psQQ*+E1. Holding potential was -140 mV and pulses were to potentials indicated for 5 s or 2 s. Tracings were fit with either a single (<0 mV) or double (>0 mV) exponential (dashed lines) to obtain fluorescence activation time constants. Protocol as in Fig. 4 A. For psQ+E1, time constants were at $+60$ (164 and 683 ms), -60 (698 ms), and -180 mV (340 ms). For psQQ*+E1, time constants were at $+80$ (145 and 2,214 ms), -40 (438 ms), and -180 mV (557 ms). (C–F) For psQ+E1 (blue) and psQQ*+E1 (green), time constants and F-V values from Fig. 4 B were used to construct α - and β -V and δ - and γ -V plots (see Materials and methods). Plots were fit with Eq. 1 and rate constants are shown in Table 2. Data are shown as mean \pm SEM, $n = 3$ – 4 . Note different ordinate scales in E and F.

Downloaded from http://jgpress.org/jgp/article-pdf/115/6/3/e202313465.pdf by guest on 22 May 2025

models the rate of the opening transition reduces to δ_V at very positive voltages, whereas in the allosteric models, the rate is determined by $\delta_V D^a$, where a is the number of activated VS subunits. We suggest that this explains the lack of convergence of the $\tau_{\text{act}}\text{-}V$ relationship (Fig. 3 B) where EQ*QQ*Q*+E1 activation time constants remain persistently slower than wt Q1+E1 or EQ*Q+E1 channels with a rather stable ratio (Fig. 3 B, inset), although the theoretical Scheme 1 curves converge. These data give us a unique opportunity to calculate D from the ratios of the activation time constants for the different constructs. If the time constant ratio for wt/EQ*QQ*Q*+E1 is 0.4, which is $\delta_V D / \delta_V D^4$, then $D = 1.357$, and if the ratio for wt/EQ*Q+E1 is 0.6 (Fig. 3 B, inset), which is $\delta_V D / \delta_V D^2$, then $D = 1.291$.

A value for D of 1.357 was selected as the initial condition based on the experimental activation rates and this was combined with the experimentally derived kinetic parameters from psQQ+E1 (Table 2) and incorporated into a 10-state allosteric model for optimization (Scheme 4 A), with the conductance of early open states set to the same value as that for O_{AAAAA}. The relatively small allosteric factor of 1.357 suggests that the C_{RRRR}–O_{RRRR} transition and other early closed-open transitions will be significant at voltages around the resting potential, consistent with the idea of multiple open states accessible when zero to four VSs are fully activated (Westhoff et al., 2019). The same rate constants and allosteric factors were incorporated into the psQQ*+E1 6-state allosteric model (Scheme 4 B) and the

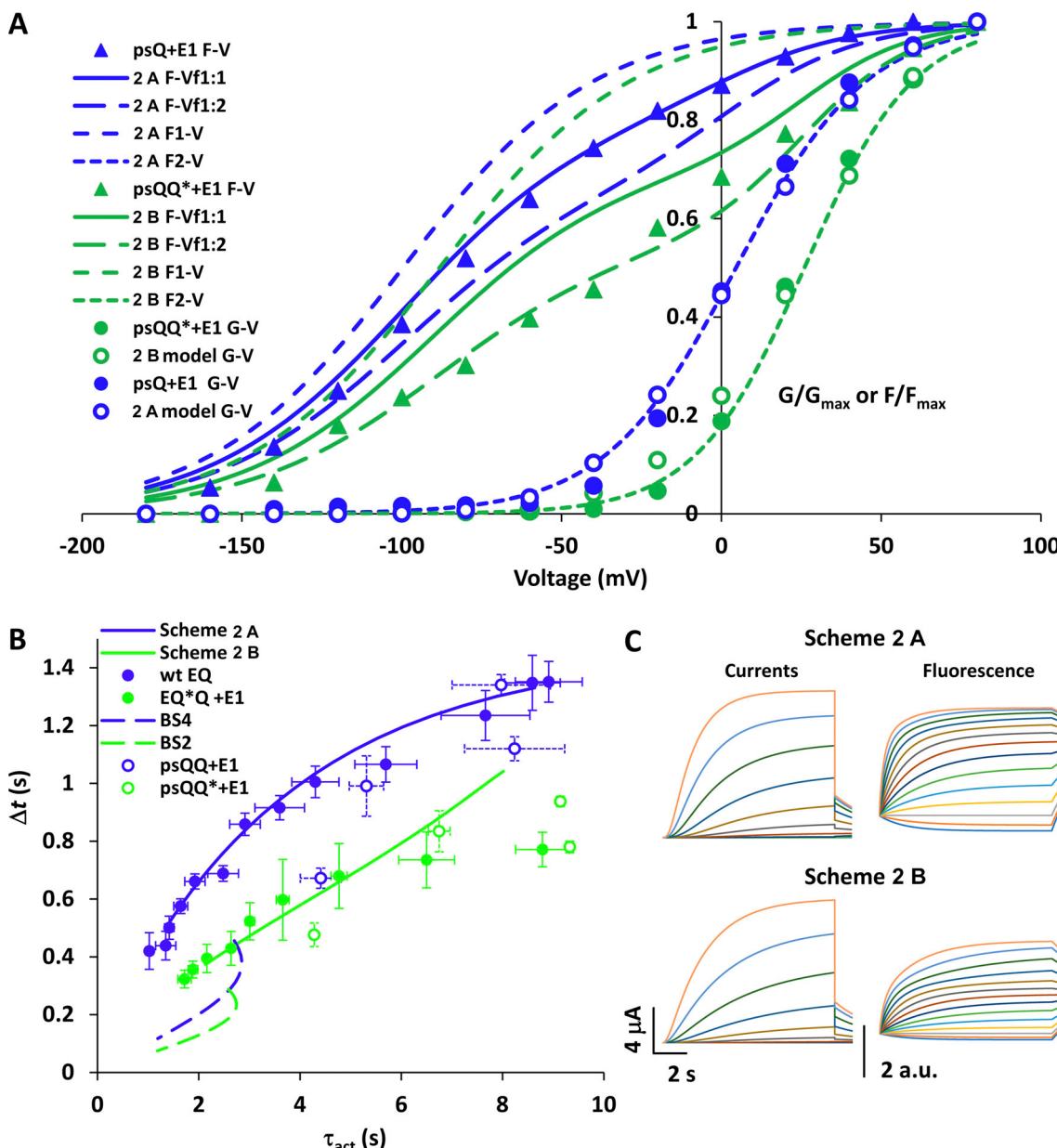


Figure 6. **Scheme 2** model simulations derived from psQ+E1 and psQQ*+E1 oocyte experiments. **(A)** F-V and G-V model data for **Scheme 2 A** (blue) and **Scheme 2 B** (green). Experimental F-V and G-V data are shown as symbols (see inset legend). Two overall F-Vs are modeled for each scheme, shown by the solid and long dashed lines. The relative value (either 1 or 2) for the fluorescence emission (f) of an α transition versus a δ transition is given in the legend for the F-Vs as f_{α}/f_{δ} . The F1-V and F2-V relations were generated from double Boltzmann fits to the modeled **Scheme 2 A** F-Vf1:1 and **Scheme 2 B** F-Vf1:2 relationships. For Boltzmann fits, see Table 1. **(B)** Δt plotted against τ_{act} . tsA201 mean wt EQ (blue) and EQ*Q+E1 (green) data (from Fig. 3 D) are shown as filled circles, mean \pm SEM, oocyte data are open circles, and **Scheme 2 A** and **B**, optimized model results as lines. Fits were after 1 s of 10 s pulses from -20 to +80 mV. Dashed lines use Barro-Soria et al. (2014) rate constants in the **Scheme 2 A** (BS4) or **Scheme 2 B** (BS2) models. **(C)** Simulated currents (left) and fluorescence (right) for psQQ+E1 (**Scheme 2 A**) and psQQ*+E1 (**Scheme 2 B**) during 10 s pulses from -140 mV to between -180 and +80 mV in 20 mV steps, with 1-s tails to -40 mV.

Downloaded from http://jgpress.org/jgp/article-pdf/156/3/e202313465/1923608/jgp-202313465.pdf by guest on 22 May 2023

EQ*QQ*Q*+E1 (**Scheme 4 C**) four-state model to examine the currents, fluorescence tracings, and model G-V relationships for comparison with experimental data (Fig. 9, A and B). The models predict the depolarizing shift of the G-V with fewer active VSs, and with D set to 1.357 are in quantitative agreement with the experimental $V_{1/2}$ values (Fig. 9, B and C; and Table 1). The slopes of the model G-Vs also decrease as the number of active VSs are reduced from 21.4 to 23.3 mV, as did the experimental G-V relationships (Fig. 1).

These model parameters also fit the equilibrium experimental oocyte current and fluorescence data (Fig. 4). Using the single set of rate constants from Table 2 (row 9), the 10-state **Scheme 4 A** and 6-state **Scheme 4 B** models fit both the F-V and G-V relationships from the psQ+E1 and psQQ*+E1 constructs very well (Fig. 9 D), predicting the shape of the F-V relationships and the voltage dependence of the F1-V and F2-V components as well as the G-Vs, plus the G-V shift to more positive potentials in psQQ*+E1 (Table 1). Only the foot of the model G-V relationship

for psQQ^{*}+E1 between -40 and 0 mV is not so well fit to the experimental data. The model appears to better simulate the mammalian data with only a minor divergence of the G-V data between -50 and -10 mV and a reduction in slope for the EQ^{*}Q+E1 model G-V (Fig. 1 B), rather than the depolarizing shift of the relationship seen in oocytes.

The Scheme 4 τ_{act} -V relations reproduce the experimental current relaxation time constants well (Fig. 10 A), and as predicted earlier, the model relationships fail to converge at up to +300 mV, the most positive voltages examined, which supports the idea of allosteric activation when more VSs contribute to the activation process. The curves also crossed over negative to -25 mV so that wt (Scheme 4 A) models support slower deactivation of currents than for constructs containing fewer active VSs, as was observed experimentally (Fig. 1 A and Fig. 3 B; Westhoff et al., 2019). The one property not well reproduced by these simulations was the activation delay, Δt . Even though the model exponential activation time constants correlated well with experimental data, the Δt values were too short when all open-state conductance levels were set to 1.0 (Fig. 10, B and C). The other extreme was therefore tested with all conductance levels set to zero except the fully activated open state (O_{AAAA}). In this situation, not surprisingly, the activation delays were increased significantly and matched the experimental data at potentials close to the activation $V_{1/2}$ (Fig. 10 C).

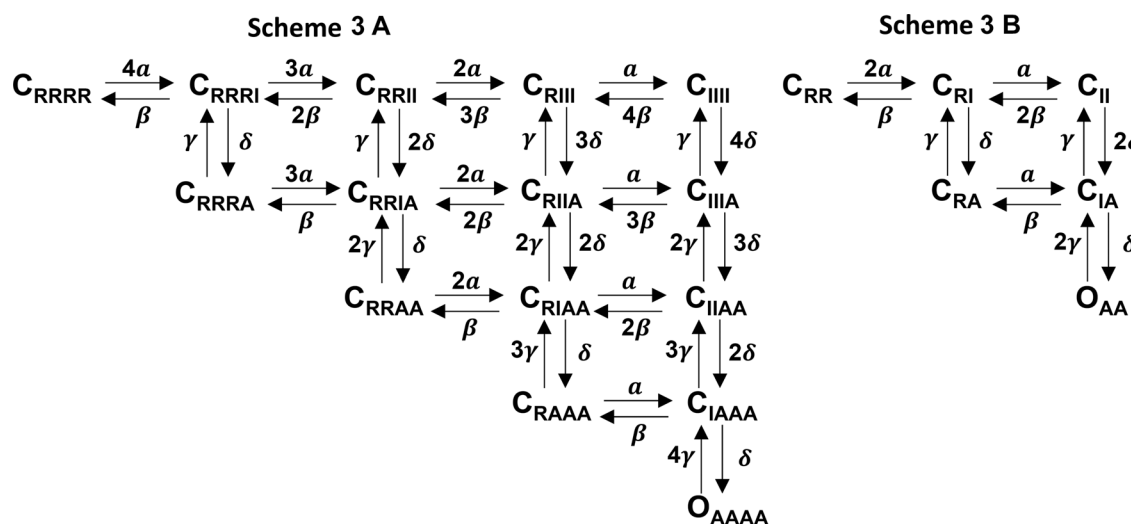
The most significant improvement that the implementation of an allosteric model with one transition per VS makes when fitting the experimental steady-state data is that the depolarization of the EQ^{*}QQ^{*}Q^{*}+E1, and psQQ^{*}+E1 G-V relationships, and the displacement of the F2 component of the F-V relative to the wt EQ and G219C psQ+E1 data are now faithfully reproduced in the models using a single set of rate constants (Fig. 9 and Table 2). The correct voltage dependence and amplitude of current relaxation time constants, and speeding of deactivation in EQ^{*}Q+E1 and EQ^{*}QQ^{*}Q^{*}+E1 compared with wt is also seen

(Fig. 10). At more negative potentials, the use of the allosteric Scheme 4 model could reduce the slope of the Po-V relationship at Po values <0.01, and adjustments to the allosteric factor changed the shape of the model Po-V between -50 and -100 mV. Overall, the experimental D value of 1.357 most accurately predicted the limiting slope behavior of psQQ+E1 at very low Po values, as shown by the overlay with the averaged experimental data (Fig. 10 D).

Allosteric models with two transitions per VS

Having established that allosteric models are able to make significant improvements to the modeling of I_{Ks} activation, we proceeded to include a second VS step (Figs. 11, 12, and 13) to be consistent with our appreciation of experimental data, demonstrating that VSs undergo at least two transitions during the activation process along with the channel opening step (Barro-Soria et al., 2014; Zayzman et al., 2014). In these Scheme 5 models, though, unlike in prior published work (Zayzman et al., 2014; Westhoff et al., 2019), we coupled the δ , γ rates derived from F2 measurements to the opening transitions and generated a new set of rate constants, “ κ ” and “ λ ,” to simulate a slow VS transition from intermediate-activated to fully activated states (Fig. 11). The reasons for this are first, that experimental studies have closely linked the F2 measurement with channel opening, even in the presence of mutations and drugs that change its voltage dependence (Osteen et al., 2010; Zayzman et al., 2014; Barro-Soria et al., 2014; Westhoff et al., 2019). Second, no gating currents have been shown to be associated with this second VS movement (Ruscic et al., 2013), and third, that recent cryo-electron microscopy data support a reorientation of the top of S4 which could certainly affect the environment of a fluorophore attached at G219C when PIP₂ binds to the channel and it opens (Mandala and MacKinnon, 2023).

Scheme 5 models (Fig. 11) depict tiered allosteric schemes wherein the VSs undergo two transitions during the activation



Scheme 3. Sequential models for psQ+E1 (Scheme 3 A) and for psQQ^{*}+E1 (Scheme 3 B) incorporating two VS transitions and a single concerted opening step. Channel states are represented as closed (C) and open (O). For each VS, subscript R denotes those in the rest state, I refers to those in the intermediate activated state, and A denotes those in the activated state.

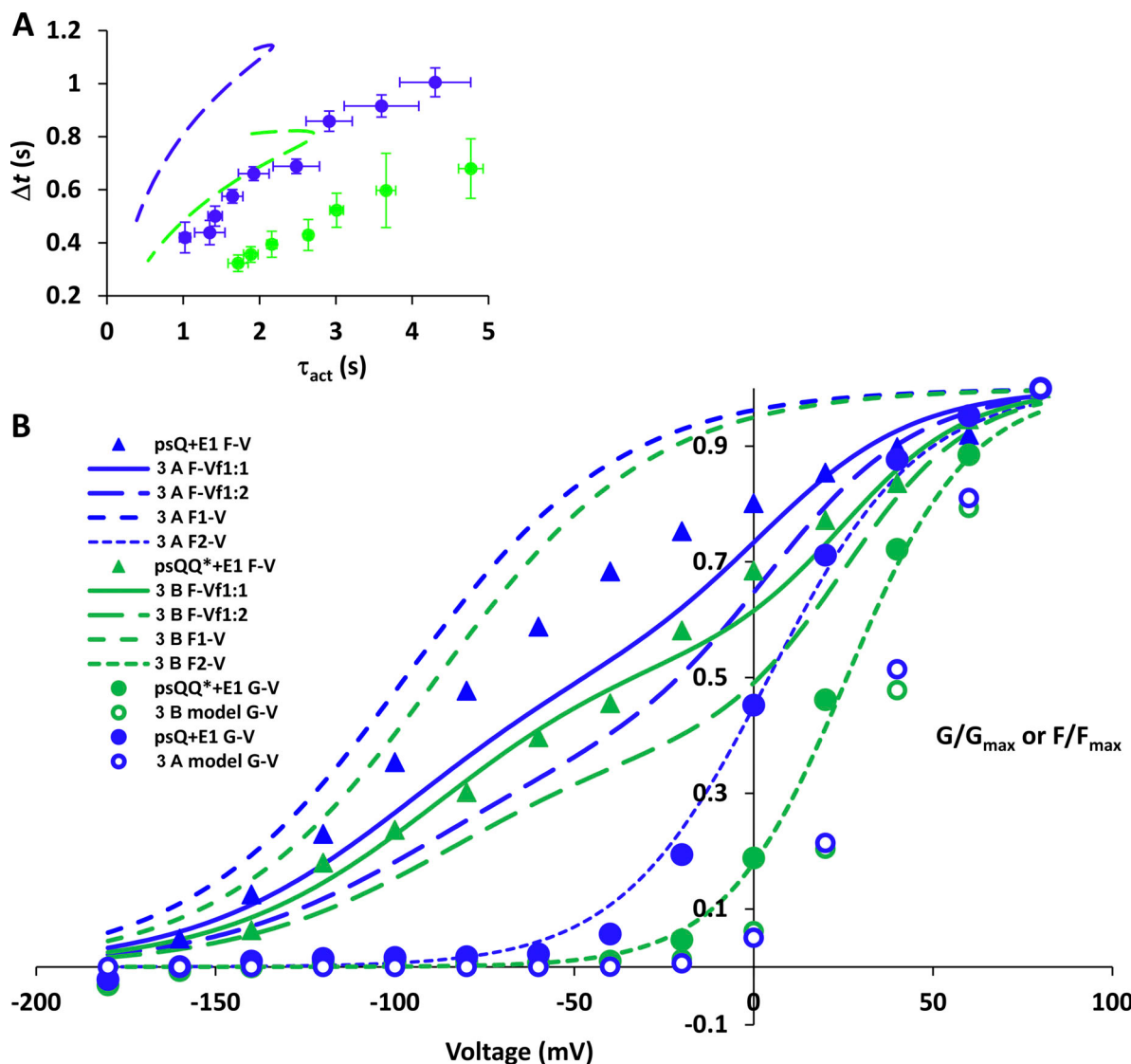


Figure 7. Scheme 3 models derived from psQ+E1 and psQQ*+E1 oocyte VCF data. (A) Δt - τ_{act} relations for Scheme 3 A (blue) and 3 B (green) models (dashed lines). Experimental tsA201 data for wt EQ (blue) and EQ*Q+E1 (green) are shown as mean values \pm SEM, from Fig. 3 D. Fits to obtain model τ_{act} values started after 1 s of 10-s pulses from -20 to +80 mV. (B) F-V and G-V model data for Scheme 3 A (blue) and 3 B (green). Experimental F-V and G-V data are filled symbols (see inset legend). Two overall F-Vs are modeled for each scheme, shown by the solid and long dashed lines. The relative value (either 1 or 2) for the fluorescence emission (f) of an α transition versus a δ transition is given in the legend for the F-Vs as f_α/δ . The F1-V and F2-V relations were generated from double Boltzmann fits to the modeled Scheme 3 A F-Vf1:1 and the Scheme 3 B F-Vf1:1 relationships.

Downloaded from http://jgpress.org/jgp/article-pdf/156/3/e202313465/19236081.pdf by guest on 22 May 2023

process before being able to open. Two sets of voltage-dependent rates, α , β and κ , λ , determine the VS transitions from resting to intermediate ($R \rightarrow I$) and intermediate to activated ($I \rightarrow A$) states. Rate constants δ and γ regulate opening and closing along with the allosteric factor, D , to determine the channel transitions from closed to open states, and similar to Scheme 4, A-C, opening allostery increases D -fold for each activated available VS. (D set to 1.357 for these simulations). Experimentally derived G-V and F-V kinetic parameters from psQ+E1 (Fig. 4), and Δt versus τ_{act} data from wt EQ (Fig. 3) were incorporated into Scheme 5 A for optimization in MATLAB (see Materials and methods) to obtain a single set of rates used in Scheme 5, A-C, models. The optimized simulations for current and fluorescence tracings and equilibrium relationships are shown in Fig. 12, with

summarized model kinetics in Table 1 and optimized transition rates in Table 2 (row 10). The time course and exponential activation of experimental currents are accurately simulated by Scheme 5 A using the optimized transition rates (Fig. 12 A). Simulations of Scheme 5 A currents and the underlying occupancy of channel open states at 0 and +80 mV show that the activation delay and slow exponential relaxation of currents is accounted for by the slow movement of channels through connected open states, especially at 0 mV, by the large numbers of channels retained in closed states in Scheme 5 models (Fig. S5). As was the case for Scheme 4 models, the oocyte G-V and F-V curves are also reproduced by Scheme 5, A and B, models. The F2-Vs are not so closely aligned at the foot with the G-Vs as in Scheme 4 models, but the depolarization of the F2-V and G-V

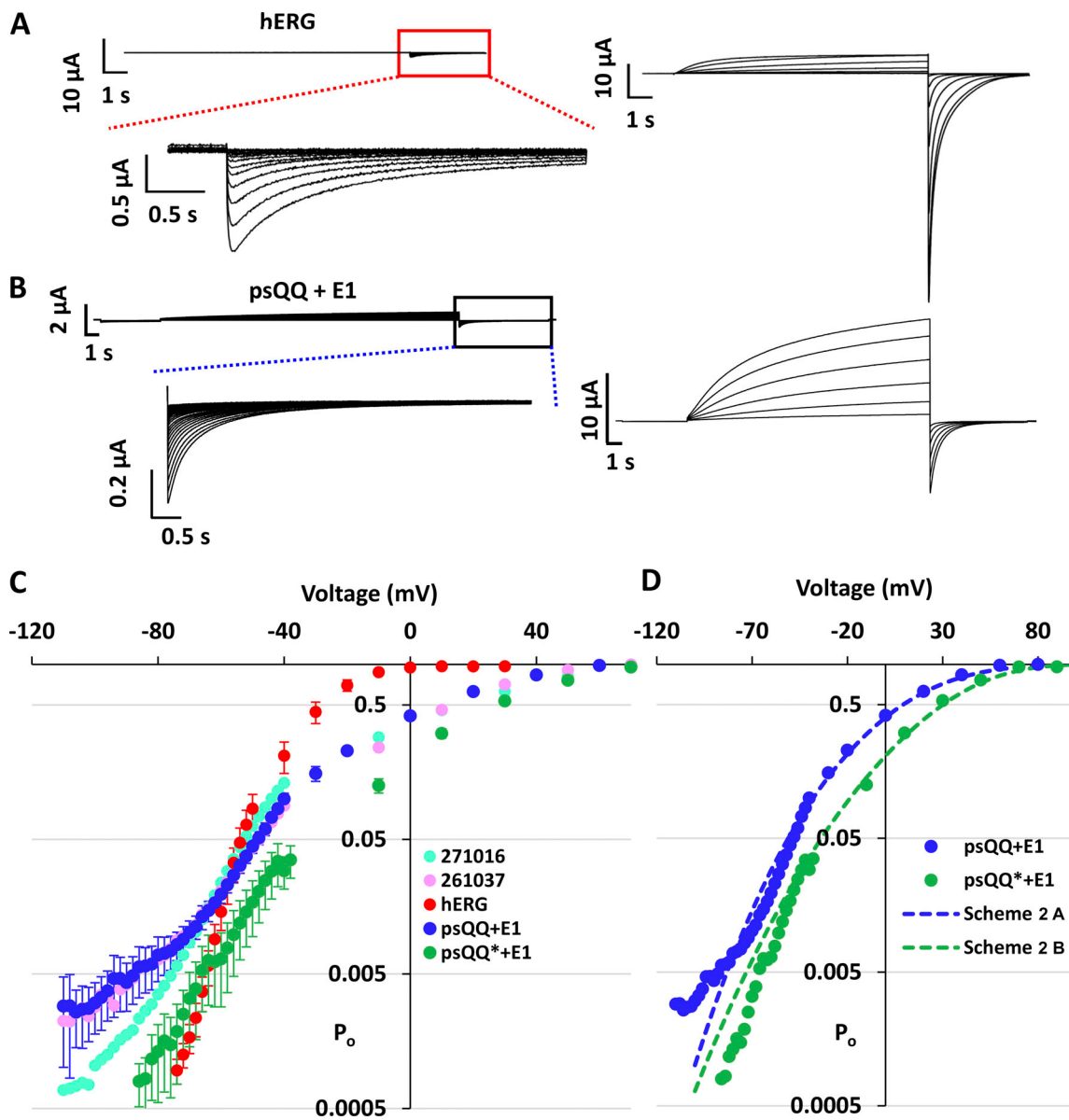
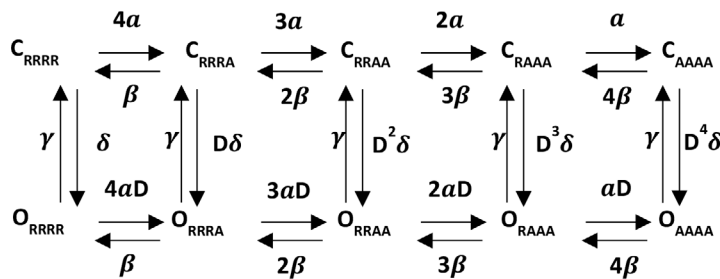
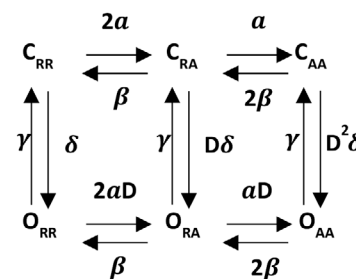
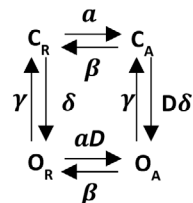


Figure 8. Limiting slope behavior in oocytes of wt-hERG and I_{Ks} constructs, psQQ+E1 and psQQ*+E1. **(A)** wt-hERG oocyte currents in 20 mM $[K]_o$, obtained using 10-s activating pulses in either 2 mV steps from -72 to -40 mV (left) or 10 mV steps from -40 to +40 mV (right) followed by a repolarization step to -90 mV for 3 or 4 s, respectively. Holding potential was -90 mV. **(B)** psQQ+E1 oocyte currents obtained by stepping to -140 mV for 4 s followed by either 20 s activating pulses in 2 mV steps from -100 to -30 mV (left) or 10 s activating pulses in 20 mV steps from -20 to +80 mV (right) followed by a repolarization step to -140 mV for 3 or 6 s, respectively. Holding potential was -90 mV. **(A and B)** Inset: Expanded views of the tail currents during the 2 mV increments. **(C)** Po-V semilog plot for wt-hERG (red, $z_a = 6.08 \pm 0.34 e_0$, $n = 4$), psQQ+E1 (blue, $z_a = 2.07 \pm 0.06 e_0$, $n = 10$), and for psQQ*+E1 (green, $z_a = 2.46 \pm 0.12 e_0$, $n = 7$). Limiting slope data for psQQ+E1, and psQQ*+E1 are adjusted by -10 mV to align with $V_{1/2}$ values of fluorescently labeled constructs. Two individual psQQ+E1 data plots are shown as pink (261037) and turquoise (271016) symbols. **(D)** Comparison of Scheme 2 A (blue) and 2 B (green) model Po-V plots (dashed lines), with psQQ+E1 (blue) and psQQ*+E1 (green) experimental data as circles.

(Fig. 12, B and C) curves in the psQQ*+E1 model versus the psQ+E1 model is reproduced, as is the overall shape of both F-V relations. The change in the G-V $V_{1/2}$ values from 7.5 to 34 mV going from wt to the EQ*QQ*Q*+E1 Scheme 5 C model are in quantitative agreement with tsA201 and oocyte data in Table 1, and are just as impressive as for Scheme 4 models (Fig. 9 C). Importantly, the current relaxation time constants (τ_{act} , Fig. 12 D) and activation delays (Δt , Fig. 12 E) are also very well simulated by Scheme 5 A models using a single set of rate

constants (Table 2). At very positive voltages, the τ_{act} -V relationships maintain their separation between the three Scheme 5 models (Fig. 12 D). This is the first model system that we have investigated that has proven adept at simulations of both isochronal and transient I_{Ks} kinetics across all three constructs using a single set of kinetic constants.

Although the experimental G-V and F-V equilibrium kinetics and the separation of the τ_{act} -V relationships from the different E160R-containing constructs are reproduced across all Scheme 5

Scheme 4 A**Scheme 4 B****Scheme 4 C**

Scheme 4. Allosteric gating models for psQ+E1 (Scheme 4 A), for psQQ*+E1 (Scheme 4 B), and for EQ*QQ*Q*+E1 (Scheme 4 C). Positive allosteric coupling of VS activation to pore opening is via the allosteric factor, D. Channel states are represented as closed (C) and open (O). Subscript R denotes VS in the rest state and A denotes those in the activated state.

models using a single set of kinetic constants (Fig. 12), the measured activation delay, Δt , and τ_{act} -V was not well fit for the Scheme 5 C model (Fig. S6). Reasons for this are considered in the Discussion, but in order to simulate the transient kinetics of the tsA201 EQ*Q+E1 and EQ*QQ*Q*+E1 current activation data better, we optimized the Scheme 5, B and C, models individually, minimizing the difference between experimental and computed relationships for the τ_{act} -V and Δt -V. The results are shown in Fig. 13, and the kinetics for these models are in Table 2. The simulation of the Δt versus τ_{act} relationship (Fig. 13 A) and its component Δt -V (Fig. 13 C) and τ_{act} -V relations (Fig. 13 D) for Scheme 5, B and C, models is excellent with the new rates, which are characterized by a 3–5× acceleration of the α , β , δ , γ , rate constants and minor slowing of the κ and λ rate constants (Table 2), compared with the single set of kinetic constants used for all model plots in Fig. 12 (and Fig. S6) and the Scheme 5 A simulations of EQ experimental data in Fig. 13. There is only a slight degradation of the Scheme 5, B and C, model G-V fits to the experimental data using these separate rates (Fig. 13 B), compared with the unified set of rates (Fig. 12 C), and this is almost certainly the result of not prioritizing the experimental G-V data in the optimization process to obtain them.

Discussion

Summary of experimental effects of reduced numbers of VSs

The aim of the present study was to examine gating models that have been proposed for the I_{Ks} channel and evaluate their ability to reproduce the gating and activation properties of the channel under a number of different conditions. The new information that we were able to add in this study is built upon prior work from our laboratory, which demonstrated the functionality of

channels with less than four active subunits. The mutation E160R in individual subunits allowed novel insights to be obtained from the comparison of channel currents, activation properties, and fluorescence in situations where one to three VS subunits were restrained and unable to contribute to the gating process (Westhoff et al., 2019). The ability of the E160R mutation to restrain the activation of VS was suggested by the lack of current when E160R was present in all four VS domains despite cell-surface protein expression (Zaydman et al., 2014; Westhoff et al., 2019), the lack of methanethiosulfonate reagent effects on ion current activation when labeled subunits also contained the E160R mutation, the reduction in conductance with each additional E160R, and the absence of fluorescence during channel activation from E160R-containing subunits (Westhoff et al., 2019). Further support for the ability of the E160R mutation to negate the contribution of individual VS to channel activation is provided in the present study by the non-convergence of τ_{act} data at voltages positive to +100 mV (Fig. 3), reduced activation delay in constructs with fewer active VSs, and allosteric activation models, which predict the G-V shifts and reduced slope, and F-V depolarization with fewer active VSs (Figs. 9, 10, 11, 12, and 13).

At first glance, the currents from the E160R-containing constructs, EQ*Q+E1 and EQ*QQ*Q*+E1, look not dissimilar to wt I_{Ks} , even when three VSs contain the E160R mutation, leaving only one active VS (Fig. 1 A). However, the amplitudes are less (Westhoff et al., 2019), current activation appears slower, and tail currents are faster with fewer activatable VSs (Figs. 1, 2, and 3). Upon closer examination and with further experimentation, some subtle, and not so subtle differences in the behavior of the different channel constructs become apparent. There is a decrease in the slope of the G-V relationship as the number of VSs is reduced, and a progressive shift of the $V_{1/2}$ of activation to

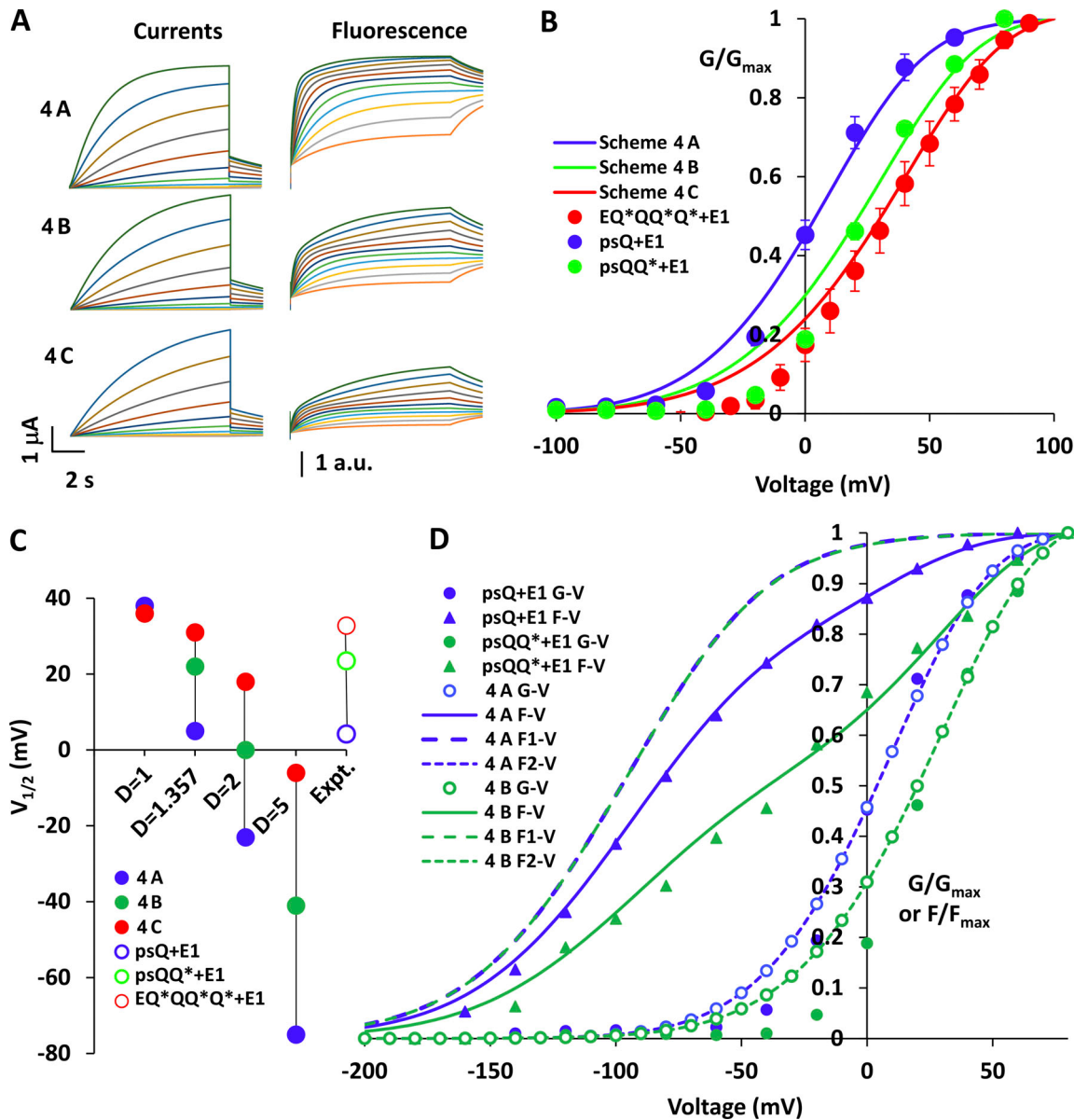


Figure 9. Scheme 4 simulations of psQ+E1 and psQQ*+E1 currents and fluorescence. (A) Currents and fluorescence from Scheme 4, A–C, allosteric models during 10 s pulses from -140 mV to between -100 and $+100$ mV in 20 mV steps, followed by 2 s pulses to -40 mV. All model tracings and plots were obtained using the protocol in Fig. 4 A with extended voltages. **(B)** G-V relationships for Scheme 4 models: 4 A, blue; 4 B, green; 4 C, red. The $V_{1/2}$ s were $+4.5$ mV ($k = 21.4$ mV), $+22$ mV ($k = 22.9$ mV), and $+31$ mV ($k = 23.3$ mV), respectively. Models were run for 10 s at each test voltage. Experimental oocyte and tsA201 data are shown as symbols (mean \pm SEM), psQ+E1 (blue), psQQ*+E1 (green), and EQ*QQ*Q*+E1 (red). **(C)** Effect of allosteric factor, D, on Scheme 4 model G-V $V_{1/2}$ s. Experimental values are hollow circles (Expt.), with $V_{1/2}$ s of 4.2, 23.5, and 32.8 mV for psQ+E1, psQQ*+E1, and EQ*QQ*Q*+E1, respectively. **(D)** Experimental psQ+E1 (blue) and psQQ*+E1 (green) G-V (filled circles) and F-V data (triangles), overlaid with model G-V (open circles) and F-V fits (lines) from Scheme 4 A (blue), and Scheme 4 B (green). F1-V and F2-V simulations are shown as long dash and short dash lines, respectively. For Boltzmann fits to G-Vs and component F-Vs, see Table 1.

more positive potentials (Fig. 1 B), which is opposite to the direction expected for Hodgkin–Huxley models of activation. The time constants for exponential relaxation of current (τ_{act}) after the activation delay accelerate at very positive potentials but do not converge in the different constructs, and the τ_{act} ratio between wt and EQ*QQ*Q*+E1 stabilizes at ~ 0.4 (Fig. 3 B). The activation delay, Δt , is reduced, but $\neq 0$ with three restrained VSs in EQ*QQ*Q*+E1 (Fig. 3 D), which indicates that even the single active VS must undergo multiple steps during activation gating.

This idea is supported by fluorescence data which divide the fluorescence emission from G219C into two exponential components (Fig. 4). The presence of fewer closed states in oocyte constructs with fewer active VSs (psQQ*+E1) is suggested by Cole–Moore type experiments (Cole and Moore, 1960), while the limiting slope experiments show a prominent deviation from linearity at $P_o \sim 0.005$ and -80 mV, in psQ+E1 and psQQ+E1 constructs, which supports the presence of multiple open states, some traversed early in the activation pathway.

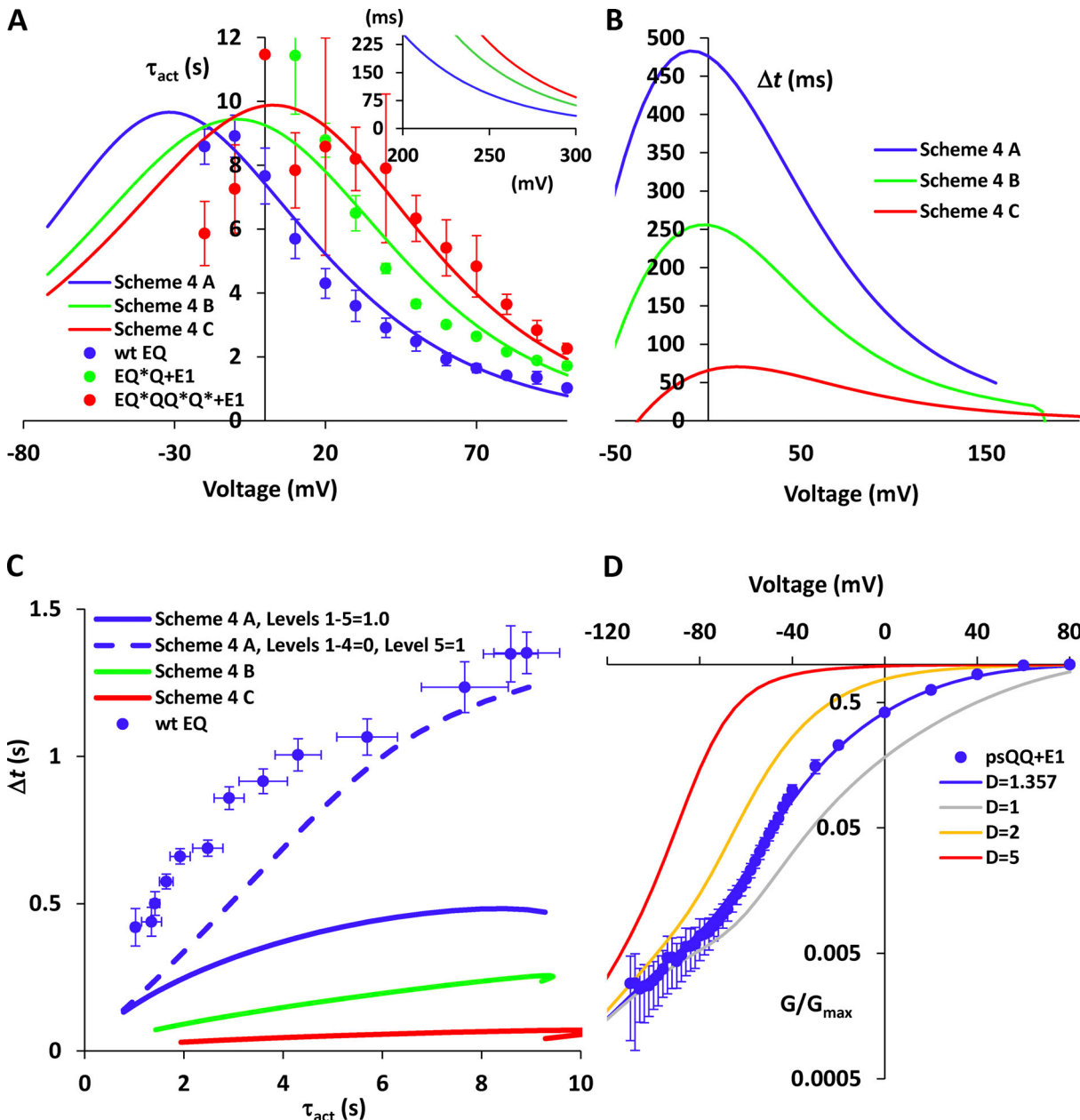


Figure 10. **Scheme 4 kinetics.** **(A)** τ_{act} -V relations for **Scheme 4, A-C**, as lines, and EQ, EQ*Q+E1, EQ*QQ*Q*+E1 experimental time constant data as circles (mean \pm SEM). Exponential relaxation of model currents fit after the first 1 s of the 10 s activation pulses from -70 to +100 mV. The inset panel shows the extended curves from +200 to +300 mV, model data fit after 50 ms, and demonstrates a lack of convergence. **(B)** Δt -V relations for voltages between -55 and +200 mV for **Scheme 4, A-C**, models. **(C)** Δt plotted against τ_{act} . Wt EQ data from Fig. 3 D are shown as mean values \pm SEM, **Scheme 4 A** model with all open state conductances equal (blue line), and with only O_{AAAA} conducting (blue dash line). Fits were after 1 s of the 10-s activation pulse from -20 to +100 mV. Green and red curves are for **Scheme 4, B and C**, models, respectively. **(D)** Mean psQQ+E1 Po-V data from -120 to 80 mV replotted from Fig. 8 (blue circles) overlain with **Scheme 4 A** fit lines. Allosteric factor, D, was adjusted while maintaining experimental rate constants and conductance levels for all open states (grey, D = 1; blue, D = 1.357; orange, D = 2; red, D = 5).

Downloaded from http://jgpress.org/jgp/article-pdf/156/3/e202313465/1923608.pdf by guest on 22 May 2023

There were some experimental limitations that were imposed by the need to use a wide range of voltages during experimental protocols and constructs with VSs containing the E160R mutations. Ideally, we preferred to use channels expressed in mammalian cells due to the higher quality of voltage clamp attainable to measure Δt and τ_{act} . But, cells were generally intolerant of being held at potentials negative to -120 mV (Fig. S2), of voltage pulse steps to greater than +100 mV, and also of

voltage pulses longer than 10 or 20 s, which would be required to obtain steady-state G-V relationships. Fluorescence measurements of VS movement could not be made in tsA201 cells due to their small size, while limiting slope measurements at low Po required expression levels at negative voltages that were also unattainable in mammalian cells. These limitations necessitated the use of a mixed set of data from mammalian cells and oocytes, which were not identical. Oocyte constructs modified for

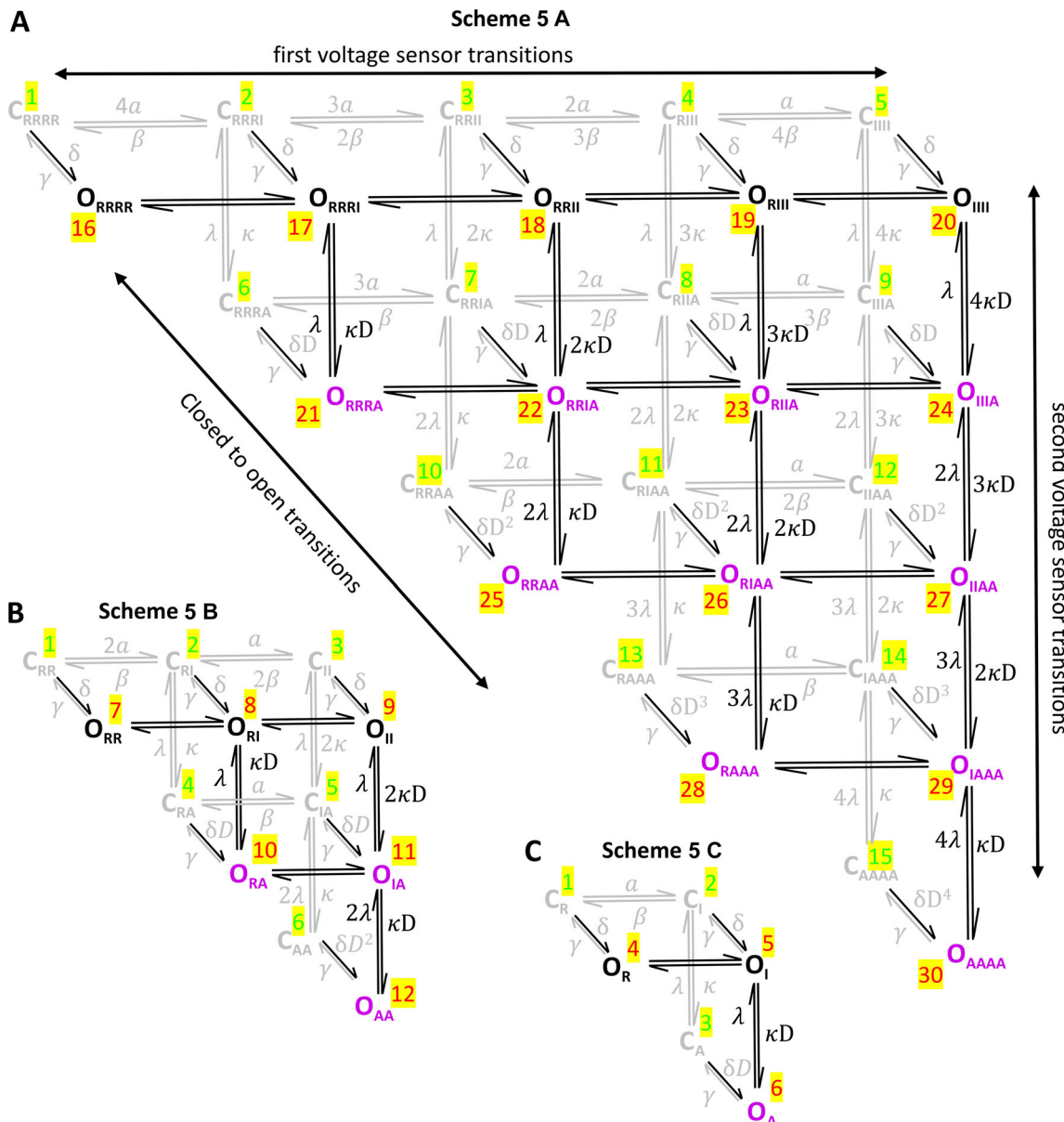


Figure 11. Scheme 5 models. Two-tier allosteric models for psQ+E1 (Scheme 5 A), for psQQ^{*}+E1 (Scheme 5 B), and for EQ^{*}QQ^{*}Q^{*}+E1 (Scheme 5 C). Closed states (C) and closed-state transitions are depicted as grey and open states (O) and transitions are black. Closed to open state transitions and their reverse are black/grey arrows. For each VS, state subscripts R denotes the rest state, I refers to the intermediate activated state, and A is the activated state of the VS. Only open states that have activated VSs are deemed to conduct current (in purple). Model transition constants and multipliers are labeled, except α and β between open states as they are identical to those between closed states. Open channel states are numbered (red) and closed states (green) with yellow highlight corresponding to their specification in the MATLAB models.

fluorescence measurements (see Materials and methods) all showed a negatively shifted G-V relationship ~ 10 mV (from +13 to +4 mV, Table 1), but psQQ^{*}+E1 still showed a positive shift of the G-V $V_{1/2}$ (from +4 to +24 mV) compared with psQ+E1 and psQQ+E1 (Fig. 4 B), similar to that seen in mammalian cells. Unfortunately, the oocytes only poorly expressed RNA constructs with multiple concatenated subunits, so fluorescence data from psQQ+E1 and psQQ^{*}+E1 were much harder to obtain, signals were smaller than from psQ+E1, and could not be obtained from constructs with three E160R VS subunits. Despite these limitations, new data were

obtained that informed the makeup of activation models, as discussed below.

Single-open-state sequential models (Scheme 1) of I_{K_s} gating
While models based on the Hodgkin and Huxley differential equations of channel activation (Hodgkin and Huxley, 1952) may seem anachronistic in a modern analysis of activation gating systems, the reality is that most models of ion channel gating will adhere to their systematization of activation, perhaps because experimental data from steady-state G-V relationships and activation time constants are still widely used to formulate

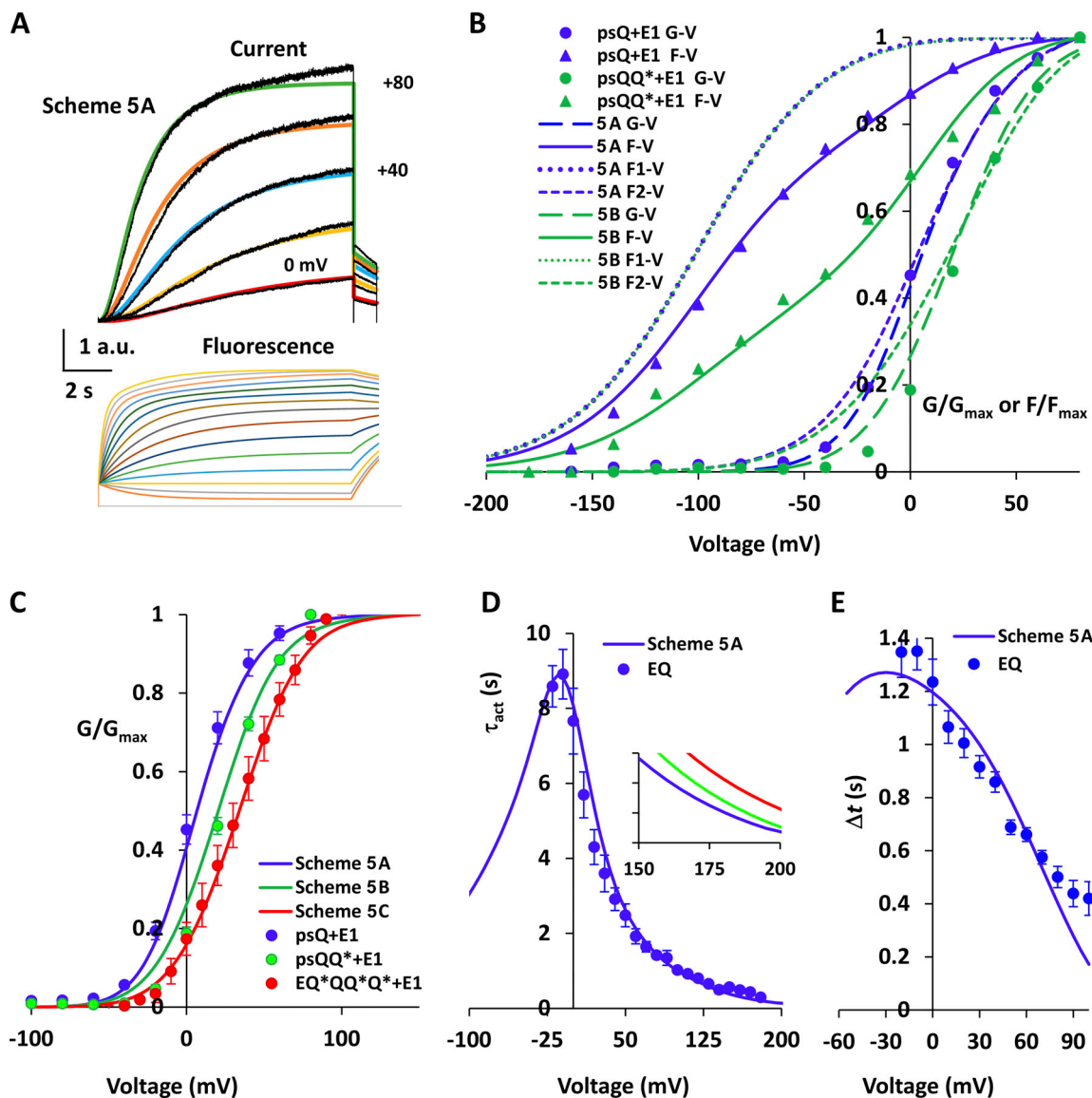


Figure 12. Scheme 5 current and fluorescence simulations. (A) EQ experimental data (black traces), 10-s pulses, overlain with normalized Scheme 5 A model currents during 10 s pulses to between 0 and +80 mV in 20 mV steps with 1 s step to -40 mV. The lower panel shows fluorescence simulations for Scheme 5 A in 20 mV steps from -140 mV to between -180 and +100 mV, followed by 2-s tail pulses to -40 mV. Model plots obtained with rates from Table 2, row 10. Grey line indicates zero fluorescence level. (B) Scheme 5 simulations as lines, psQ+E1 (blue) and psQQ*+E1 (green) overlay experimental F-V data (triangles), G-V (circles $V_{1/2} = 4.2$ and 23.5 mV, respectively). F1-V and F2-V simulations are shown as dots and short dash lines, respectively, while G-V simulations are long dash. For Boltzmann fits, see Table 1. (C) Scheme 5 model G-Vs as lines, with four (blue), two (green), or one (red) active VS. Model $V_{1/2}$: +7.5 ($k = 17.5$ mV, Scheme 5 A), +20.6 ($k = 19.3$ mV, Scheme 5 B), and +33.8 mV ($k = 20$ mV, Scheme 5 C). Experimental data as symbols. (D) τ_{act} -V relation for Scheme 5 A (blue line), model currents fit after the first 0.05–1 s of the 10 s activation pulse and EQ experimental time constant data as circles (mean \pm SEM). Inset shows Scheme 5 A (blue), 5 B (green), and 5 C (red) model time constants for voltages between +150 and +200 mV. (E) Δt -V relation for Scheme 5 A. Mean EQ tsA201 data (Fig. 3 C) between -20 and +100 mV as symbols (mean \pm SEM). Scheme 5 A model data as line. Model fits start at 1 s of the 10 s pulse from -55 to +100 mV.

Downloaded from http://jgpress.org/jgp/article-pdf/156/3/e202313465/1923608.pdf by guest on 22 May 2023

gating models. Therefore, we first examined sequential models with a single open state based on Scheme 1 to determine if they could account for I_{Ks} gating. Such models are consistent with a reduced version of Hodgkin and Huxley activation of a K^+ channel (Hille, 2001) with different numbers of VSs. In these models, the movement of the last voltage sensor directly couples with channel opening and is depicted as a single event. We used the EQ*QQ*Q*+E1 construct, which has only one activatable VS, to record time constant and isochronal G-V data and solve

exactly the rate kinetics for the single transition (Scheme 1 C), and optimize them to fit a model to the data. This model was then extended to Scheme 1, B and A, to fit data from EQ*Q+E1 and wt, respectively (Figs. 1, 2, and 3; Figs. S1, S2, and S3; and Tables 1 and 2). The Scheme 1 C model optimized fits reproduce the isochronal G-V and τ_{act} kinetics of EQ*QQ*Q*+E1 well, including the overall current recordings at different potentials (Fig. 1 and Fig. 2 C), but cannot simulate the delay in activation (Δt) and the rate constants do not transfer well to the schemes with more active subunits.

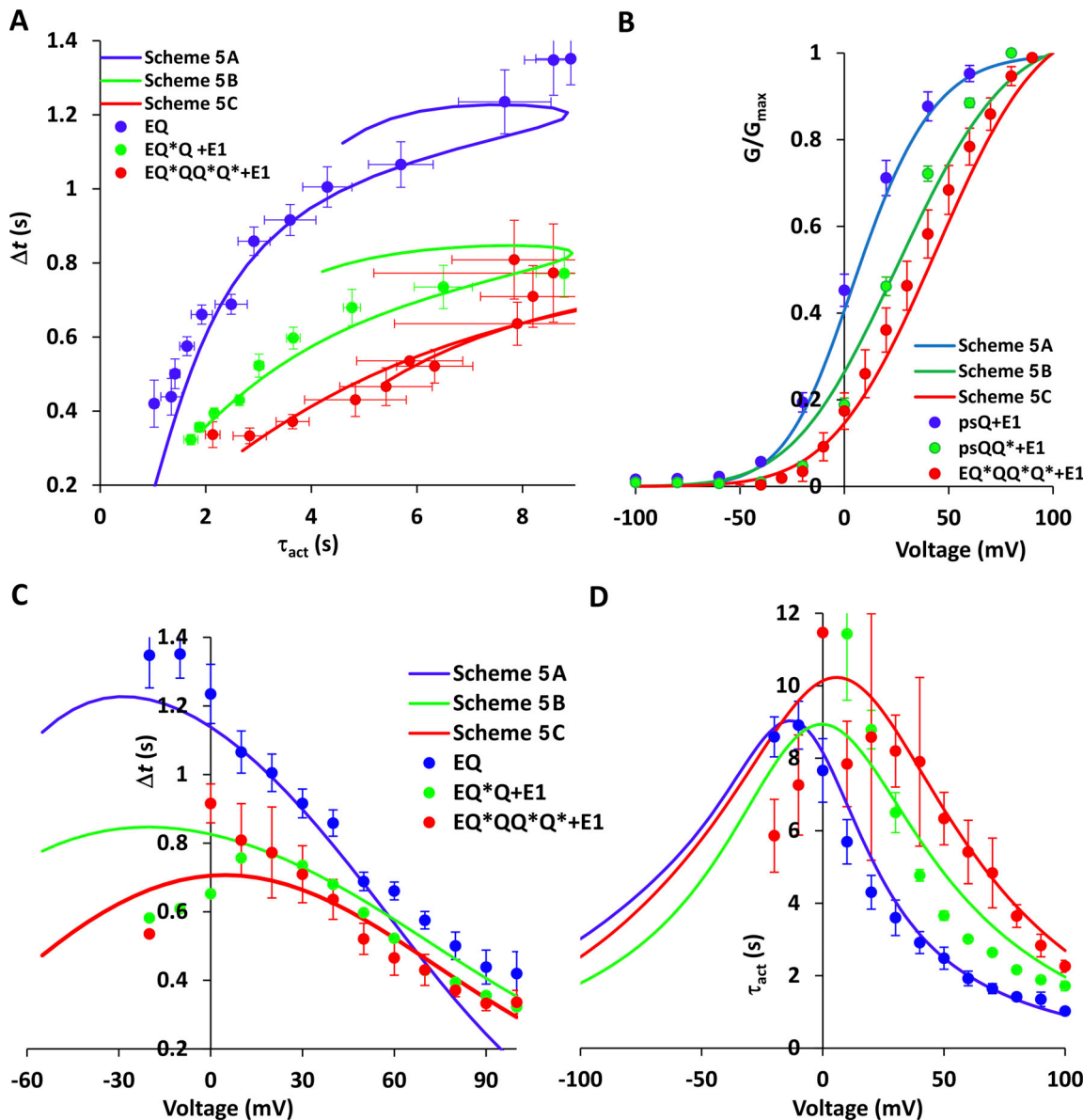


Figure 13. Current activation delay and time constant optimization for Scheme 5, B and C, models. **(A)** Δt versus τ_{act} . Mean tsA201 data for EQ, EQ^*Q+E1 , and $EQ^*QQ^*Q^*+E1$ (Fig. 3 D) as symbols (mean \pm SEM), currents fit between -20 and $+100$ mV. Scheme 5 models are shown as lines and were fit to simulated currents starting at 1 s of the 10 s pulse from -55 to $+100$ mV. Transition constants for 5 B and 5 C models are in Table 2, lines 11 and 12. All Scheme 5 A model data use the same kinetic constants as in Fig. 12. **(B)** Scheme 5 model G-Vs as lines, (5 A, blue; 5 B, green; and 5 C, red). Model G-V $V_{1/2S}$: $+7.5$ ($k = 17.5$ mV, 5 A), $+24.3$ ($k = 22.3$ mV, 5 B), and $+38.9$ mV ($k = 20.9$ mV, 5 C). Experimental data are symbols (mean \pm SEM). **(C)** Δt -V relations for Scheme 5, A-C, as lines, overlaying experimental data from tsA210 cells. **(D)** τ_{act} -V relations for Scheme 5, A-C, as lines, model currents fit after the first 1 s of the 10 s activation pulse and EQ, EQ^*Q+E1 , $EQ^*QQ^*Q^*+E1$ experimental time constant data as circles (mean \pm SEM).

Downloaded from [https://jgpess.org/jgp/article-pdf/115/6/362/202313465.pdf](https://jgpress.org/jgp/article-pdf/115/6/362/202313465.pdf) by guest on 22 May 2023

First, the Δt -V relationship should be zero for the single subunit, but it is not, and in the other two models, the Δt values are depressed below those expected from models based on the current relaxation time constants (τ_{act} , Fig. 3, C and D), where subunit activation determines both the delay in opening and subsequent activation of I_{Ks} . Although values negative to 0 mV were difficult to obtain, it appears that the Δt -V relationships have a bell-shaped voltage dependence, which suggests a process governed by a single transition with voltage-dependent forward and backward rate constants (Horrigan et al., 1999), and is consistent with the mainly exponential time course of I_{Ks} .

activation (Fig. 3, A and B; and Figs. S2 and S4). The existence of a delay in the $EQ^*QQ^*Q^*+E1$ single activatable subunit Δt -V data indicates that multiple transition steps must occur for each subunit VS, and wt and EQ^*Q+E1 Δt -V data show that models based on the measured activation time constants produce Δt values that are about twice as long as experimental values. This suggests that slower steps in activation gating are not accounted for in the models, which limits the speed of exponential current relaxation during opening. In I_{Ks} channels, it is the interaction of the KCNE1 subunit, associated with KCNQ1, that causes this very slow exponential relaxation of currents, since it is not present in

KCNQ1 channels expressed alone (Fig. 1 A). Further, **Scheme 1** models do not take into account that the delay duration may be influenced by the presence of multiple open states if they exist, and therefore also transitions between closed and open states and between open states themselves.

Secondly, the **Scheme 1** models predict that τ_{act} kinetics will converge at potentials between +140 and +180 mV, but no such convergence was seen experimentally as relatively stable time constant ratios between wt, EQ*Q+E1 and EQ*QQ*Q*+E1 of 0.6 and 0.4, respectively, were maintained out to +180 mV (Fig. 3 B), the limit of our ability to record currents and maintain seals in tsA201 cells. Eq. 3 predicts a linear relationship between Δt and τ_{act} , but this was observed neither experimentally nor in the models (Fig. 3 D). To reproduce the experimental method, simulated Δt values were obtained by fitting the output model currents to obtain Δt and τ_{act} . Longer simulation test pulses improved the linearity of Δt versus τ_{act} curves (Fig. S3), and we conclude that to approach the theoretical relationship described by Eq. 3, experimental pulse durations would need to be longer than 20 s. Most of our experimental data were obtained from 10-s pulses, or 20 s at voltages around 0 mV, and the curvature of the experimental relationships closely matches the model curves for 10–20 s pulse durations. It would not have been practical in mammalian cells to use 50- or 100-s duration pulses to get better fits for τ_{act} at voltages around and below 0 mV. The remaining curvature of the model Δt versus τ_{act} curves obtained from pulses longer than 50 s can be attributed to other terms in the binomial expansion that defines I_{Ks} activation with multiple subunits (Horrigan et al., 1999).

Thirdly, **Scheme 1** models predict that the optimized isochronal G-V relationships should shift to more positive potentials and become steeper as more subunits are added in **Scheme 1, B and A** (Fig. 1). Experimentally, the G-V relations do become steeper by about the right amount, but they are hyperpolarized and displaced in the opposite direction, as we had previously observed using data from cells that were not HMR1556-subtracted (Westhoff et al., 2019).

Sequential gating models with an added concerted gating step
Scheme 2 models incorporate a concerted gating step, with an additional set of rate constants, that represents a slower and concerted conformational change of the VS and channel gate, which is required to regulate the time course of exponential current relaxation, as pointed out during the **Scheme 1** analysis (Figs. 1, 2, and 3). Rate constants for such models can be obtained from the activation delay and exponential current activation kinetics as long as VS activation is much faster than the kinetics of the closed to open transition (Horrigan et al., 1999). In our experiments, we avoided this issue by making direct measurements of VS movement during activation using fluorescence spectroscopy.

Apart from being able to measure fluorescence from labeled cysteine residues in oocytes, a further advantage of using oocytes is that they can be held at -140 mV for extended periods to place channels in their ground closed states (Fig. S4), and pulsed to potentials as negative as -180 mV for a number of seconds. Double exponential fits of the resulting fluorescence records

allowed separation of F1 and F2 components and calculation of rate constants for the two VS steps (Fig. 5 and Table 2) that were then incorporated into **Scheme 2** models. These models simulated the isochronal data very well, but again did not simulate the transient kinetics well. This is perhaps not surprising; both in our experiments (Fig. 4) and those described previously, VS fluorescence pulse durations are limited to 2–5 s to minimize photobleaching of the Alexa Fluor 488 dye (Osteen et al., 2010; Barro-Soria et al., 2014; Zayzman et al., 2014; Westhoff et al., 2019), while current activation can take over 10 s at the $V_{1/2}$ in both mammalian cells and oocytes (Fig. 3 B and Fig. 6 B). Optimization slowed rates in the models for both VS transitions (Table 2), and allowed **Scheme 2** psQ+E1 and psQQ*+E1 model outputs to fit transient as well as isochronal experimental data (lines in Fig. 6 B). Importantly, however, models still did not predict the hyperpolarization of the G-V as more active subunits are present and the shift is only apparent in the isochronal model fits (Fig. 6 A) because of the different experimental rates pertinent to psQ+E1 and psQQ*+E1 (Fig. 5 and Table 2) that were used in the separate models. The Boltzmann parameters from fits to the F1-V component of fluorescence from psQ+E1 and psQQ*+E1 (Table 1), and the F1 rate constants that were obtained from fits to the F1 fluorescence time course (Table 2) were almost identical, despite the fact that two of the four VSs in the psQQ*+E1 construct were being prevented from outward displacement during activation. This F1 matching, plus the reduction of the total fluorescence attributable to F1 versus F2 in psQQ*+E1 data compared with psQ+E1 (Fig. 4), strongly supports the idea that the component of VS movement reflected in F1 is independent of the position, fixed or otherwise, of the other VSs, and is expected for independent movement of VSs, which is an axiom of all the models examined in this paper.

Experimental data have suggested that the second VS step is very closely associated with channel gate opening, and mutations in some subunits that shifted the voltage dependence of channel opening to more positive potentials, or drugs that prevented channel gate opening also shifted the voltage-dependence or prevent the appearance of the second phase of fluorescence (Barro-Soria et al., 2014). Still, it did seem possible that the second VS step could be divorced from channel gate opening, and so we constructed **Scheme 3** models to represent the possible closed channel conformations in situations where the two VS steps occur between closed channel states, but occupancy of a single open state remains contingent on a transition that occurs after the concerted movement of all available subunits. We found two significant mismatches between experimental observations and model simulations using **Scheme 3** models which meant that we did not pursue these models further. The first was that the voltage dependence of the F2-V fluorescence component was no longer tied to channel gate opening and therefore to the G-V, so that in most simulation results, the F2-V no longer overlaid with the voltage dependence of the G-V (Fig. 7). This was a significant problem, as in all published data, F2 in pseudo-wt channels or in the presence of mutations like F351A, F232A, or E160R, tracks closely with the G-V (Osteen et al., 2010; Barro-Soria et al., 2014, 2017; Zayzman et al., 2014; Westhoff et al., 2019; Wu et al., 2021). The second

was that the hyperpolarization of the isochronal G-V with four versus two VSs was still not observed which meant that one of our key experimental findings could not be simulated by any of the **Scheme 2** or **3** models.

Schemes 4 and 5 allosteric activation models of I_{Ks}

At very positive potentials in the **Schemes 1, 2**, and **3** models which possess a single open state, the current relaxation time constants during the exponential phase approximate to $1/\alpha$ or $1/\delta$. In contrast, in the **Schemes 4** and **5** models, the channels undergo rate-limiting conformational changes from multiple closed to open states, which are allosterically regulated. The result is that if horizontal transitions equilibrate rapidly, the maximum current relaxation rate will remain faster even at very positive potentials in channels with more activatable VSs, in the ratio of D⁴:D² for a four or two subunit channel, respectively. This was observed experimentally (**Fig. 3 B**), and the ratios of the τ_{act} -V between wt, EQ*Q+E1, and EQ*QQ*Q*+E1 allowed us to calculate a value of 1.357 for the allosteric factor (D). The limiting slope experiments (**Fig. 8**) provide additional support for models with multiple open states, as the deviation of the Po-V curve from linearity at negative voltages is consistent with access of channels to open states from ground closed states and those only part way along the horizontal activation pathways of **Schemes 4** and **5** (**Fig. 11**). Using 1.357 in the model, with equal conductance of early and final open states (O_{RRRR}, O_{RRRA}, and O_{AAAA}) to generate the Po-V curve, gave the closest approximation to the Po-V recorded experimentally (**Fig. 10 D**), and there was no indication that D was going to be a much higher value. Allosteric factors have been calculated from fits to data from Shaker channels ($k = 7$; McCormack et al., 1994), and BK channels in the absence of Ca²⁺, where D had a value of 17 (Horrigan et al., 1999) - much higher than our value of 1.357. In HCN channels, the allosteric factor was fixed as a fraction (0.2) of the ratio of reverse:forward rates, and did not depend on the number of "willing" VSs (Altomare et al., 2001). In KCNQ1 channels without KCNE1, values of the allosteric factor for different mutants varied between 2.04 and 6.08 (Osteen et al., 2012), values much closer to ours.

Scheme 4 model simulations with D = 1.357 fit almost all of our experimental data well (**Figs. 9** and **10**), surprisingly so given the simplicity of this model and the fact that both isochronal and transient kinetic data span a wide range of voltages and two experimental models. A relatively low value for the allosteric factor might suggest that conduction through intermediate open states along the activation pathway would be significant. However, this tendency for opening from intermediate closed states is counteracted by the relatively rapid F1 kinetics so that channels may activate preferentially across models from left to right and then vertically, rather than in a mixed manner (**Schemes 4** and **5**; and **Fig. S5**).

The voltage-dependence of the G-Vs and F-Vs for both psQ+E1 and psQQ*+E1 and the magnitudes of the G-V and F-V shifts with different numbers of E160R mutant VSs could be fit in **Scheme 4** models after optimization starting from the experimentally obtained rate constants from psQ+E1 (**Fig. 9** and **Table 2**, row 9). It was interesting to note that the foot of the

model G-V relationships for psQ+E1 and psQQ*+E1 remain relatively superimposed as seen in G-V data from EQ, EQ*Q+E1, and EQ*QQ*Q*+E1 expressed in tsA201 cells (**Fig. 1 B**), and this is likely due to the fact that the closed to open transitions for the two models are governed by identical rates for potentials to about -50 mV. While the isochronal G-V and F-V were well modeled, the transient kinetics were again too fast. After optimization to experimental values, the current relaxation time constants, τ_{act} , showed a good agreement with tsA201 experimental data, and like the experiments, the model curves did not converge for the different constructs at potentials up to +300 mV (**Fig. 10 A**), and they also showed a crossover at negative potentials to explain the speeding of current tails in EQ*Q+E1 and EQ*QQ*Q*+E1 versus wt. The Δt activation delays were still not well reproduced in this model (**Fig. 10 B**), and remained about half the experimental values, which depressed the Δt versus τ_{act} relationships (**Fig. 10 C**, solid lines). Changing the model into one with a single conducting open state reached only when all VSs are activated, analogous to **Scheme 2** models, did increase the delay, and the **Scheme 4 A** curve trended up toward the EQ data.

At least one other VS transition is required to adequately simulate the transient activation kinetics. **Scheme 5** models (**Fig. 11**) were built to improve the transient kinetic simulations while preserving the ability to accurately model the steady-state kinetics of I_{Ks} channel currents. As for **Scheme 4**, the **Scheme 5** models heavily relied on rates optimized from experimental F1 fluorescence kinetics to model the horizontal resting-closed to intermediate-closed transitions, and F2 fluorescence kinetics to model the activated-closed to activated-open transitions. A second VS movement was interpolated between these two movements to model intermediate-closed to activated-closed transitions. The concept of intermediate- and activated-closed states was introduced along with the idea of two VS transitions during I_{Ks} activation (Zayzman et al., 2014). The optimized model rates solved the transient kinetics problem and preserved the ability of allosteric models to reproduce the isochronal G-V and F-V kinetics (**Fig. 12**). We have no experimental evidence to support a slow VS transition. But fluorescence recordings that would reveal such a slow VS movement have never been made, to our knowledge, for the reasons discussed in the Results. Such transients would probably be small and very slow, and any attempt to record these would face significant photobleaching issues. The unified **Scheme 5** rates (**Table 2**, row 10) applied to **Scheme 5, B** and **C**, models did not reproduce the degree of downward displacement of the Δt delay kinetics in **Scheme 5 C** compared with **Scheme 5 A** (**Fig. S6**) that was seen experimentally (**Fig. 3 D**). In the **Scheme 5** models, the conductance of all the viable open states (colored purple in **Fig. 11**) was set to be the same, for simplicity, but this has the effect that in all the models exponential current development can occur as soon as they access open states in the activation pathway. Experimentally, it has been shown that these open states are likely of different conductance since EQ, EQ*Q+E1, and EQ*QQ*Q*+E1 show progressively diminished peak single-channel amplitudes (Westhoff et al., 2019). Indeed, reducing the peak conductance of the upper tier open states earlier in the activation pathway of **Scheme 5** models does separate the Δt delay

curves of the **Scheme 5** models (not shown), but fully developed models of this type are beyond the scope of our study, which attempts to simulate whole cell/oocyte rather than single channel kinetic data. The unified **Scheme 5** rates, which were based on optimization of EQ and psQ+E1 data, fitted the wt experimental activation kinetics extremely well and also fitted much of the kinetic data from EQ*Q+E1, psQQ*+E1, and EQ*QQ*Q*+E1 constructs as well (Fig. 12). Our solution to the problem discussed above is to provide optimized rates specifically for the EQ*Q+E1 (**Scheme 5 B**) and EQ*QQ*Q*+E1 (**Scheme 5 C**) models (Table 2, rows 11 and 12) that are able to fully simulate all the current kinetics seen experimentally in these constructs (Fig. 13).

Pore-VS coupling

The nature of the allosteric switching between the activated-closed and activated-open conducting channel pore in the presence of individual activated VS in KCNQ1:KCNE1 channels is likely to be extremely complex (reviewed in Wang et al., 2020), and understanding VS-PD coupling is generally beyond the experimental and modeling studies presented here. The reader is directed to experimental studies that examine VS-PD coupling in some detail (Zayzman et al., 2013; Zayzman and Cui, 2014) and models of the VS-PD coupling in KCNQ1 channels (Zayzman et al., 2014; Westhoff et al., 2019) for a comprehensive analysis and model usage. Recent structural data suggest that perhaps the VS may not have evolved in KCNQ1 to open the channel but rather to impart voltage-dependent access to PIP₂ (Mandala and MacKinnon 2023). In a manner analogous to many multimeric proteins, acting as a switch between two parallel conformational pathways (Ackers et al., 1992), PIP₂ binding might then act to displace calmodulin (CaM) from the S2-S3 linker and allow the opening of the channel (Sun and MacKinnon, 2020). As PIP₂ is thought to act after VS activation, it is not surprising that depletion of PIP₂ does not affect the VS, with no apparent change in the F-V of I_{Ks} , although currents are eliminated (Barro-Soria et al., 2017). On the other hand, the G-V has been shown to be affected by increases in PIP₂ concentration, with the V_{1/2} shifting to more negative potentials upon patch excision into PIP₂-containing bath solutions (Loussouarn et al., 2003; Li et al., 2011) and a concurrent slowing of deactivation. This G-V shift suggests that not all channels are saturated with PIP₂ under typical recording conditions and that when the channel is saturated with PIP₂, channel opening is easier. This is in contrast to when E160R-containing VSs are unable to activate and the V_{1/2} of the G-V shifts to more depolarized voltages with an increasing number of E160R mutations in the channel complex (Fig. 1 B). We know that this shift takes place even in the absence of KCNE1 (Westhoff et al., 2019), so it is unrelated to the E1 subunit and preferentially affects the V_{1/2} of the G-V and F2-V relationships and the relative amplitude of the F2 compared with the F1 component of the F-V (Fig. 4 B). The preservation of F2 may reflect VS-pore interactions that change the environment of the fluorophore attached at 219C even in VSs that contain E160R mutations. This would make sense in light of compounds like UCL 2077 that prevent channel opening and abolish F2 (Barro-Soria et al., 2014), but is not supported by the observation that depletion of PIP₂ using the voltage-sensitive phosphatase from

Ciona intestinalis prevents pore opening but does not affect either component of the F-V (Barro-Soria et al., 2017).

Morphing the new low-resolution KCNQ1 resting-state structural model (PDB ID 8sin; Mandala and MacKinnon, 2023) into the activated-open-state structure of KCNQ1/KCNE3/PIP₂ (PDB ID 6v01; Sun and MacKinnon, 2020) highlights the rearrangements that take place within the cytoplasmic C-terminus of the complex. To open, the S6 transmembrane domain becomes continuous with the helix A portion of the C-terminal domain of the channel, and as it splays open, CaM rotates around the helix A-helix B segment into the space where a CaM on a neighboring subunit would reside in the closed state. In E160R-containing VSs where activation is prevented, the mutation may create a steric hindrance to the opening where a moving CaM would bump into a static CaM and make the opening transition more energetically difficult. This would explain the depolarizing V_{1/2} shift in E160R-containing complexes and in those not fully saturated with PIP₂. In contrast, a hyperpolarizing V_{1/2} shift occurs when the pore is propped open by an increasing number of L353K mutations in the channel complex (Meisel et al., 2012), where presumably CaM molecules bound to mutated subunits are already out of the way of those remaining subunits that are starting from a closed pore configuration. Not surprisingly, several mutations in CaM linked to long QT-interval syndrome are also known to shift the V_{1/2} of I_{Ks} to more positive potentials (McCormick et al., 2023).

Conclusion

Having examined both sequential and allosteric models for I_{Ks} gating, we conclude that only the allosteric models, Schemes 4 and 5, are able to faithfully reproduce the experimentally observed gating behavior, including the Po-V upturn at very low Po values and negative voltages, the depolarization of the EQ*Q+E1 and EQ*QQ*Q*+E1 G-V relationships relative to wt, the relative changes in deactivation rates in the different constructs, and the concordance of the G-V and F2-V relationships from psQ+E1 and psQQ*+E1 oocytes. Sequential Schemes 1, 2, and 3 with and without a concerted opening transition are qualitatively unable to reproduce these phenomena. Our Scheme 5 models present an accurate depiction of I_{Ks} VS activation and current behavior as, using a single set of rate constants, the models are able to reproduce both transient and quasi steady-state experimental kinetics from mammalian cells and oocytes in models with various numbers of active VSs. It appears that I_{Ks} is yet another channel whose gating is consistent with rows (or tiers) of open and closed states, like the Ca²⁺-activated K⁺ channel (Cox et al., 1997; Rothberg and Magleby, 1998, 2000; Horrigan et al., 1999; Cui and Aldrich, 2000), ACh receptor isomerization (Auerbach, 2010), the HCN channel (Altomare et al., 2001), and indeed KCNQ1 itself (Ma et al., 2011; Osteen et al., 2012; Zayzman et al., 2014).

Data availability

Data and the code for the final tiered allosteric model used in the manuscript to generate tables and figures have been deposited in a publicly accessible database at <https://doi.org/10.5281/zenodo.10421153>.

Acknowledgments

Crina M. Nimigean served as editor.

We thank Dr. Jianmin Cui for the C214A/G219C/C331A Q1 construct and Dr. Yoshihiro Kubo for the pGEMHE vector. We thank Yundi Wang and David Chen for their help with preliminary experiments, Fariba Ataei for her technical assistance, and members of the Fedida lab, Drs. Peter Backx and Khanh Dao-Duc for valuable discussion.

This research was funded by the Natural Sciences and Engineering Research Council of Canada (grant #RGPIN-2022-03021), Canadian Institutes of Health Research (#PJT-175024), and Heart and Stroke Foundation of Canada (#G-21-0031566) grants to D. Fedida.

Author contributions: D. Fedida: all MATLAB modeling, tsA201 cell data collection, data analysis, figure preparation, writing of paper draft, revisions, and final version of manuscript. D. Sastre: tsA201 cell and oocyte data collection, data analysis, figure preparation, and review of the final version of the manuscript. M. Westhoff: tsA201 cell and oocyte data collection, review of the final version of the manuscript. Y. Dou: tsA201 cell and oocyte data collection, review of the final version of the manuscript. J. Eldstrom: tsA201 and mouse *ltk*-cell data collection, data analysis, writing and review of the draft paper, and review of the final version of the manuscript.

Disclosures: The authors declare no competing interests exist.

Submitted: 16 August 2023

Revised: 30 November 2023

Accepted: 3 January 2024

References

- Abrahamyan, A., J. Eldstrom, H. Sahakyan, N. Karagulyan, L. Mkrtchyan, T. Karapetyan, E. Sargsyan, M. Kneussel, K. Nazaryan, J.R. Schwarz, et al. 2023. Mechanism of external K⁺ sensitivity of KCNQ1 channels. *J. Gen. Physiol.* 155:e202213205. <https://doi.org/10.1085/jgp.202213205>
- Ackers, G.K., M.L. Doyle, D. Myers, and M.A. Daugherty. 1992. Molecular code for cooperativity in hemoglobin. *Science*. 255:54–63. <https://doi.org/10.1126/science.1553532>
- Altomare, C., A. Bucchi, E. Camatini, M. Baruscotti, C. Visconti, A. Moroni, and D. DiFrancesco. 2001. Integrated allosteric model of voltage gating of HCN channels. *J. Gen. Physiol.* 117:519–532. <https://doi.org/10.1085/jgp.117.6.519>
- Auerbach, A. 2010. The gating isomerization of neuromuscular acetylcholine receptors. *J. Physiol.* 588:573–586. <https://doi.org/10.1113/jphysiol.2009.182774>
- Barro-Soria, R., R. Ramentol, S.I. Liin, M.E. Perez, R.S. Kass, and H.P. Larsson. 2017. KCNE1 and KCNE3 modulate KCNQ1 channels by affecting different gating transitions. *Proc. Natl. Acad. Sci. USA*. 114:E7367–E7376. <https://doi.org/10.1073/pnas.1710335114>
- Barro-Soria, R., S. Rebollo, S.I. Liin, M.E. Perez, K.J. Sampson, R.S. Kass, and H.P. Larsson. 2014. KCNE1 divides the voltage sensor movement in KCNQ1/KCNE1 channels into two steps. *Nat. Commun.* 5:3750. <https://doi.org/10.1038/ncomms4750>
- Bottino, D., R.C. Penland, A. stamps, M. Traebert, B. Dumotier, A. Georgiva, G. Helmlinger, and G.S. Lett. 2006. Preclinical cardiac safety assessment of pharmaceutical compounds using an integrated systems-based computer model of the heart. *Prog. Biophys. Mol. Biol.* 90:414–443. <https://doi.org/10.1016/j.pbiomolbio.2005.06.006>
- Carbonell-Pascual, B., E. Godoy, A. Ferrer, L. Romero, and J.M. Ferrero. 2016. Comparison between Hodgkin-Huxley and Markov formulations of cardiac ion channels. *J. Theor. Biol.* 399:92–102. <https://doi.org/10.1016/j.jtbi.2016.03.039>
- Carnevale, V., L. Delemotte, and R.J. Howard. 2021. Molecular dynamics simulations of ion channels. *Trends Biochem. Sci.* 46:621–622. <https://doi.org/10.1016/j.tibs.2021.04.005>
- Chan, M., H. Sahakyan, J. Eldstrom, D. Sastre, Y. Wang, Y. Dou, M. Pourrier, V. Vardanyan, and D. Fedida. 2023. A generic binding pocket for small molecule IKs activators at the extracellular inter-subunit interface of KCNQ1 and KCNE1 channel complexes. *Elife*. 12:RP87038. <https://doi.org/10.7554/elife.87038>
- Chowdhury, S., and B. Chanda. 2012a. Estimating the voltage-dependent free energy change of ion channels using the median voltage for activation. *J. Gen. Physiol.* 139:3–17. <https://doi.org/10.1085/jgp.20110722>
- Chowdhury, S., and B. Chanda. 2012b. Perspectives on: Conformational coupling in ion channels: Thermodynamics of electromechanical coupling in voltage-gated ion channels. *J. Gen. Physiol.* 140:613–623. <https://doi.org/10.1085/jgp.201210840>
- Clerx, M., K.A. Beattie, D.J. Gavaghan, and G.R. Mirams. 2019. Four ways to fit an ion channel model. *Biophys. J.* 117:2420–2437. <https://doi.org/10.1016/j.bpj.2019.08.001>
- Cole, K.S., and J.W. Moore. 1960. Potassium ion current in the squid giant axon: Dynamic characteristic. *Biophys. J.* 1:1–14. [https://doi.org/10.1016/S0006-3495\(60\)86871-3](https://doi.org/10.1016/S0006-3495(60)86871-3)
- Colquhoun, D., and A.G. Hawkes. 1977. Relaxation and fluctuations of membrane currents that flow through drug-operated channels. *Proc. R. Soc. Lond. B.* 199:231–262. <https://doi.org/10.1098/rspb.1977.0137>
- Cox, D.H., J. Cui, and R.W. Aldrich. 1997. Allosteric gating of a large conductance Ca-activated K⁺ channel. *J. Gen. Physiol.* 110:257–281. <https://doi.org/10.1085/jgp.110.3.257>
- Cui, J., and R.W. Aldrich. 2000. Allosteric linkage between voltage and Ca(2+)-dependent activation of BK-type mslo1 K(+) channels. *Biochemistry*. 39:15612–15619. <https://doi.org/10.1021/bi001509+>
- D'Errico, J. 2021. fminsearchbnd, fminsearchcon, MATLAB Central File Exchange URL. <https://www.mathworks.com/matlabcentral/fileexchange/8277-fminsearchbnd-fminsearchcon>.
- Eldstrom, J., D.A. McAfee, Y. Dou, Y. Wang, and D. Fedida. 2021. ML277 regulates KCNQ1 single-channel amplitudes and kinetics, modified by voltage sensor state. *J. Gen. Physiol.* 153:e202112969. <https://doi.org/10.1085/jgp.202112969>
- Es-Salah-Lamoureux, Z., R. Fougeré, P.Y. Xiong, G.A. Robertson, and D. Fedida. 2010. Fluorescence-tracking of activation gating in human ERG channels reveals rapid S4 movement and slow pore opening. *PLoS One*. 5:e10876. <https://doi.org/10.1371/journal.pone.0010876>
- Fitzhugh, R. 1965. A kinetic model of the conductance changes in nerve membrane. *J. Cell. Comp. Physiol.* 66:111–118. <https://doi.org/10.1002/jcp.10366060518>
- Flood, E., C. Boiteux, B. Lev, I. Vorobyov, and T.W. Allen. 2019. Atomistic simulations of membrane ion channel conduction, gating, and modulation. *Chem. Rev.* 119:7737–7832. <https://doi.org/10.1021/acs.chemrev.8b00630>
- Gagnon, D.G., and F. Bezanilla. 2009. A single charged voltage sensor is capable of gating the Shaker K⁺ channel. *J. Gen. Physiol.* 133:467–483. <https://doi.org/10.1085/jgp.200810082>
- Hafner, D., U. Borchard, O. Richter, and M. Neugebauer. 1981. Parameter estimation in Hodgkin-Huxley-type equations for membrane action potentials in nerve and heart muscle. *J. Theor. Biol.* 91:321–345. [https://doi.org/10.1016/0022-5193\(81\)90236-8](https://doi.org/10.1016/0022-5193(81)90236-8)
- Hille, B. 2001. Ion Channels of Excitable Membranes. Third edition. Sinauer Associates Inc., Sunderland, MA.
- Hodgkin, A.L., and A.F. Huxley. 1952. A quantitative description of membrane current and its application to conduction and excitation in nerve. *J. Physiol.* 117:500–544. <https://doi.org/10.1113/jphysiol.1952.sp004764>
- Horrigan, F.T. 2012. Perspectives on: Conformational coupling in ion channels: Conformational coupling in BK potassium channels. *J. Gen. Physiol.* 140:625–634. <https://doi.org/10.1085/jgp.201210849>
- Horrigan, F.T., and R.W. Aldrich. 2002. Coupling between voltage sensor activation, Ca²⁺ binding and channel opening in large conductance (BK) potassium channels. *J. Gen. Physiol.* 120:267–305. <https://doi.org/10.1085/jgp.20028605>
- Horrigan, F.T., J. Cui, and R.W. Aldrich. 1999. Allosteric voltage gating of potassium channels I. Mslo ionic currents in the absence of Ca(2+). *J. Gen. Physiol.* 114:277–304. <https://doi.org/10.1085/jgp.114.2.277>
- Hou, P., J. Eldstrom, J. Shi, L. Zhong, K. McFarland, Y. Gao, D. Fedida, and J. Cui. 2017. Inactivation of KCNQ1 potassium channels reveals dynamic coupling between voltage sensing and pore opening. *Nat. Commun.* 8:1730. <https://doi.org/10.1038/s41467-017-01911-8>
- Hou, P., P.W. Kang, A.D. Kongmenck, N.D. Yang, Y. Liu, J. Shi, X. Xu, K.M. White, M.A. Zayzman, M.A. Kasimova, et al. 2020. Two-stage electro-

- mechanical coupling of a K_v channel in voltage-dependent activation. *Nat. Commun.* 11:676. <https://doi.org/10.1038/s41467-020-14406-w>
- Kernik, D.C., S. Morotti, H. Wu, P. Garg, H.J. Duff, J. Kurokawa, J. Jalife, J.C. Wu, E. Grandi, and C.E. Clancy. 2019. A computational model of induced pluripotent stem-cell derived cardiomyocytes incorporating experimental variability from multiple data sources. *J. Physiol.* 597:4533–4564. <https://doi.org/10.1113/P277724>
- Kernik, D.C., P.C. Yang, J. Kurokawa, J.C. Wu, and C.E. Clancy. 2020. A computational model of induced pluripotent stem-cell derived cardiomyocytes for high throughput risk stratification of KCNQ1 genetic variants. *PLoS Comput. Biol.* 16:e1008109. <https://doi.org/10.1371/journal.pcbi.1008109>
- Kuenze, G., C.G. Vanoye, R.R. Desai, S. Adusumilli, K.R. Brewer, H. Woods, E.F. McDonald, C.R. Sanders, A.L. George Jr., and J. Meiler. 2020. Allosteric mechanism for KCNE1 modulation of KCNQ1 potassium channel activation. *Elife.* 9:e57680. <https://doi.org/10.7554/eLife.57680>
- Ledwell, J.L., and R.W. Aldrich. 1999. Mutations in the S4 region isolate the final voltage-dependent cooperative step in potassium channel activation. *J. Gen. Physiol.* 113:389–414. <https://doi.org/10.1085/jgp.113.3.389>
- Li, Y., M.A. Zayzman, D. Wu, J. Shi, M. Guan, B. Virgin-Downey, and J. Cui. 2011. KCNE1 enhances phosphatidylinositol 4,5-bisphosphate (PIP₂) sensitivity of IKs to modulate channel activity. *Proc. Natl. Acad. Sci. USA.* 108:9095–9100. <https://doi.org/10.1073/pnas.1100872108>
- Li, Z., B.J. Ridder, X. Han, W.W. Wu, J. Sheng, P.N. Tran, M. Wu, A. Randolph, R.H. Johnstone, G.R. Mirams, et al. 2019. Assessment of an in silico mechanistic model for proarrhythmia risk prediction under the CiPA initiative. *Clin. Pharmacol. Ther.* 105:466–475. <https://doi.org/10.1002/cpt.1184>
- Loussouarn, G., K.H. Park, C. Bellocq, I. Baró, F. Charpentier, and D. Escande. 2003. Phosphatidylinositol-4,5-bisphosphate, PIP₂, controls KCNQ1/KCNE1 voltage-gated potassium channels: A functional homology between voltage-gated and inward rectifier K⁺ channels. *EMBO J.* 22: 5412–5421. <https://doi.org/10.1093/emboj/cdg526>
- Ma, L.J., I. Ohmert, and V. Vardanyan. 2011. Allosteric features of KCNQ1 gating revealed by alanine scanning mutagenesis. *Biophys. J.* 100: 885–894. <https://doi.org/10.1016/j.bpj.2010.12.3726>
- Maly, J., A.M. Emigh, K.R. DeMarco, K. Furutani, J.T. Sack, C.E. Clancy, I. Vorob'yov, and V. Yarov-Yarovoy. 2022. Structural modeling of the hERG potassium channel and associated drug interactions. *Front. Pharmacol.* 13:966463. <https://doi.org/10.3389/fphar.2022.966463>
- Mandala, V.S., and R. MacKinnon. 2023. The membrane electric field regulates the PIP₂-binding site to gate the KCNQ1 channel. *Proc. Natl. Acad. Sci. USA.* 120:e2301985120. <https://doi.org/10.1073/pnas.2301985120>
- McCormack, K., W.J. Joiner, and S.H. Heinemann. 1994. A characterization of the activating structural rearrangements in voltage-dependent Shaker K⁺ channels. *Neuron.* 12:301–315. [https://doi.org/10.1016/0896-6273\(94\)90273-9](https://doi.org/10.1016/0896-6273(94)90273-9)
- McCormick, L., K. Wadmore, A. Milburn, N. Gupta, R. Morris, M. Held, O. Prakash, J. Carr, R. Barrett-Jolley, C. Dart, and N. Helassa. 2023. Long QT syndrome-associated calmodulin variants disrupt the activity of the slowly activating delayed rectifier potassium channel. *J. Physiol.* 601: 3739–3764. <https://doi.org/10.1113/JP284994>
- Meisel, E., M. Dvir, Y. Haitin, M. Giladi, A. Peretz, and B. Attali. 2012. KCNQ1 channels do not undergo concerted but sequential gating transitions in both the absence and the presence of KCNE1 protein. *J. Biol. Chem.* 287: 34212–34224. <https://doi.org/10.1074/jbc.M112.364901>
- Moreno, J.D., T.J. Lewis, and C.E. Clancy. 2016. Parameterization for in-silico modeling of ion channel interactions with drugs. *PLoS One.* 11:e0150761. <https://doi.org/10.1371/journal.pone.0150761>
- Moreno, J.D., P.C. Yang, J.R. Bankston, E. Grandi, D.M. Bers, R.S. Kass, and C.E. Clancy. 2013. Ranolazine for congenital and acquired late INa-linked arrhythmias: In silico pharmacological screening. *Circ. Res.* 113: e50–e61. <https://doi.org/10.1161/CIRCRESAHA.113.301971>
- Murray, C.I., M. Westhoff, J. Eldstrom, E. Thompson, R. Emes, and D. Fedida. 2016. Unnatural amino acid photo-crosslinking of the IKs channel complex demonstrates a KCNE1:KCNQ1 stoichiometry of up to 4:4. *Elife.* 5:e1815. <https://doi.org/10.7554/eLife.11815>
- Nekouzadeh, A., J.R. Silva, and Y. Rudy. 2008. Modeling subunit cooperativity in opening of tetrameric ion channels. *Biophys. J.* 95:3510–3520. <https://doi.org/10.1529/biophysj.108.136721>
- Nelder, J., and R. Mead. 1965. A simplex method for function minimization. *Comput. J.* 7:308–313. <https://doi.org/10.1093/comjnl/7.4.308>
- O'Hara, T., L. Virág, A. Varró, and Y. Rudy. 2011. Simulation of the undiseased human cardiac ventricular action potential: Model formulation and experimental validation. *PLoS Comput. Biol.* 7:e1002061. <https://doi.org/10.1371/journal.pcbi.1002061>
- Osteen, J.D., R. Barro-Soria, S. Robey, K.J. Sampson, R.S. Kass, and H.P. Larsson. 2012. Allosteric gating mechanism underlies the flexible gating of KCNQ1 potassium channels. *Proc. Natl. Acad. Sci. USA.* 109:7103–7108. <https://doi.org/10.1073/pnas.1201582109>
- Osteen, J.D., C. Gonzalez, K.J. Sampson, V. Iyer, S. Rebollo, H.P. Larsson, and R.S. Kass. 2010. KCNE1 alters the voltage sensor movements necessary to open the KCNQ1 channel gate. *Proc. Natl. Acad. Sci. USA.* 107: 22710–22715. <https://doi.org/10.1073/pnas.1016300108>
- Paci, M., J. Hyttinen, K. Aalto-Setälä, and S. Severi. 2013. Computational models of ventricular- and atrial-like human induced pluripotent stem cell derived cardiomyocytes. *Ann. Biomed. Eng.* 41:2334–2348. <https://doi.org/10.1007/s10439-013-0833-3>
- Passini, E., O.J. Britton, H.R. Lu, J. Rohrbacher, A.N. Hermans, D.J. Gallacher, R.J.H. Greig, A. Bueno-Orovio, and B. Rodriguez. 2017. Human in silico drug trials demonstrate higher accuracy than animal models in predicting clinical pro-arrhythmic cardiotoxicity. *Front. Physiol.* 8:668. <https://doi.org/10.3389/fphys.2017.00668>
- Pusch, M., L. Ferrera, and T. Friedrich. 2001. Two open states and rate-limiting gating steps revealed by intracellular Na⁺ block of human KCNQ1 and KCNQ1/KCNE1 K⁺ channels. *J. Physiol.* 533:135–143. <https://doi.org/10.1111/j.1469-7793.2001.0135b.x>
- Pusch, M., R. Magrassi, B. Wollnik, and F. Conti. 1998. Activation and inactivation of homomeric KvLQT1 potassium channels. *Biophys. J.* 75: 785–792. [https://doi.org/10.1016/S0006-3495\(98\)77568-X](https://doi.org/10.1016/S0006-3495(98)77568-X)
- Ramasubramanian, S., and Y. Rudy. 2018. The structural basis of IKs ion-channel activation: Mechanistic insights from molecular simulations. *Biophys. J.* 114:2584–2594. <https://doi.org/10.1016/j.bpj.2018.04.023>
- Restier, L., L. Cheng, and M.C. Sanguinetti. 2008. Mechanisms by which atrial fibrillation-associated mutations in the S1 domain of KCNQ1 slow deactivation of IKs channels. *J. Physiol.* 586:4179–4191. <https://doi.org/10.1113/jphysiol.2008.157511>
- Rothberg, B.S., and K.L. Magleby. 1998. Kinetic structure of large-conductance Ca²⁺-activated K⁺ channels suggests that the gating includes transitions through intermediate or secondary states. A mechanism for flickers. *J. Gen. Physiol.* 111:751–780. <https://doi.org/10.1085/jgp.111.6.751>
- Rothberg, B.S., and K.L. Magleby. 2000. Voltage and Ca²⁺ activation of single large-conductance Ca²⁺-activated K⁺ channels described by a two-tiered allosteric gating mechanism. *J. Gen. Physiol.* 116:75–99. <https://doi.org/10.1085/jgp.116.1.75>
- Ruscic, K.J., F. Miceli, C.A. Villalba-Galea, H. Dai, Y. Mishina, F. Bezanilla, and S.A. Goldstein. 2013. IKs channels open slowly because KCNE1 accessory subunits slow the movement of S4 voltage sensors in KCNQ1 pore-forming subunits. *Proc. Natl. Acad. Sci. USA.* 110:E559–E566. <https://doi.org/10.1073/pnas.1222616110>
- Santiago-Castillo, J.A., M. Covarrubias, J.E. Sánchez-Rodríguez, P. Pérez-Cornejo, and J. Arreola. 2010. Simulating complex ion channel kinetics with IonChannelLab. *Channels.* 4:422–428. <https://doi.org/10.4161/chan.4.5.13404>
- Schoppa, N.E., K. McCormack, M.A. Tanouye, and F.J. Sigworth. 1992. The size of gating charge in wild-type and mutant Shaker potassium channels. *Science.* 255:1712–1715. <https://doi.org/10.1126/science.1553560>
- Schoppa, N.E., and F.J. Sigworth. 1998aa. Activation of shaker potassium channels. I. Characterization of voltage-dependent transitions. *J. Gen. Physiol.* 111:271–294. <https://doi.org/10.1085/jgp.111.2.271>
- Schoppa, N.E., and F.J. Sigworth. 1998bb. Activation of Shaker potassium channels. III. An activation gating model for wild-type and V2 mutant channels. *J. Gen. Physiol.* 111:313–342. <https://doi.org/10.1085/jgp.111.2.313>
- Sigworth, F.J. 1994. Voltage gating of ion channels. *Q. Rev. Biophys.* 27:1–40. <https://doi.org/10.1017/S003358350002894>
- Silva, J., and Y. Rudy. 2005. Subunit interaction determines IKs participation in cardiac repolarization and repolarization reserve. *Circulation.* 112: 1384–1391. <https://doi.org/10.1161/CIRCULATIONAHA.105.543306>
- Sun, J., and R. MacKinnon. 2020. Structural basis of human KCNQ1 modulation and gating. *Cell.* 180:340–347.e9. <https://doi.org/10.1016/j.cell.2019.12.003>
- Tzounopoulos, T., J. Maylie, and J.P. Adelman. 1998. Gating of I(sK) channels expressed in Xenopus oocytes. *Biophys. J.* 74:2299–2305. [https://doi.org/10.1016/S0006-3495\(98\)77939-1](https://doi.org/10.1016/S0006-3495(98)77939-1)
- Wang, Y., J. Eldstrom, and D. Fedida. 2020. Gating and regulation of KCNQ1 and KCNQ1 + KCNE1 channel complexes. *Front. Physiol.* 11:504. <https://doi.org/10.3389/fphys.2020.00504>
- Werry, D., J. Eldstrom, Z. Wang, and D. Fedida. 2013. Single-channel basis for the slow activation of the repolarizing cardiac potassium current, I(Ks). *Proc. Natl. Acad. Sci. USA.* 110:E996–E1005. <https://doi.org/10.1073/pnas.1214875110>

- Westhoff, M., J. Eldstrom, C.I. Murray, E. Thompson, and D. Fedida. 2019. IK_S ion-channel pore conductance can result from individual voltage sensor movements. *Proc. Natl. Acad. Sci. USA.* 116:7879–7888. <https://doi.org/10.1073/pnas.1811623116>
- Westhoff, M., C.I. Murray, J. Eldstrom, and D. Fedida. 2017. Photo-cross-linking of IK_S demonstrates state-dependent interactions between KCNE1 and KCNQ1. *Biophys. J.* 113:415–425. <https://doi.org/10.1016/j.bpj.2017.06.005>
- Willegems, K., J. Eldstrom, E. Kyriakis, F. Ataei, H. Sahakyan, Y. Dou, S. Russo, F. Van Petegem, and D. Fedida. 2022. Structural and electrophysiological basis for the modulation of KCNQ1 channel currents by ML277. *Nat. Commun.* 13:3760. <https://doi.org/10.1038/s41467-022-31526-7>
- Wu, X., M.E. Perez, S.Y. Noskov, and H.P. Larsson. 2021. A general mechanism of KCNE1 modulation of KCNQ1 channels involving non-canonical VSD-PD coupling. *Commun. Biol.* 4:887. <https://doi.org/10.1038/s42003-021-02418-1>
- Zagotta, W.N., T. Hoshi, and R.W. Aldrich. 1994. Shaker potassium channel gating. III: Evaluation of kinetic models for activation. *J. Gen. Physiol.* 103:321–362. <https://doi.org/10.1085/jgp.103.2.321>
- Zaydman, M.A., and J. Cui. 2014. PIP2 regulation of KCNQ channels: Biophysical and molecular mechanisms for lipid modulation of voltage-dependent gating. *Front. Physiol.* 5:195. <https://doi.org/10.3389/fphys.2014.00195>
- Zaydman, M.A., M.A. Kasimova, K. McFarland, Z. Beller, P. Hou, H.E. Kinser, H. Liang, G. Zhang, J. Shi, M. Tarek, and J. Cui. 2014. Domain-domain interactions determine the gating, permeation, pharmacology, and subunit modulation of the IK_S ion channel. *eLife.* 3:e03606. <https://doi.org/10.7554/eLife.03606>
- Zaydman, M.A., J.R. Silva, K. Delaloye, Y. Li, H. Liang, H.P. Larsson, J. Shi, and J. Cui. 2013. Kv7.1 ion channels require a lipid to couple voltage sensing to pore opening. *Proc. Natl. Acad. Sci. USA.* 110:13180–13185. <https://doi.org/10.1073/pnas.1305167110>
- Zhang, M., J. Liu, and G.N. Tseng. 2004. Gating charges in the activation and inactivation processes of the HERG channel. *J. Gen. Physiol.* 124:703–718. <https://doi.org/10.1085/jgp.200409119>
- Zheng, J., L. Vankataraman, and F.J. Sigworth. 2001. Hidden Markov model analysis of intermediate gating steps associated with the pore gate of shaker potassium channels. *J. Gen. Physiol.* 118:547–564. <https://doi.org/10.1085/jgp.118.5.547>

Supplemental material

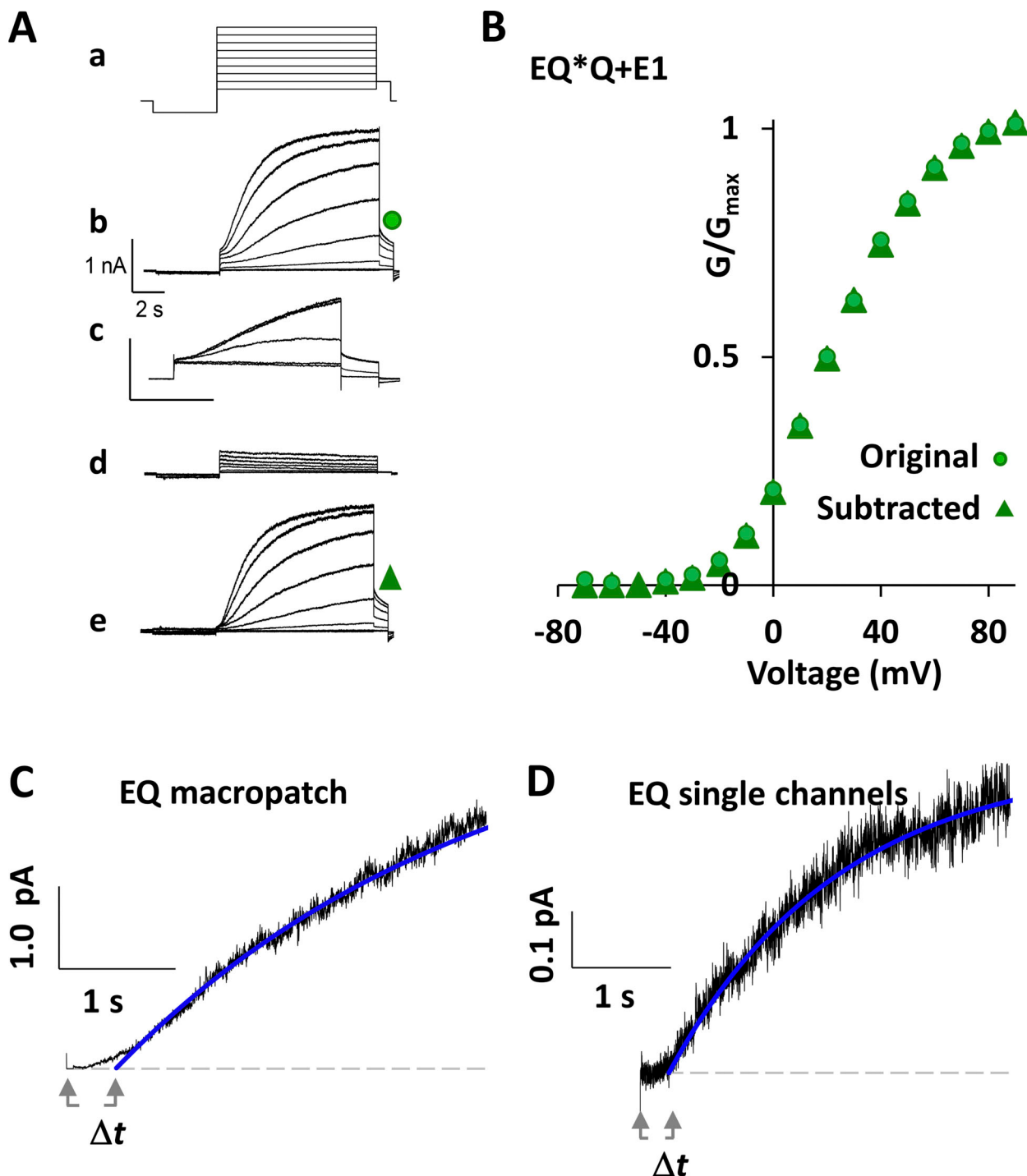


Figure S1. Pedestal current in tsA201 cells removed by endogenous current subtraction without affecting EQ*Q+E1 channel kinetics. (A) Response of EQ*Q+E1 currents in tsA201 cells to 0.3 μ M HMR1556: Aa, Protocol showing 4-s -120 mV prepulse, 10-s test pulse to between -80 and +100 mV, followed by 1-s pulse to -40 mV to record tail currents; Ab, representative current traces in control showing currents to +90 mV in 20 mV steps; Ac, wash-in of HMR1556 at a constant step voltage of +60 mV; Ad, currents in the presence of 0.3 μ M HMR1556; and Ae, subtracted (b-d) currents. The pedestal current in control is removed from subtracted currents as it is unaffected by HMR1556 treatment. Current and time bars in panel b apply also to d and e. Current and time bars in Ac are 1 nA and 2 s. (B) Minimal effect of 0.3 μ M HMR1556 subtraction on EQ*Q+E1 G-V plots. Tail currents measured as indicated in panel A, in control (circles) and after subtraction (triangles). (C) Cell-attached EQ data from a multichannel patch, the cell was held at -120 mV before pulsing to +60 mV for 4 s, fit with a single exponential. Current tracing is the average of 34 sweeps, filtered at 500 Hz. Exponential fit line shown in blue has a τ_{act} of 3.47 s and a Δt of 477 ms. Data show the absence of a pedestal current at the start and measurement of the activation delay, Δt . The activation delay (bracket region) is determined by time from pulse onset (vertical line) to where exponential fits of current growth intersect zero current (horizontal axis dashed line). (D) Single-channel EQ data. Cells were held at -120 mV before pulsing to +60 mV for 4 s. Current tracing is the average of 46 sweeps from a single cell, filtered at 500 Hz. Exponential fit line shown in blue has a τ_{act} of 1.83 s and a Δt of 342 ms. As for C, data show the absence of a pedestal current at the start and measurement of the activation delay, Δt .

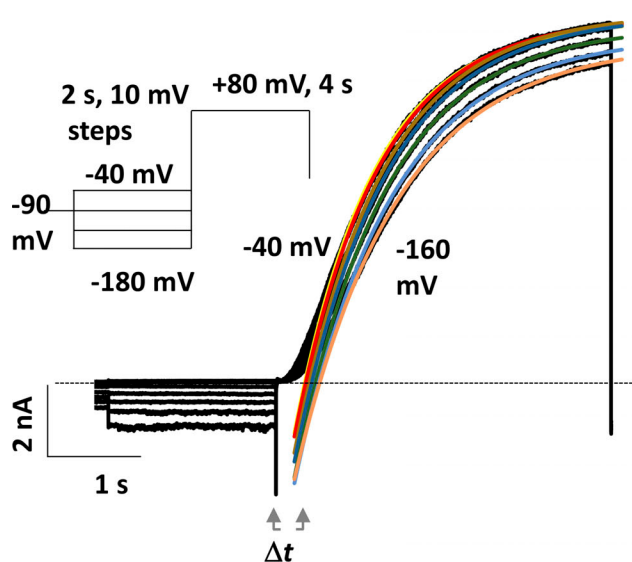
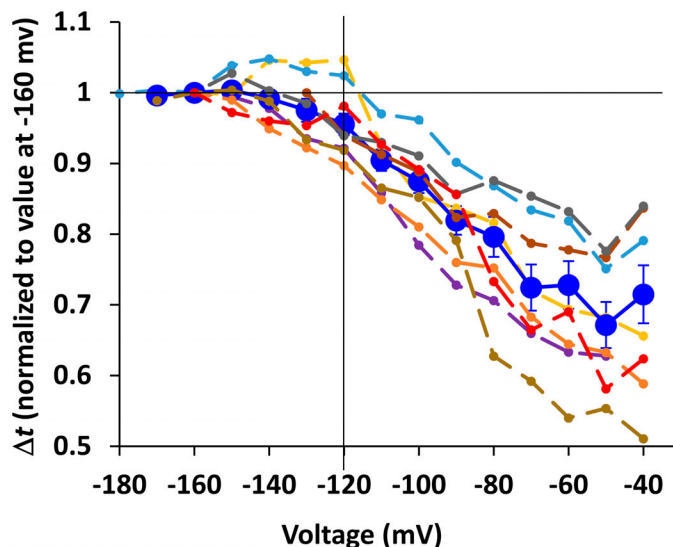
A**B**

Figure S2. Activation delay, Δt , as a function of prepulse potential in tsA201 cells. (A) wt EQ currents (black traces) from a holding potential of -90 mV, with 2-s prepulses in 10 mV steps from -180 to -40 mV, followed by a test pulse to $+80$ mV. Protocol applied every 10 s. Colored lines are exponential fits to the current relaxation time course after a delay (Δt) as shown. Mean τ_{act} was 1.08 ± 0.025 s (SEM, range: 0.952 – 1.24 s). Traces during the step to $+80$ have been leak subtracted to enable Δt measurement. **(B)** Values of Δt normalized to measurement at -160 mV (0.51 ± 0.039 s, mean \pm SEM, $n = 8$). Individual data sets are shown as connected dashed lines and mean data as blue symbols and line. At -120 mV, Δt is $96 \pm 1.5\%$ of its maximum value.

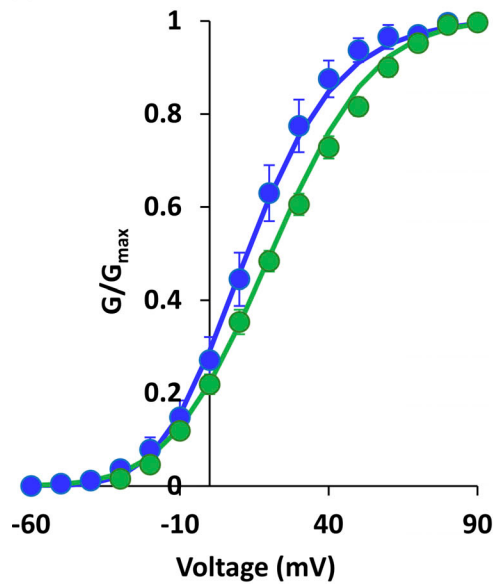
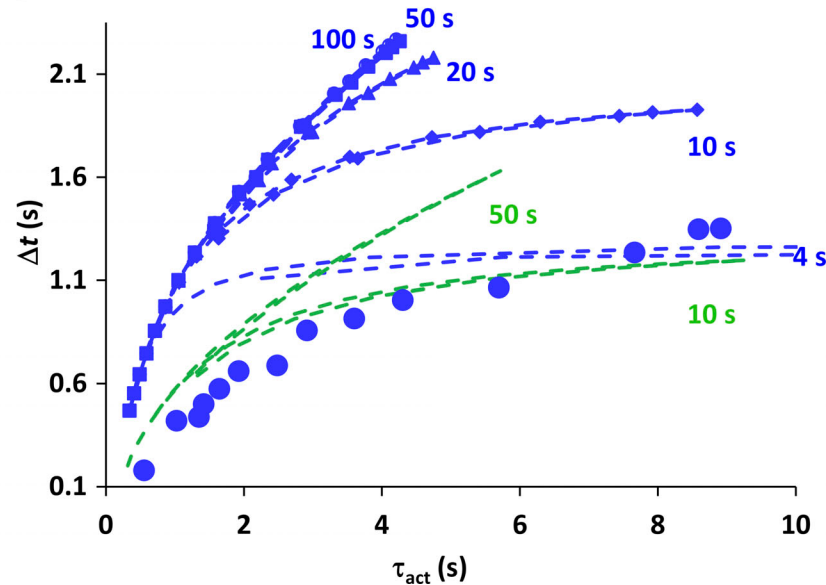
A**B**

Figure S3. Steady-state kinetics of optimized Scheme 1, A and B, models. (A) Mean tsA201 cell G-V data for wt EQ (blue circles; $V_{1/2} = 13.2$ mV, $k = 13.5$ mV, $n = 8$), and EQ*Q+E1 (green circles; $V_{1/2} = 22.3$ mV, $k = 16.8$ mV, $n = 5$). Solid lines show optimized fits using Scheme 1A (blue) and 1B (green) models. Rate constants for fits are shown in Table 2 (rows 3, 4). **(B)** Relationships between Δt and τ_{act} obtained by running the Scheme 1A (blue) and 1B (green) models for 4, 10, 20, 50, and 100 s and fitting the activation of model currents to single exponentials. Note that relationships are curvilinear and no longer change for pulse durations of 50 s or longer. Blue circles are experimental data from the wt EQ construct (Fig. 3 D).

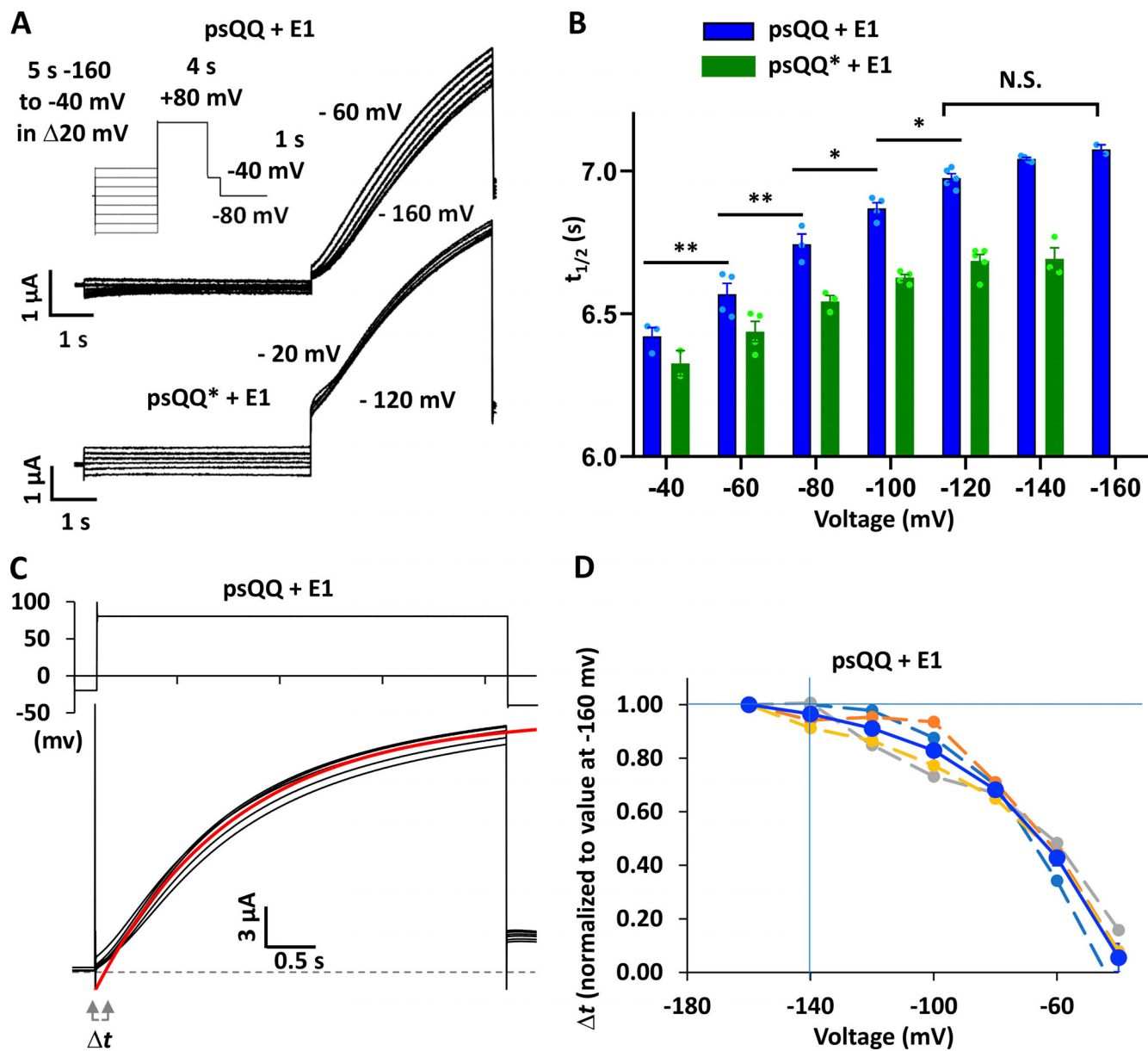


Figure S4. psQQ+E1 and psQQ*+E1 activation delay in oocytes. (A) psQQ+E1 (top) and psQQ*+E1 (bottom) expressed in oocytes. Currents from 5-s prepulses to voltages between -40 and -160 mV followed by an activating step to $+80$ mV for 4 s. Interpulse holding potential was -80 mV. Currents during the activating step are labeled according to the preceding prepulse voltage. Protocol is shown in the inset. (B) $t_{1/2}$ versus voltage where $t_{1/2}$ represents the time taken to reach half-peak activating current amplitude after the prepulse. The bars indicate mean values \pm SEM and individual values are also plotted. psQQ+E1 (blue; $n = 2-5$) and psQQ*+E1 (green; $n = 2-5$). *, ** denote $P < 0.04$ and $P < 0.008$, respectively, as determined using one-way ANOVA followed by a Bonferroni post hoc test. (C) Activation delay, Δt , as a function of prepulse potential. Protocol as in A. psQQ+E1 voltage (above) and currents (below) are shown during the 4-s pulses to $+80$ mV. Red line shows exponential fit to current activation time course after delay, Δt . Mean τ_{act} was 1.38 ± 0.021 s (SEM, range: 1.33–1.46 s). Dotted line denotes zero current. (D) Values of Δt normalized to value at -160 mV, for each data set, ($n = 4$). Individual data sets are shown as connected dashed lines and mean data as blue symbols and line. At -140 mV, Δt is $97 \pm 2\%$ of its maximum value.

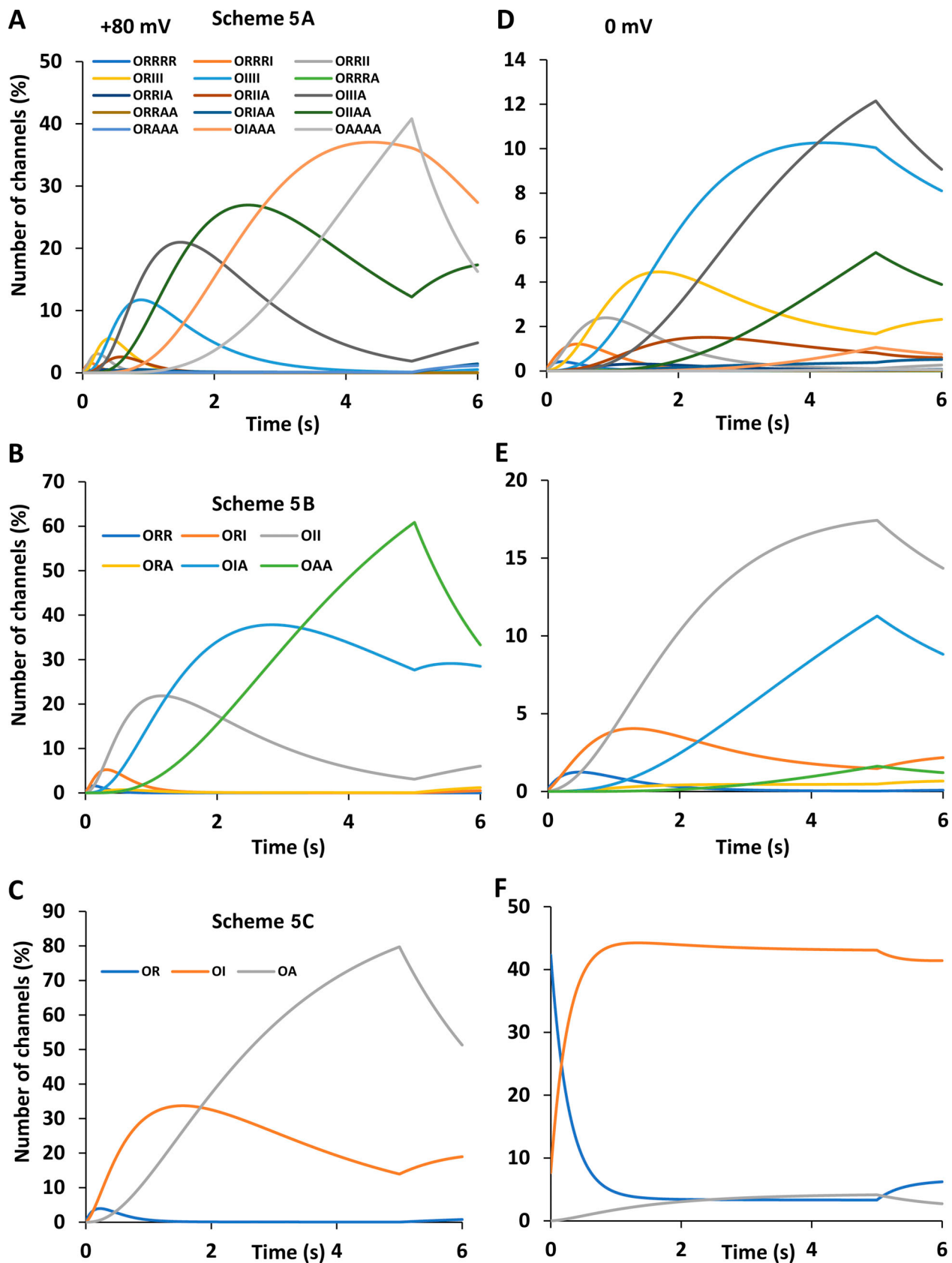


Figure S5. **Scheme 5, A-C, simulations of channel state occupancy.** (A-C) Open channel occupancies simulated using Scheme 5 A ($\text{psQ}+\text{E1}$, A), 5 B ($\text{psQQ}^*+\text{E1}$, B), and 5 C ($\text{EQ}+\text{QQ}^*\text{Q}^*+\text{E1}$, C) models using transition kinetics from Table 2, line 10, during a 5 s pulse from -140 to $+80$ mV, followed by a 1-s step to -40 mV. Number of channels is shown as a percentage of the total in the simulation, which also includes channels remaining in closed states (not shown). (D-F) As in A-C, except pulse was 0 mV. Legend colors in A-C also apply to D-F.

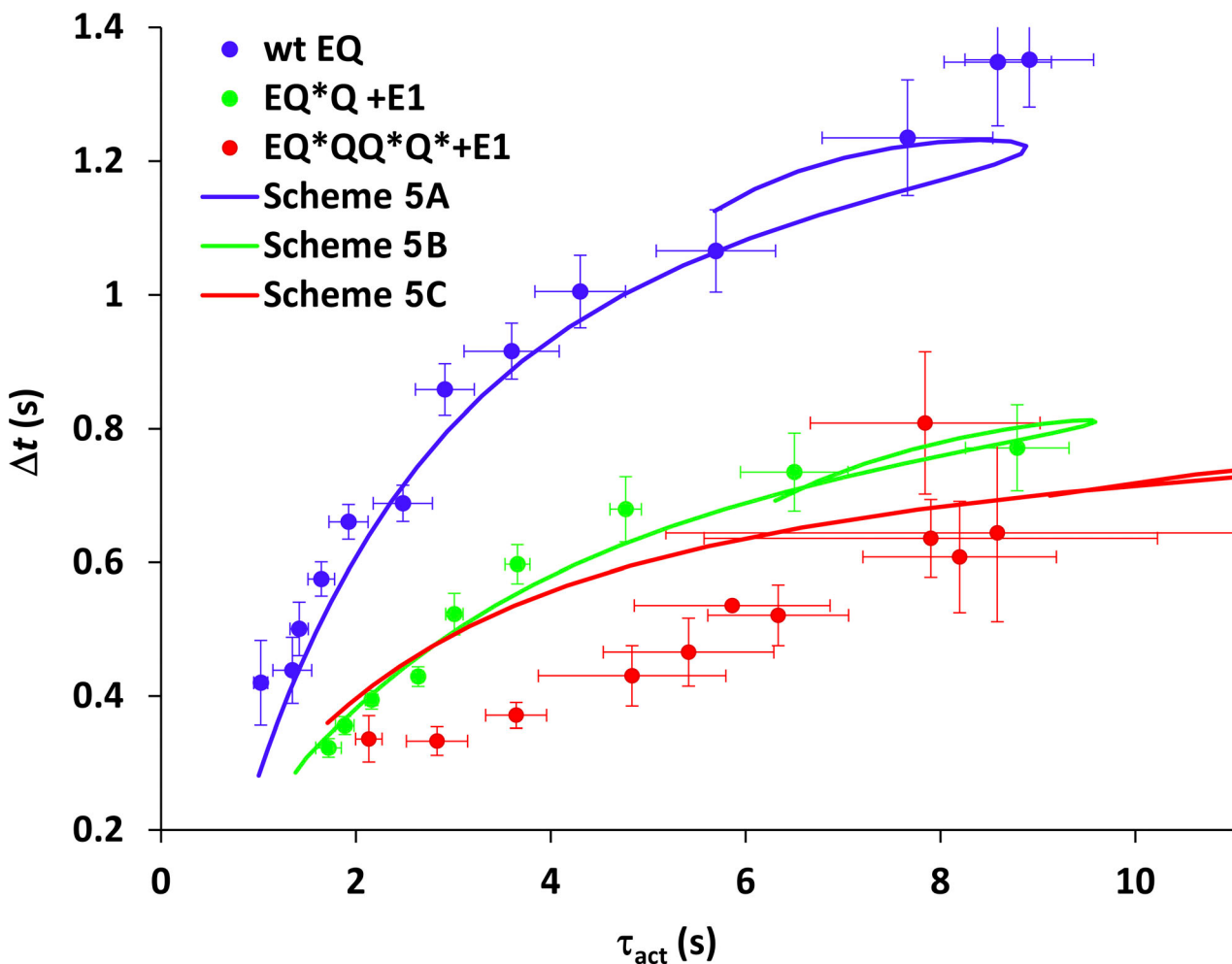


Figure S6. **Current activation delay, Δt , versus activation time constants, τ_{act} , for Scheme 5 models.** Mean tsA201 data (from Fig. 3 D) for 10-s clamp pulses from -120 mV to between -20 and $+100$ mV are shown as symbols (mean \pm SEM), for wt EQ (blue), EQ^*Q+E1 (green), and $EQ^{*QQ*Q*}+E1$ (red). Scheme 5 model data are shown as lines for wt EQ (blue), EQ^*Q+E1 (green), and $EQ^{*QQ*Q*}+E1$ (red). Fits for τ_{act} were after 0.25–1 s of the 10 s activation pulse from -55 to $+100$ mV. Unified rate constants for fits are from Table 2, row 10.

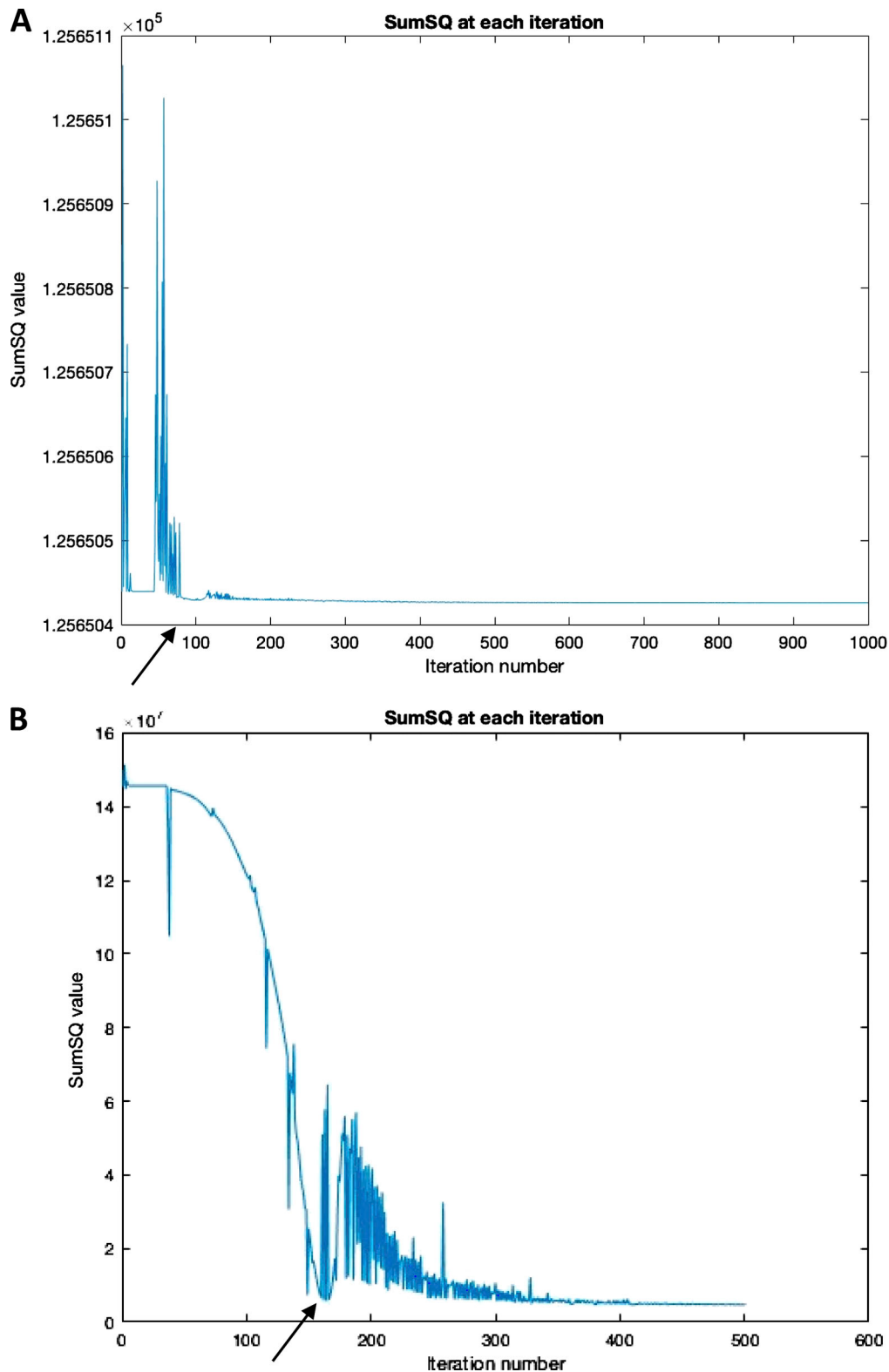


Figure S7. **Two different examples of SumSQ changing with iteration using the fminsearchbnd optimization routine.** At arrows, parameters were perturbed to avoid local minima. **(A)** Optimization was performed for G-V and F-V simultaneously. **(B)** Optimization was performed for G-V, F-V, τ_{act} , and Δt , simultaneously.